

**NOVEL GOLD MONOLAYER PROTECTED CLUSTERS: SYNTHESIS,
CHARACTERIZATION, SEPARATION, AND FUNCTIONALIZATION**

Rebecca L. Wolfe

A dissertation submitted to the faculty of the University of North Carolina at Chapel Hill in partial fulfillment of the requirements for the degree of Doctor of Philosophy in the Department of Chemistry (Analytical Chemistry).

Chapel Hill
2007

Approved by

Advisor: Dr. Royce W. Murray

Reader: Dr. R. Mark Wightman

Reader: Dr. James W. Jorgenson

Committee Member: Dr. Michel R. Gagné

Committee Member: Dr. Edward T. Samulski

© 2007
Rebecca L. Wolfe
ALL RIGHTS RESERVED

ABSTRACT

**Rebecca L. Wolfe: Novel Gold Monolayer Protected Clusters: Synthesis,
Characterization, Separation, and Functionalization
(Under the Direction of Dr. Royce W. Murray)**

Chapter One is an introduction to monolayer protected clusters (MPCs) and their unique size-dependent properties. This chapter also serves as an introduction to the methods of synthesis, characterization, functionalization, and separation of MPCs that have been explored in the literature.

Chapter Two demonstrates how the Brust synthesis of thiolate-protected gold clusters has been modified to produce identifiable proportions of a hexanethiolate-protected Au₂₂₅ core nanoparticle that display quantized double layer charging voltammetry consistent with a Au₂₂₅ core dimension. Transmission electron microscopy (TEM) and thermogravimetric results indicate an average nanoparticle formula of Au₂₂₅[(S(CH₂)₅CH₃)]₇₅. A simulated pulse voltammogram that accounts for the TEM nanoparticle dispersity matches reasonably well with that of the polydisperse synthetic sample containing the Au₂₂₅ component. In confirmation of the size determination, an HPLC analysis using ratiometric absorbance and electrochemical detectors gives a core radius of 1.0 nm for the Au₂₂₅ nanoparticle.

Chapter Three describes the synthesis and compositional analysis of four different gold clusters with protecting monolayers comprised solely of ferrocene hexanethiolate ligands.

The gold nanoparticles have average core diameters of 1.4, 1.6, 2.0, and 2.2 nm with estimated average atom counts of 55, 140, 225, and 314 Au atoms and average monolayer coverages of 37, 39, 43, and 58 ferrocenated ligands, respectively. The data show unequivocally that the number of ferrocene hexanethiolate ligands bound to each core size is constrained by the steric requirements of the ferrocene head group; the ligand numbers are significantly smaller than those for hexanethiolate ligands bonded to analogous sized Au cores. Voltammetry of dilute solutions of these nanoparticles shows a large ferrocene oxidation wave and, at more negative potentials, smaller one-electron waves for the quantized double-layer charging of the Au cores. Together, the ferrocenes and core of the ferrocenated Au₃₁₄ nanoparticle deliver 60 electrons at the ferrocene oxidation potential, which amounts to a very large volume charge capacity, $7 \times 10^9 \text{ C/m}^3$, for an undiluted nanoparticle sample.

Chapter Four describes how Au nanoparticles fully coated with **w**-ferrocenyl hexanethiolate ligands, with average composition Au₂₂₅(**w**-ferrocenyl hexanethiolate)₄₃, exhibit a unique combination of adsorption properties on Pt electrodes. The adsorbed layer is so robust that electrodes bearing sub-monolayer, monolayer, and multilayer quantities of these nanoparticles can be transferred to fresh electrolyte solutions and then exhibit stable ferrocene voltammetry over long periods of time. The adsorption kinetics is quite slow and monolayer and sub-monolayer deposition can be described by a rate law that is first order in bulk concentration of the nanoparticles and in available surface of the platinum electrode. The adsorption mechanism is proposed to involve ion-pair bridges between oxidized (ferrocenium) sites and certain specifically adsorbed electrolyte anions on the electrode. Adsorption is promoted by potential scanning through the ferrocene redox wave

and by high concentrations of $\text{Bu}_4\text{N}^+\text{X}^-$ electrolyte ($\text{X}^- = \text{ClO}_4^-, \text{PF}_6^-$) in the CH_2Cl_2 solvent; there is no adsorption if $\text{X}^- = \text{p-toluenesulfonate}$ or if the electrode is coated with an alkanethiolate monolayer. The electrode double layer capacity is unchanged in the presence of the ferrocenated layers, and the adsorbed nanoparticles can be gradually desorbed by scanning to potentials more negative than the electrode's potential of zero charge. The full-width-half-maxima of the symmetrical voltammetric peaks of an adsorbed monolayer of ferrocenated nanoparticles are considerably narrower (typical 35 mV) than expected (90.6 mV, at 298 K) for a one electron transfer or for reactions of multiple, independent redox centers with identical formal potentials. The peak narrowing is explicable by a surface activity effect involving large, attractive lateral interactions between nanoparticles and by a proposed series of reactions of ferrocene sites whose formal potential values become successively altered as ion-pair bridges are formed.

Chapter Five presents the use of anion-induced adsorbed $\text{Au}_{225}(\text{w-ferrocenyl hexanethiolate})_{43}$ on carbon-paper-supported carbon aerogel (nanofoam) electrodes as novel materials for supercapacitors. The specific capacitance (in F/g) of the carbon nanofoam electrode increases by more than 8000% upon adsorption of the ferrocenyl functionalized gold MPCs. This remarkable increase in capacitance can be attributed to the pseudocapacitance derived from the redox charging of the monolayer as well as the double-layer capacitance arising from the charging of the gold core. The carbon nanofoam electrode is also ground into a fine powder to increase the surface area, and similar studies with adsorbed ferrocenated MPCs are performed. While the capacitance of the powder does increase upon adsorption of the MPC, it does not surpass that of the intact MPC-modified nanofoam electrode. Scanning electron microscopy shows that the powder is

quite polydisperse in size and shape, and the dropcast method to analyze the powder electrochemically leads to nonuniform distribution of the powder onto surfaces.

Chapter Six investigates the catalytic properties of Pd, Au, Ag, and bimetallic AgAu MPCs. A polar protecting monolayer shell consisting of *N*-(2-mercaptopropionyl)glycine ligands (also known as tiopronin) is used to allow for solubility in water. The reaction that is catalyzed by all four MPCs is the reduction of 4-nitrophenol in the presence of sodium borohydride, which on its own does not reduce the substrate. The four MPCs all successfully catalyze reduction, and first-order rate constants are derived and found to be comparable with other literature values. Pd MPCs are not surprisingly significantly faster than the other three MPCs, but, more interestingly, the bimetal AgAu MPC catalyzes the reduction faster than that of the monometallic Ag and Au MPCs.

ACKNOWLEDGEMENTS

I would like to thank my advisor, Dr. Royce W. Murray, for his outstanding guidance and support. He has been an invaluable mentor to me over the past four years. His scientific knowledge is incomparable, and his many ideas have helped stimulate my own scientific thinking. I also very much appreciate the present and former members of the Murray group who have played the roles of mentors, collaborators, and good friends. It was a pleasure working with the many talented and intellectual group members who passed through the lab during my time at UNC. I would also like to thank Dr. Stephen Feldberg of Brookhaven National Lab for all of his stimulating discussions and intriguing ideas as well as the UNC chemistry department's brilliant faculty and amazing staff for all of their help and encouragement over the past four years.

I would also like to thank my family and my fiancé, Dr. Paul Stiles, for their unwavering support and encouragement. Paul's hard work and dedication to his own doctoral research set an excellent example for me to follow, and his passion for science is clearly contagious. Without the life-long encouragement and support from my parents, I never would have made it this far. My two sisters have also been instrumental in supporting me in my pursuit of a Ph.D. I have additionally been blessed with wonderful grandparents, aunts, uncles, and cousins. Finally, I would like to thank all the good friends I have made while here in NC. They have gone above and beyond to help make life in graduate school a wonderful experience.

TABLE OF CONTENTS

	Page
List of Tables	xi
List of Figures	xii
List of Abbreviations and Symbols.....	xvii
 Chapter 1. Introduction to Monolayer Protected Metal Clusters	 1
1.1. Introduction.....	1
1.2. MPC Synthesis.....	2
1.3. MPC Size Dispersion and Separation.....	3
1.4. Core Size Dependent Properties of Gold MPCs	4
1.5. Determination of Number of Gold Core Atoms	6
1.6. References.....	13
 Chapter 2. Analytical Evidence for the Monolayer Protected Cluster Au₂₂₅[(S(CH₂)₅CH₃)₇₅].....	 20
2.1. Introduction.....	20
2.2. Experimental Section.....	22
2.3. Results and Discussion	25
2.4. Conclusions.....	39
2.5. Acknowledgements.....	43
2.6. References.....	44

Chapter 3. Fully Ferrocenated Hexanethiolate Monolayer-Protected Gold Clusters.....	47
3.1. Introduction.....	47
3.2. Experimental Section.....	51
3.3. Results and Discussion	54
3.4. Conclusions.....	78
3.5. Acknowledgements.....	82
3.6. References.....	83
Chapter 4. Anion Induced Adsorption of Ferrocenated Nanoparticles.....	87
4.1. Introduction.....	87
4.2. Experimental Section	89
4.3. Results and Discussion	93
4.4. Acknowledgements.....	133
4.5. References.....	135
Chapter 5. Redox Functionalized Monolayer Protected Gold Clusters as Electrochemical Capacitors.....	139
5.1. Introduction.....	139
5.2. Experimental Section	141
5.3. Results and Discussion	145
5.4. Conclusions.....	174
5.5. Acknowledgements.....	175
5.6. References.....	176
5.7 Appendix.....	179

Chapter 6.	Catalysis with Monolayer Protected Metal Clusters.....	183
6.1.	Introduction.....	183
6.2.	Experimental Section	185
6.3.	Results and Discussion	187
6.4	Conclusions.....	197
6.5	Acknowledgements.....	197
6.6.	References.....	199

LIST OF TABLES

Table 2.1	Estimation of Core Size of $\text{Au}_{225}[(\text{S}(\text{CH}_2)_5\text{CH}_3)]_{75}$ MPCs Using HPLC and Ratio of Optical Absorbance Detector Signal and One-Electron Charging Currents of MPCs in Two Separate Experiments.....	42
Table 3.1	Voltammetric Quantized Double Layer Charging Results for Ferrocene-hexanethiolate Protected Au Clusters (Figure 3.1) and Literature Values for Hexanethiolate Protected Au Clusters.....	59
Table 3.2	Ligand Counts and Ligand/Surface Atom Coverages for Hexanethiolate and Fully Ferrocenated Hexanethiolate Monolayers, for Au MPCs of Varying Core Size.....	76
Table 4.1	Effect of type and concentration of supporting electrolyte on coverage Γ_{MPC} of ferrocenated MPCs adsorbed on Pt electrode from a 0.05 mM MPC solution, during survey potential scanning (between 0.2 and 1.0 V at 0.50 V/s).....	100
Table 4.2	Effect of potential scanning (between 0.2 and 1.0 V at 0.50 V/s) on adsorption of ferrocenated MPCs from $\text{Bu}_4\text{NClO}_4/\text{CH}_2\text{Cl}_2$ solution in survey experiment.....	101
Table 4.3	Rate constants for MPC adsorption derived from fixed-time and no-scan experimental protocols. G_{MPC} was measured as a function of MPC concentration in fixed-time experiments and as a function of time in no-scan protocol. (All scans were taken between 0 and 0.8 V/s.).....	119
Table 5.1	Specific capacitances of bare and MPC-modified carbon nanofoam electrodes and powder.....	155
Table 5.1A	<i>RC</i> time constant and capacitance values for different carbon nanofoam electrode materials.....	182
Table 6.1	Apparent rate constants for the reduction of 4-nitrophenol in the presence of NaBH_4 and tiopronin-protected metal clusters.....	198

LIST OF FIGURES

Figure 1.1	Cyclic voltammogram of 0.2 mM Au ₁₄₀ (SC6) ₅₃ in CH ₂ Cl ₂ with 0.1 M Bu ₄ NClO ₄ at 283 K with scan rate of 0.1 V/s.....	7
Figure 1.2	Concentric sphere capacitor model for a monolayer protected gold cluster.....	9
Figure 2.1	(a) TEM image of Au ₂₂₅ [(S(CH ₂) ₅ CH ₃)] ₇₅ in CH ₂ Cl ₂ ; (b) Size-distribution histogram for several TEM images of Au ₂₂₅ [(S(CH ₂) ₅ CH ₃)] ₇₅ in CH ₂ Cl ₂ (118 MPCs in total from three different batches synthesized separately); (c) TGA analysis of organic mass lost for a sample of Au ₂₂₅ [(S(CH ₂) ₅ CH ₃)] ₇₅ ; (d) UV/Vis absorbance spectrum for Au ₂₂₅ [(S(CH ₂) ₅ CH ₃)] ₇₅	27
Figure 2.2	(a) Model of Au ₂₂₅ core with vertex, terrace, and edge atoms labeled; (b) Osteryoung square wave voltammogram (OSWV) of 0.2 mM Au ₂₂₅ [(S(CH ₂) ₅ CH ₃)] ₇₅ in CH ₂ Cl ₂ with 0.1 M tetrabutylammonium perchlorate. OSWV measured with step potential of 4 mV, square wave amplitude of 25 mV, square wave frequency of 15 s ⁻¹ , quiet time of 2 s, sensitivity of 1 μA/V, and sampling rate of 256 samples per point; (c) Oxidation scan only of OSWV of polydisperse Au ₂₂₅ [(S(CH ₂) ₅ CH ₃)] ₇₅ ; the solid line represents the same experimental data as in part (b) of this figure. The shaded line represents a simulation which includes currents weighted according to proportions of various sizes from TEM histogram (Figure 2.1b), as shown in Ref. 32.....	30
Figure 2.3	HPLC chromatograms for a solution of a mixture of Au ₂₂₅ [(S(CH ₂) ₅ CH ₃)] ₇₅ and Au ₁₄₀ [(S(CH ₂) ₅ CH ₃)] ₅₇ (solid line), Au ₂₂₅ [(S(CH ₂) ₅ CH ₃)] ₇₅ alone (dotted line), and Au ₁₄₀ [(S(CH ₂) ₅ CH ₃)] ₅₇ alone (dashed line) from (a) the PDA absorbance detector and (b) the electrochemical detector taken at a potential of 350 mV. The corresponding absorbance spectra are shown for the (c) Au ₂₂₅ [(S(CH ₂) ₅ CH ₃)] ₇₅ and (d) Au ₁₄₀ [(S(CH ₂) ₅ CH ₃)] ₅₇ peaks obtained from the absorbance chromatogram of the mixture.....	37
Figure 2.4	Current vs. potential curves for the single electron charging event of the 0 to +1 state of the eluted bands of (a) Au ₂₂₅ [(S(CH ₂) ₅ CH ₃)] ₇₅ and (b) Au ₁₄₀ [(S(CH ₂) ₅ CH ₃)] ₅₇ with limiting current shown (i _{lim}).....	40
Figure 3.1	(A) Cyclic voltammogram of 0.2 mM Au ₇₅ (SC6Fc) ₃₇ in 0.1 M Bu ₄ NClO ₄ /CH ₂ Cl ₂ under Ar atmosphere, at 284 K, potential scan rate 500 mV/s, sample interval of 1 mV; (B) Osteryoung square wave voltammogram (OSWV) of Au ₃₁₄ (SC6Fc) ₅₈ ; (C) OSWV of Au ₂₂₅ (SC6Fc) ₄₃ ; (D) OSWV of Au ₁₄₀ (SC6Fc) ₃₉ ; (E) OSWV of Au ₇₅ (SC6Fc) ₃₇ (asterisks indicate first one-electron oxidation and reduction peaks). For all four MPC core sizes,	

	OSWV was performed on 0.2 mM MPC in 0.1 M Bu ₄ NClO ₄ /CH ₂ Cl ₂ with step potential of 4 mV, square wave amplitude of 25 mV, and square wave frequency of 15 s ⁻¹	56
Figure 3.2	UV/Vis absorbance spectra for the four separately synthesized ferrocene hexanethiolate protected Au clusters in CH ₂ Cl ₂	61
Figure 3.3	TEM images of (a) Au ₃₁₄ (SC6Fc) ₅₈ , (b) Au ₂₂₅ (SC6Fc) ₄₃ , (c) Au ₁₄₀ (SC6Fc) ₃₉ , and (d) Au ₇₅ (SC6Fc) ₃₇ . Corresponding core diameter histograms with average core diameters labeled, each from 100 sampled MPC cores, are inset in the bottom right corner of each image. Inset in the top left corner of (b) is a high-resolution image of a Au ₂₂₅ (SC6Fc) ₄₃ core clearly showing lattice planes.....	63
Figure 3.4	TEM images of (a) Au ₃₁₄ (SC6) ₉₁ , (b) Au ₂₂₅ (SC6) ₇₅ , (c) Au ₁₄₀ (SC6) ₅₃ , and (d) Au ₇₅ (SC6) ₄₀ . Corresponding core diameter histograms with average core diameters labeled, each from 100 sampled MPC cores, are inset in the bottom right corner of each image.....	66
Figure 3.5	First derivative of the CV of (A) Au ₃₁₄ (SC6Fc) ₆₈ , (B) Au ₂₂₅ (SC6Fc) ₄₃ , and (C) Au ₁₄₀ (SC6Fc) ₃₉ done under Ar atmosphere at 284 K with potential scan rate of 100 mV/s and sample interval of 1 mV. First derivative of the CV of (D) 0.1 mM Bu ₄ NClO ₄ in CH ₂ Cl ₂ (<i>no MPC</i>) under identical conditions (blue, upper line, corresponding to left y-axis) and under identical conditions except with a sample interval of 4 mV (red, lower line, corresponding to right y-axis). The difference in sample interval is shown to demonstrate the dependence of peak spacing with sample interval and to show that 100 mV spacing can be achieved as in other references which attribute this spacing as QDL peaks. ^{46,47}	68
Figure 3.6	Thermogravimetric analysis (TGA) traces of (A) HSC6Fc, (B) Au ₂₂₅ (SC6Fc) ₄₃ , and (C) Au ₂₂₅ (SC6) ₇₅ , for comparison.....	71
Figure 3.7	Bulk electrolysis charge vs. time curves for Au ₇₅ (SC6Fc), Au ₁₄₀ (SC6Fc) ₃₉ , Au ₂₂₅ (SC6Fc) ₄₃ , and Au ₃₁₄ (SC6Fc) ₅₈ at concentrations of 0.05 mM, 0.11 mM, 0.10 mM, and 0.04 mM, respectively, and over potential differences of 462 mV, 447 mV, 260 mV, and 230 mV, respectively. All measurements were performed in 50 mM Bu ₄ NClO ₄ in CH ₂ Cl ₂ using a Pt mesh working electrode, a Pt wire counter electrode (in a separate cell compartment), and a Ag/AgCl (aqueous) reference electrode.....	73
Figure 3.8	(A) Cyclic voltammogram of solution of 0.1 mM Au ₂₂₅ (SC6Fc) ₄₃ in 1 M Bu ₄ NPF ₆ /CH ₂ Cl ₂ under Ar atmosphere, at 284 K, potential scan rate 25 mV/s. (B) After solution electrochemistry is performed, electrode is rinsed with 1 M Bu ₄ NPF ₆ /CH ₂ Cl ₂ and used to take cyclic voltammogram of <i>MPC-free</i> solution of 1 M Bu ₄ NPF ₆ /CH ₂ Cl ₂ under Ar atmosphere, at 284 K, potential scan rate 25 mV/s.....	79

Figure 4.1	Cyclic voltammetry of: Curves A-C, 0.1 mM $\text{Au}_{225}(\text{SC6Fc})_{43}$ (MPC) in 1.0 M $\text{Bu}_4\text{NPF}_6/\text{CH}_2\text{Cl}_2$ solution at potential scan rates 0.025, 0.20, and 2.0 V/s, respectively, and of Curves D-F, an adsorbed $\text{Au}_{225}(\text{SC6Fc})_{43}$ film on electrode ($\Gamma_{\text{MPC}} = 7.1 \times 10^{-12} \text{ mol/cm}^2$) formed by potential scanning in 0.1 mM MPC in 1.0 M $\text{Bu}_4\text{NPF}_6/\text{CH}_2\text{Cl}_2$ solution and transferred to an <i>MPC-free</i> 1.0 M $\text{Bu}_4\text{NPF}_6/\text{CH}_2\text{Cl}_2$ solution, at potential scan rates of 0.025, 0.20, and 2.0 V/s, respectively.....	94
Figure 4.2	First 10 cyclic voltammograms (1.0 V/s) of an adsorbed MPC layer formed in a 0.1 mM MPC, 1.0 M $\text{Bu}_4\text{NPF}_6/\text{CH}_2\text{Cl}_2$ solution after transfer to an <i>MPC-free</i> 1.0 M $\text{Bu}_4\text{NPF}_6/\text{CH}_2\text{Cl}_2$ solution. Inset: blow-up of oxidation current peak, showing slight initial change. Thereafter, peak currents are stable and reproducible.....	97
Figure 4.3	Oxidation peak (solid blue line) from cyclic voltammetry (2.0 V/s) of partly ferrocenated, $\text{Au}_{225}(\text{SC6})_{58}(\text{SC6Fc})_{17}$, adsorbed MPCs in 1.0 M Bu_4NClO_4 . The dashed pink line is a simulated waveshape for a reversible one-electron transfer with no lateral interactions and with E^0 the same for all ferrocenes (Equation 4). $\Gamma_{\text{MPC}} = 2 \times 10^{-13} \text{ mol/cm}^2$	103
Figure 4.4	(A) Cyclic voltammetry (blue curve, 0.20 V/s) of an adsorbed $\text{Au}_{225}(\text{SC6Fc})_{43}$ film formed on a clean Pt electrode from a 0.1 mM MPC, 1.0 M $\text{Bu}_4\text{NPF}_6/\text{CH}_2\text{Cl}_2$ solution and transferred to an <i>MPC-free</i> 1.0 M $\text{Bu}_4\text{NPF}_6/\text{CH}_2\text{Cl}_2$ solution. (B) Cyclic voltammetry (red curve, 0.20 V/s) of an identically treated Pt electrode, except that the Pt electrode had been first coated with a dodecanethiolate self-assembled monolayer (SAM).....	106
Figure 4.5	Cyclic voltammograms of an MPC-free 1.0 M $\text{Bu}_4\text{NClO}_4/\text{CH}_2\text{Cl}_2$ solution at (A) a bare Pt electrode and (B) a Pt electrode with an adsorbed film of $\text{Au}_{225}(\text{SC6Fc})_{43}$ (made in 0.1 mM MPC solution). The cyclic voltammograms were collected at 0.20 V/s.....	108
Figure 4.6	Potential cycling on 1 M $\text{Bu}_4\text{NClO}_4/\text{CH}_2\text{Cl}_2$ of a Pt electrode with an adsorbed film of $\text{Au}_{225}(\text{SC6Fc})_{43}$ (made in 0.1 mM MPC/1.0 M $\text{Bu}_4\text{NClO}_4/\text{CH}_2\text{Cl}_2$ solution). A 90 % loss in coverage was observed over the course of 280 scans that included the negative potential region. The cycling was performed at 0.2 V/s with a Pt wire auxiliary electrode and a Ag/AgCl (aq) reference electrode.....	110
Figure 4.7	Cartoon of ion-induced adsorption, where ferrocenium cations on the MPC form ion-pair bridges with electrolyte anions specifically adsorbed to the Pt electrode. It can be imagined that the ligand shell may become deformed to form ion-pair bridges of similar dimensions. Formation of ion-pair bridges shown stabilizes successive ion-pair bridges and can cause a successive shift in Fc/Fc^+ formal potentials ($E_{j_{\text{max}}}$ scheme, see later). It is also possible to imagine lateral ion-pair bridges, between adsorbates.....	113

Figure 4.8 Panel A: Fractional coverages (θ) of MPCs measured in *fixed-time* experiments at different MPC concentrations (lower horizontal axis) in 1.0 M Bu₄NClO₄ (open black circles, $\Gamma_{\text{MONO}} = 0.7 \times 10^{-11}$ mol/cm²) and 1.0 M Bu₄NPF₆ (filled black circles, $\Gamma_{\text{MONO}} = 1.3 \times 10^{-11}$ mol/cm²) electrolytes. The upper horizontal axis is normalized MPC concentration*time (tc), where $t = 80$ s for all data points. Panel B: Coverage of MPCs (Γ_{MPC}) measured as a function of $\log(tc)$ in *no-scan* (open red circles), *scanning* (filled red circles), and *fixed-time* (ClO₄⁻ open black circles, PF₆⁻ filled black circles) protocol experiments. *No-scan and scanning* experimental protocols used a fixed (0.05 mM) MPC concentration in 1.0 M Bu₄NClO₄/CH₂Cl₂. The solid lines in both Panels are fits to the first-order rate expression, Equation 3, for the rate constants displayed in Table 4.3. No fit was performed on the *scanning* protocol as it leads to multilayers and does not appear to attain a saturation coverage.....116

Figure 4.9 Simulations of $E_{j_{\text{max}}}$ scheme voltammetry for sequential electron transfer reactions of 10 ferrocene ligands per adsorbed MPC, where each successively reacting ferrocene's formal potential is incrementally shifted by $\Delta E^{\circ'} = -4$ mV. The numbers by the curves are values of j ; i.e., $j = 3$ is the voltammetry predicted for reaction of the first three ferrocenes only and $j = 10$ for overall current after the tenth ferrocene has reacted.....123

Figure 4.10 Simulations of a 10 e⁻ transfer with 10 successive $E^{\circ'}$ values, each less positive (by $\Delta E^{\circ'}$) than the previous one ($E_{j_{\text{max}}}$ scheme); each simulation has a different $\Delta E^{\circ'}$, with the numbers by the curve representing the values of $\Delta E^{\circ'}$ ranging from -1 mV (the sharpest peak) to -11 mV (the broadest peak).....126

Figure 4.11 Simulations of the oxidative peak of a one electron transfer of an ideal adsorbed ferrocene monolayer (blue dashed line) and $E_{j_{\text{max}}}$ scheme with $j = 10$ and varied $\Delta E^{\circ'}$ (pink dashed line), compared to experimental voltammetry (green solid line, 0.025 V/s) of ferrocenated MPCs adsorbed from a 0.1 mM MPC solution in 1.0 M Bu₄NPF₆/CH₂Cl₂ (Curves A – C) and 1.0 M Bu₄NClO₄/CH₂Cl₂ (Curve D). Varied $\Delta E^{\circ'}$ fits (blue dashed line) for Curve A has $\Delta E^{\circ'} = -1$ mV (FWHM = 23 mV), for Curve B and D $\Delta E^{\circ'} = -4$ mV (FWHM = 35 mV), and for Curve C $\Delta E^{\circ'} = -6$ mV (FWHM = 53 mV); the best fit for both electrolytes is at $\Delta E^{\circ'} = -4$ mV. To compare the curves, all are normalized to the experimental $E^{\circ'}$ and peak current.....128

Figure 4.12 Ferrocene oxidation peak in experimental voltammetry (green solid line, 0.10 V/s) of ferrocenated MPCs adsorbed from a 0.1 mM MPC solution in 1.0 M Bu₄NClO₄/CH₂Cl₂ compared to waveshapes (pink dashed lines) predicted from Equations 4 (Curve A) and 5 (Curve B for $r_{\text{Ox}} = r_{\text{Red}} = 2 \times 10^{11}$ mol⁻¹

	¹ cm ²). Experimental data collected from 1.0 M Bu ₄ PF ₆ /CH ₂ Cl ₂ (not shown) gave a similarly good fit to Equation 5, using $r_{\text{Ox}} = r_{\text{Red}} = 6 \times 10^{11} \text{ mol}^{-1}\text{cm}^2$. Predicted curves are normalized to the experimental E ^o and peak current.....	132
Figure 5.1	(A) Cyclic voltammogram (0.025 V/s) of an adsorbed Au ₂₂₅ (SC6Fc) ₄₃ film formed on a clean glassy carbon electrode from a 0.1 mM MPC, 1.0 M Bu ₄ NClO ₄ /CH ₂ Cl ₂ solution and transferred to an MPC-free 1.0 M Bu ₄ NClO ₄ /CH ₂ Cl ₂ solution. (B) Comparison of cyclic voltammograms of two electrodes treated identically to (A) except that the blue curve is for a Au ₂₂₅ (SC6Fc) ₄₃ film formed on a clean glassy carbon electrode (same as (A)) and the maroon curve is for a Au ₂₂₅ (SC6Fc) ₄₃ film formed on a clean platinum electrode.....	148
Figure 5.2	Cartoon schematic of the carbon nanofoam electrode used. A plastic-protected wire with exposed metal ends is connected to a square cut-out from a carbon-paper-supported carbon nanofoam sheet through one metal end with silver paint (cured overnight) and sealed with epoxy (cured overnight).....	151
Figure 5.3	Pseudo-first-order rate plots for exchange of phenylethanethiolate (PhC2S-) by <i>p</i> -toluenethiol (4-CH ₃ -PhSH) onto (Panel a) Au ₃₈ (SC2Ph) ₂₄ and (Panel b) Au ₁₄₀ (SC2Ph) ₅₃ at mole ratio of 4-CH ₃ -PhSH/ PhC2S- = 4.3 :1 and 3.3 :1, respectively.....	153
Figure 5.4	Fifty cyclic voltammograms of Au ₂₂₅ (SC6Fc) ₄₃ -modified carbon nanofoam electrode in 1.0 M NaSO ₄ /H ₂ O taken at scan rate 0.025 V/s. After fifty cycles, there is <i>ca.</i> 34% loss in current. Counter electrode was vitreous carbon.....	158
Figure 5.5	Cyclic voltammograms of (A) bare and (B) Au ₂₂₅ (SC6Fc) ₄₃ -modified carbon nanofoam electrodes in 1.0 M NaSO ₄ /H ₂ O at 0.010 V/s with vitreous carbon counter electrode. The larger blue curves are for a carbon nanofoam electrode with area 9.5 cm ² , and the smaller marron curves are for a carbon nanofoam electrode with area 2.3 cm ² . (C) Cyclic voltammograms of the same Au ₂₂₅ (SC6Fc) ₄₃ -modified carbon nanofoam electrode (A = 9.5 cm ²) in 1.0 M NaSO ₄ /H ₂ O at 0.002 V/s with (maroon curve) and without (blue curve) the drying at 70 °C for one hour step between cycling in 0.1 mM MPC/1.0 M Bu ₄ NClO ₄ /CH ₂ Cl ₂ (for MPC adsorption) and cycling in 1.0 M NaSO ₄ /H ₂ O (for capacitance measurements). The counter electrode used for both was vitreous carbon.....	160
Figure 5.6	Scanning electron micrographs of (a and c) bare carbon-paper-supported carbon nanofoam electrode and (b and d) manually ground bare carbon nanofoam powder.....	163

Figure 5.7	Cyclic voltammogram of bare carbon nanofoam powder dropcast on a glassy carbon disk electrode (maroon line) and $\text{Au}_{225}(\text{SC6Fc})_{43}$ -modified carbon nanofoam powder dropcast on the same glassy carbon disk electrode (blue line) in 1.0 M $\text{NaSO}_4/\text{H}_2\text{O}$. Scan rate was 0.002 V/s and counter electrode was platinum wire.....	166
Figure 5.8	Mass normalized cyclic voltammograms of $\text{Au}_{225}(\text{SC6Fc})_{43}$ -modified carbon nanofoam electrode (red line) and $\text{Au}_{225}(\text{SC6Fc})_{43}$ -modified carbon nanofoam powder dropcast on a glassy carbon disk electrode (black line) in 1.0 M $\text{NaSO}_4/\text{H}_2\text{O}$. Scan rate was 0.005 V/s. Counter electrode was vitreous carbon for the MPC-modified nanofoam electrode and platinum wire for the MPC-modified nanofoam powder film.....	168
Figure 5.9	Rotated disk voltammetry of bare carbon nanofoam powder sonicated in 1.0 M $\text{NaSO}_4/\text{H}_2\text{O}$ at 0.010 V/s and rotation rates of (A) 400 (teal curve), 625 (purple curve), 900 (black curve), 1600 (blue curve), and 2500 (maroon curve) rpm and (B) 1600 (maroon curve), 2500 (blue curve), and 3600 (teal curve) rpm. Counter electrode for all scans was a platinum wire.....	172
Figure 5.1A	Plots of natural log of current ($\ln(I)$) vs. time (t) for the small (physical area = 2.3 cm^2) bare carbon nanofoam electrode (A), large (physical area = 9.5 cm^2) bare (B) and $\text{Au}_{225}(\text{SC6Fc})_{43}$ -modified (C) carbon nanofoam electrodes, and $\text{Au}_{225}(\text{SC6Fc})_{43}$ -modified carbon nanofoam powder (D). The insets in each plot are of the first five points of the larger plot in which the RC values were derived from the slopes using Equation 1A.....	181
Figure 6.1	UV/visible absorbance spectra of tiopronin-protected clusters with metal cores of (a) Pd, (b) Au, (c) Ag, and (d) AgAu.....	188
Figure 6.2	UV-Vis absorbance spectra of 0.1 mM 4-nitrophenol in H_2O (pH = 12) with $1 \times 10^{-2} \text{ M NaBH}_4$ and $2.0 \times 10^{-4} \text{ M}$ tiopronin-protected AgAu clusters over a time period of one to 125 minutes with spectra taken every one minute.....	190
Figure 6.3	Absorbance at 400 nm vs. time plot of the reduction of 4-nitrophenol using the tiopronin-protected clusters with metal cores comprised of (a) Pd, (b) AgAu, (c) Ag, and (d) Au. Absorbance was monitored in H_2O (pH = 12) with $1.0 \times 10^{-2} \text{ M NaBH}_4$, and $2.0 \times 10^{-4} \text{ M MPC}$	193
Figure 6.4	Plot of $\ln(Abs)$ vs. time, where Abs is absorbance monitored at 400 nm, of the reduction of 4-nitrophenol using as catalysts the tiopronin-protected clusters with metal cores comprised of (a) Pd, (b) AgAu, (c) Ag, and (d) Au. Absorbance was monitored in H_2O (pH = 12) with $1.0 \times 10^{-2} \text{ M NaBH}_4$, and $2.0 \times 10^{-4} \text{ M MPC}$. The straight black lines through the curves were used to determine the apparent rate constant.....	195

LIST OF ABBREVIATIONS AND SYMBOLS

2-D	Two-Dimensional
3-D	Three-Dimensional
A	Absorbance
	Amperes
	Electrode area
abbr.	abbreviation
A_{CLU}	MPC surface area
Ag	Silver
AgQRE	Silver quasi-reference electrode
Ag/Ag⁺	Silver-silver ion non-aqueous reference electrode
Ag/AgCl (aq)	Silver-silver chloride aqueous reference electrode
Au	Gold
AuCl₄⁻	Tetrachloroaurate
Au(I)-SR	Au(I) thiolate
a	Atto-
aF	AttoFarad
BAS	Bioanalytical Systems
BH₄⁻	Borohydride
Bu₄NClO₄	Tetrabutylammonium perchlorate
Bu₄NPF₆	Tetrabutylammonium hexafluorophosphate
C	Carbon
	Concentration
	Coulombs
¹³C NMR	¹³ C Nuclear Magnetic Resonance Spectroscopy
°C	Degrees Celsius
CCl₄	Carbon tetrachloride
C_{MPC}	MPC double-layer capacitance
CD₂Cl₂	Deuterated methylene chloride
C_{COMPACT}	Compact layer double-layer capacitance
C_{DIFFUSE}	Diffuse layer double-layer capacitance

CE	Capillary electrophoresis
CH₂	Methylene group
CH₂Cl₂	Methylene chloride (or dichloromethane)
CH₃	Methyl group
CH₃CN	Acetonitrile
C_n	Alkanethiol with n carbon atoms
COOH	Carboxylic acid group
CV	Cyclic voltammetry
ca.	About
cm	Centimeter
D	Diffusion coefficient
D_{MPC}	MPC diffusion coefficient
DCM	Methylene chloride
DL	Double-layer
DPV	Differential Pulse Voltammetry
D_R	Diffusion coefficient of reduced species
d	Diameter
	Length of MPC monolayer
E	Potential
DE	Potential difference
	Potential step
	Pulse amplitude
E°	Formal potential
E°_{Z,Z-1}	Formal potential of the Z/(Z-1) charge state couple
E_{1/2}	Electrochemical half-wave potential
ECLC	Liquid chromatography with electrochemical detector
E_{PZC}	Potential-of-zero charge
EQCM	Electrochemical Quartz Crystal Microbalance
e	Electronic charge
e⁻	Electron
equiv	Equivalent

eV	Electron volts
exp	Exponential
F	Farad
	Faraday constant
mF	MicroFarad
Fc	ferrocene
FT-IR	Fourier Transform Infrared Spectroscopy
fd	Fast delivery
g	Gram
H	Hydrogen
¹H NMR	Proton Nuclear Magnetic Resonance Spectroscopy
H₂O	Water
H₂SO₄	Sulfuric acid
HAuCl₄ · xH₂O	Tetrachloroauric acid hydrate
HO	Alcohol group
HOOC	Carboxylic acid group
HOMO	Highest occupied molecular orbital
HSC6OH	6-mercapto-1-hexanol thiol
HPLC	High performance liquid chromatography
HRTEM	High-Resolution Transmission Electron Microscopy
HSC6	Hexanethiol
HSC6Fc	w-Functionalized ferrocene hexanethiol
Hz	Hertz
h	Hour
I	Intercept
I₂	Iodine
IEC	Ion exchange chromatography
IR	Infrared
i	Current
Di	Current difference
i_{LIM}	Limiting current

i.e.	That is
J	Joule
K	Degrees Kelvin
KBr	Potassium bromide
k	Kilo-
k_B	Boltzmann constant
kD	Kilodaltons
keV	Kiloelectron volts
LUMO	Lowest unoccupied molecular orbital
log	Logarithm
LDI-MS	Laser desorption/ionization mass spectrometry
M	Metal
	Molar
mM	Micromolar
MHz	MegaHertz
MPC	Monolayer-protected cluster
MPC^{As-prep}	as-prepared MPC
m	Meter
	Milli-
mg	Milligram
min	Minute
mL	Milliliter
mM	Millimolar
mol	Mole
mV	Millivolt
N	Newtons
	Nitrogen
N₂	Nitrogen gas
N_A	Avogadro's number
NaBH₄	Sodium borohydride
NaCl	Sodium chloride
NMR	Nuclear magnetic resonance

n	Number of electrons transferred
nA	NanoAmperes
n_{DL}	Number of double-layer electrons
nm	Nanometer
O	Oxygen
⁻OOC	Deprotonated carboxylic acid group
Oct₄NBr	Tetraoctylammonium bromide
OSWV	Osteryoung Square Wave Voltammetry
PDA	Photo diode array
PE	Place exchange
PhC₂S	Phenylethanethiolate
PhC₂ MPCs	Phenylethanethiolate monolayer protected clusters
<i>p</i>-X-PhSH	Para-substituted aryl thiol
Pt	Platinum
PZC	Potential-of-zero charge
pH	$-\log [\text{H}^+]$
QDL	Quantized double-layer
Q_{DL}	Double-layer charge
RS	Alkanethiolate
RSH	Alkanethiol
r	Radius
rpm	Rotations per minute
S	Slope
	Sulfur
S/N	Signal-to-noise ratio
SAM	Self-assembled monolayer
SC₆	Hexanethiolate
SC₆Fc	w -Functionalized ferrocene hexanethiolate
SCE	Saturated Calomel Electrode
SEC	Size exclusion chromatography
SET	Single electron transfer
SP	Surface plasmon

SSCE	Sodium-Saturated Calomel Electrode
STM	Scanning tunneling microscopy
s	Second
T	Temperature
TEM	Transmission electron microscopy
TGA	Thermogravimetric analysis
THF	Tetrahydrofuran
UV-visible	Ultraviolet-visible
V	Volt
DV	Potential difference
v	Volume
vs	Versus
vv	Vice versa
W_{1/2}	Voltammetric peak-width at half-height
X	Times
XPS	X-ray photoelectron spectroscopy
Z	Charge state
d	Chemical shift
e	Dielectric constant
	Molar absorbance coefficient
e_o	Permittivity of free space
f	quantum efficiency
h	Viscosity
l	Wavelength
m	Micro-
n	Scan rate
p	Pi
w	Omega functional group
=	Equals to
	Double bond
+	Positive

–	Negative
—	Single bond
<	Less than
>	More than
×	Multiplied by
μ	Proportional to

CHAPTER I

INTRODUCTION TO MONOLAYER PROTECTED METAL CLUSTERS

1.1 Introduction

While study of the unique properties of colloidal gold has been an increasingly popular field of scientific research, colloidal gold has actually been used for centuries, often as a method of staining glass. The Lycurgus Cup, made of gold and silver colloids, is the oldest example of manipulating the unique optical properties of metal colloids. The cup dates back to the Romans in the fourth century AD and is well known for its unusual coloring.¹ When the cup is viewed in reflected light, for example in the daytime, it appears green, however when light is shone through the cup and transmitted through the glass, the cup appears red. In the seventeenth century, colloids of tin dioxide and gold, known as “Purple of Cassius”, became a popular glass coloring agent.² The creation of unusual colors using metal colloids led to the investigations of Michael Faraday into the colors of gold clusters in the middle of the 1800s, effectively beginning the field of colloidal science.³

Despite the rich history of colloidal chemistry, it is still an exciting and constantly evolving field. Increasingly the field, as well as much of science, is moving toward smaller dimensions. When gold clusters can be reduced down to the lowest end of the nanoscale (< 10 nm), unique physical and chemical properties emerge that can be exploited in applications including biolabeling,^{4,5} luminescent tagging,^{6,7} catalysis,⁸ sensing,⁹⁻¹¹ and

release of chemical reagents in biological systems.¹² Metal clusters require additional support in the form of a chemisorbed monolayer shell, typically with organic thiolated ligands owing to the strong gold-sulfur bond, and, as the clusters get smaller in size, these stabilization supports become increasingly important in determining the structural and chemical properties of the cluster system.¹³⁻¹⁶ The monolayer prevents aggregation of the metal cores and allows for the nanoparticles to be dissolved, dried, and redissolved without alteration or degradation. Ligand-capped gold clusters have been known for a number of years,^{17,18} however only in the past decade has the practical formation of stable and isolatable monolayer protected clusters (MPCs) been demonstrated.¹⁹

1.2 MPC Synthesis

In early 1994, Brust, Schiffrin, and coworkers¹⁹ developed a two-phase (water-toluene) synthesis of stable 1 – 3 nm gold MPCs that penetrated the metal to molecule transition range for this metal. In the original reaction, addition of dodecanethiol to organic phase AuCl_4^- in a 1:1 mole ratio, followed by reduction by BH_4^- , leads to dodecanethiolate-protected gold MPCs:



The “Brust-Schiffrin” synthesis is commonly believed to be a growth, nucleation, and passivation process, however the mechanism is still not completely understood.

Our lab has embraced the Brust-Schiffrin synthesis while extensively modifying it over the years. While the synthesis described usually results in MPCs with a core size distribution, it has been shown that several factors can affect the average gold core size as well as size monodispersity, including (i) larger thiol-gold ratios which give smaller average gold cores,^{20,21} (ii) fast reductant addition and cooler reduction temperatures which result in

more monodisperse and smaller gold cores,^{20,22} and (iii) quenching of the reaction immediately after reduction which produces larger amounts of smaller gold cores (≤ 2 nm).^{23,24}

While the Brust-Schiffrin method is most well-known for creating alkanethiolate protected gold clusters, much research interest has been in the modification of the synthesis, both in terms of the metal core and the stabilizing monolayer. The synthesis has been modified to produce MPCs with different metal cores such as palladium,²⁵⁻²⁷ platinum,^{8,27-29} copper,³⁰ and silver^{27,31-34} as well as bimetal³⁵ cores. The supporting monolayer for organic-soluble MPCs can be made up of organothiolate,^{19,36-38} organophosphine,³⁹⁻⁴¹ or organoamine⁴² ligands, which can undergo further modification through place exchange reactions^{38,39,42-48} leading to heterogeneous ligand shells. Monolayers have also been extensively functionalized, either through place exchange reactions or as the incoming ligand in the Brust-Schiffrin synthesis, with various end groups including redox-active groups⁴⁹⁻⁵³ to investigate multiple electron transfer, electron donating and withdrawing groups⁵⁴ to examine substituent effects on the metal core, and polar groups^{26,32,55,56} to create water-soluble MPCs. As MPCs become increasingly utilized in the fields of catalysis, biosensors, drug delivery agents, and nanoelectronics their synthesis and functionalization continues to be an active area of research.

1.3 MPC Size Dispersion and Separation

Gold MPC synthetic routes all lead to a distribution of metal core sizes that can be tuned through a variety of synthetic conditions.²⁰ The resulting gold nanoparticles are always polydisperse in size, meaning more than one core size is present. Since the physical and chemical properties of the smallest metal clusters are size-dependent, it is desirable to have as monodisperse a sample as possible. Although it is virtually impossible to create a

sample that is completely monodisperse in size, several techniques have been developed that significantly aid the size dispersion challenge. These methods include heating,⁵⁷ etching,⁵⁸ annealing,^{59,60} and vapor treating,^{61,62} however the detailed mechanism behind these techniques are still not well understood. Another route to core size monodispersity is through separation and isolation of the various core sizes. Diverse methods have been developed including solubility solvent fractionation,²² gel electrophoresis,^{63,64} capillary electrophoresis,^{52,65-67} size exclusion chromatography (SEC),⁶⁸⁻⁷¹ ion exchange chromatography (IEC),⁷² ion-pair⁷³ and reverse phase HPLC,⁷⁴⁻⁷⁸ ultracentrifugation,⁷⁹ and molecular imprinting.⁸⁰

While all of these separation techniques have been shown in specific examples to successfully separate MPCs, many of them present significant problems. For example, while solvent fractionation is an excellent method to isolate large amounts of certain cluster sizes, it can be time-consuming, and it is not always possible to find a suitable solvent to separate selected core sizes. Gel electrophoresis and capillary electrophoresis are also favorable techniques, however they have only been shown to work with water-soluble nanoparticles. Disadvantages of chromatographic separations include irreversible adsorption to SEC packing materials and the inapplicability of IEC and ion-pair chromatography for neutral MPCs. Reverse-phase HPLC has emerged as an excellent, high-resolution method for separating organic-soluble MPCs in the 1 – 2 nm core size range. The optimization of HPLC conditions for separating nanoparticles is still a growing area of research owing to the complicated nature of the separation.

1.4 Core Size Dependent Properties of Gold MPCs

Much of the interest in gold MPCs is their size-dependent, or quantized, properties, most evident in their optical and electrochemical traits. The optical properties are apparent in the

absorbance spectra of the different sized gold MPCs. For example, the smaller gold MPCs, with cores originally presumed to be composed of ca. 38 gold atoms but later revealed to be of 25 atoms,⁸¹ reveal step-like transitions over ca. 300 to 500 nm and a weaker band at ca. 700 nm,^{24,82,83} but as the gold core gets larger, these features become smeared out,⁸⁴ until eventually, at ca. 200 gold atoms, a surface plasmon band at ca. 520 nm appears.^{78,85,86} As the gold core increases to even larger clusters, the surface plasmon band becomes more well-defined until eventually the absorbance spectrum resembles that of the bulk metal.

The size-dependent electrochemical properties of gold monolayer protected clusters have been fascinating scientists over the last decade or so and have been extensively investigated by our lab^{59,78,82-84,87-90} and others.^{60,91-94} Voltammetry of MPCs with gold core diameters smaller than ca. 1.6 nm displays a distinct, large space between the first oxidation and the first reduction peak. This spacing has been assigned to the HOMO-LUMO energy bandgap owing to the molecule-like properties of the very small gold clusters.^{82,84}

MPCs with gold core diameters larger than or equal to ca. 1.6 nm exhibit very different voltammetric behavior in that their voltammetry shows a series of evenly spaced peaks, with each peak representing a one electron transfer to or from the gold core. We have coined this phenomenon “quantized double-layer (QDL) charging” as it arises from the cluster’s sub-attofarad capacitance (C_{CLU}) associated with the ionic space charge that forms around an MPC dissolved in a solution of electrolyte.³⁶ Charging of the nanocapacitor by single electrons occurs in potential intervals, $\Delta V = e/C_{CLU}$, where e is the electronic charge, that exceed $k_B T$.^{87,90} The potentials of the electrochemical current peaks seen in voltammetry provide definitive evidence to the charge state of the gold core, and the minimum in the overall capacitance profile presents information on the potential at which

the MPC gold core has zero charge (E_{PZC}).⁹⁵ Figure 1.1 shows the cyclic voltammogram, with gold core charge states labeled, of a solution of highly monodisperse MPCs with an *average* composition of 140 gold atoms and 53 hexanethiolate ligands ($\text{Au}_{140}(\text{SC}_6)_{53}$).

When dissolved in an electrolyte solution, a gold MPC can be considered a concentric sphere capacitor, as shown in Figure 1.2, where the metal core acts as the inner conducting sphere, the organic monolayer as the dielectric, and the boundary of conducting ions as the outer sphere.⁸⁸ The equation for the concentric sphere capacitor model, which relates the cluster capacitance (C_{CLU}) to the core radius (r), is as follows:

$$C_{CLU} = 4\pi\epsilon_0\epsilon\left(\frac{r}{d}\right)(r + d) \quad (3)$$

where ϵ_0 is the permittivity of free space, and ϵ and d are the static dielectric constant and the thickness of the monolayer, respectively. Because C_{CLU} is inversely proportional to ΔV , this equation dictates that as the gold core gets larger in size, the peak potential spacing decreases until $\Delta V < k_B T$ (thermal spreading, ca. 26 mV at 298 K), where the voltammetry is seen as an unresolved current continuum more characteristic of bulk gold. Electrochemical and optical analysis of gold MPCs continues to exploit the core-size dependent properties and has led to many interesting discoveries that should aid researchers in their fundamental understanding of small metal clusters.

1.5 Determination of Number of Gold Core Atoms

With the smallest metal cluster sizes, very small changes in the core size and structure can lead to dramatic changes in the electronic properties; thus there is a great importance in determining clusters' atom counts and configurations. Evidence supports that there are specific closed-shell configurations that are favored by gold clusters and identified as "magic numbers."^{22,96-100} Much theory has been devoted to uncovering the number of

Figure 1.1. Cyclic voltammogram of 0.2 mM $\text{Au}_{140}(\text{SC}_6)_{53}$ in CH_2Cl_2 with 0.1 M Bu_4NClO_4 at 283 K with scan rate of 0.1 V/s.

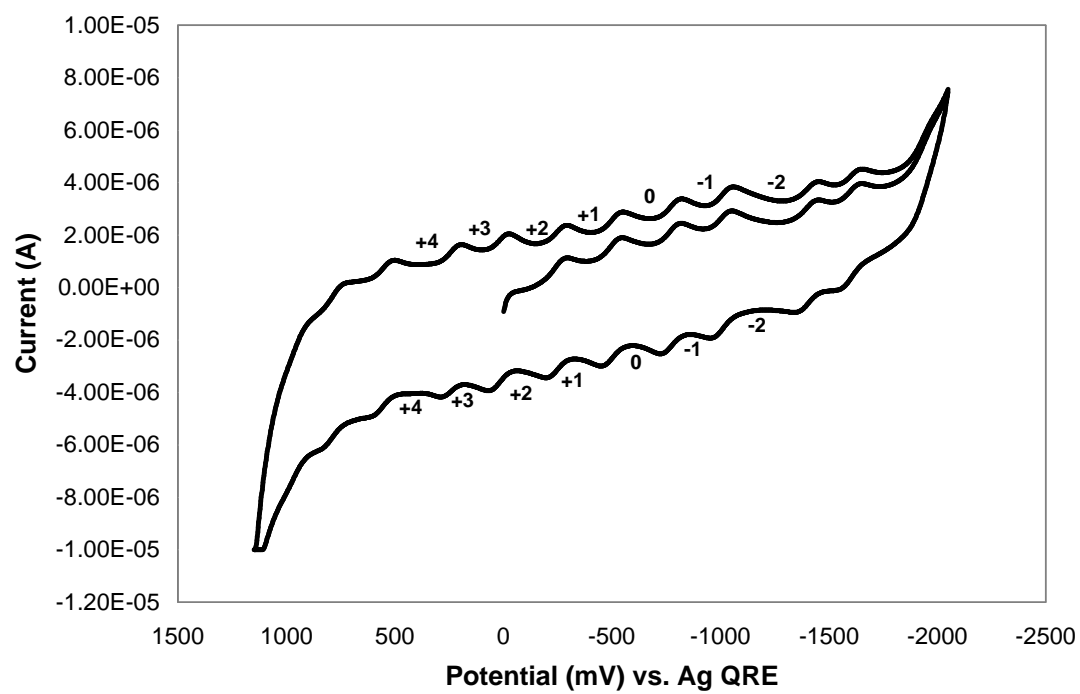
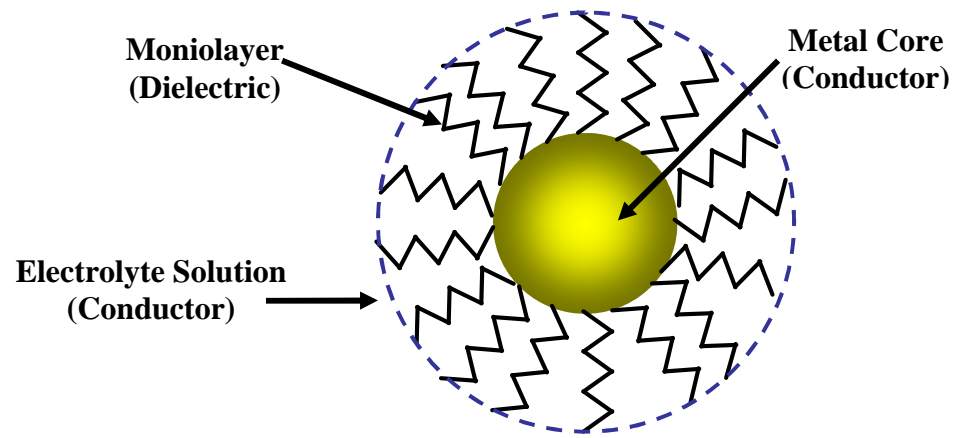


Figure 1.2. Concentric sphere capacitor model for a monolayer protected gold cluster.



$$C_{CLU} = 4\pi\epsilon_0\epsilon\left(\frac{r}{d}\right)(r + d)$$

atoms of small gold clusters and their structures including a series of gold clusters spanning the size range from Au₆ to Au₁₄₇ with core diameters of 0.7 to 1.7 nm studied by Rösch *et. al.*⁹⁷ Their theoretical investigation was aimed to analyze the convergence of cluster properties toward the corresponding bulk metal values. In their research, they calculated positive gold 4*f* core level binding energy shifts for the surface sites, which distinguish among the corner, edge, and face-centered sites, providing theoretical evidence of a heterogeneous gold core surface.

In another theoretical study, Landman *et. al.* investigated slightly larger gold clusters, analyzing the structures of clusters ranging from Au₄₀ to Au₂₀₀⁹⁹ and reporting a discrete sequence of optimal clusters with different structural motifs, in particular focusing on the decahedral structures. Whetten *et. al.* showed, through atomistic modeling and x-ray powder diffraction analysis, that many of the MPC gold cores, including Au₁₄₀ and Au₂₂₅, prefer the truncated octahedral (TO) shells, in particular the TO⁺ shape which is defined as $(0 < n - m \leq 4)$, where n is the number of atoms between (111) facets, and m is the number of atoms between (111) and (100) facets.¹⁰⁰ Most analytical techniques are insufficient to determine the extent of truncation so the actual atom count has some uncertainty, for example it is likely that a sample of Au₁₄₀ MPCs also contains some clusters with cores of Au₁₄₂ or Au₁₄₄.

While theoretical studies of gold clusters have been well documented, there has also been intriguing experimental work devoted to learning more about the atom counts and structures of gold clusters. Although electron microscopy has been a valuable tool in the study of large metal colloids, at the sub-2-nm scale the technique is insufficient in distinguishing clusters that differ only by several core atoms.¹⁰¹⁻¹⁰⁴ Single crystal X-ray diffraction is a more effective method of precisely determining the cluster atom count and

structure of both the metal cluster and organic monolayer with which electronic properties can be correlated.¹⁰⁵⁻¹¹⁵ However, most clusters of recent interest have not been successfully crystallized owing to the polydispersity, or size distribution, of the cluster samples.¹¹⁶

Several other analytical techniques are showing promise in the determination of precise cluster core stoichiometry and structure. One such technique is mass spectrometry, both with matrix-assisted laser desorption ionization (MALDI) and electrospray ionization (ESI).^{63,64,81,116-118} Despite the fact that mass spectrometry is emerging as a valuable technique in core size determination, the analysis still has several difficulties to overcome, including resolving multiple core sizes in polydisperse samples. Another promising new technique, quantitative high-angle annular dark-field scanning transmission electron microscopy (HAADF-STEM), is being employed by Nuzzo *et. al.* to determine atomic compositions and monodispersity of monolayer protected gold clusters.^{119,120} HAADF-STEM has the ability to provide both images as well as atom counts of individual monolayer protected clusters with sub-nanometer gold cores. While great strides have been made in the search for analytical techniques that can provide precise atomic and structural information of polydisperse cluster samples, it is still very much an active area of research.

1.6 References

- (1) <http://www.thebritishmuseum.ac.uk/science/lycorguscup/sr-lycugus-p1.html>.
- (2) Thiessen, P. A. *Kolloid Z.* **1942**, *101*, 241-248.
- (3) Faraday, M. *Philos. Trans. R. Soc.* **1857**, *147*, 145-147.
- (4) Aubin, M. E.; Morales, D. G.; Hamad-Schifferli, K. *Nano Lett.* **2005**, *5*, 519-522.
- (5) Grancharov, S. G.; Zeng, H.; Sun, S. H.; Wang, S. X.; O'Brien, S.; Murray, C. B.; Kirtley, J. R.; Held, G. A. *J. Phys. Chem. B* **2005**, *109*, 13030-13035.
- (6) Li, Z. F.; Ruckenstein, E. *Nano Lett.* **2004**, *4*, 1463-1467.
- (7) Gao, X. H.; Nie, S. M. *Anal. Chem.* **2004**, *76*, 2406-2410.
- (8) Eklund, S. E.; Cliffl, D. E. *Langmuir* **2004**, *20*, 6012-6018.
- (9) McFarland, A. D.; Van Duyne, R. P. *Nano Lett.* **2003**, *3*, 1057-1062.
- (10) Riboh, J. C.; Haes, A. J.; McFarland, A. D.; Yonzon, C. R.; Van Duyne, R. P. *J. Phys. Chem. B* **2003**, *107*, 1772-1780.
- (11) Malinsky, M. D.; Kelly, K. L.; Schatz, G. C.; Van Duyne, R. P. *J. Am. Chem. Soc.* **2001**, *123*, 1471-1482.
- (12) Rothrock, A. R.; Donkers, R. L.; Schoenfish, M. H. *J. Am. Chem. Soc.* **2005**, *127*, 9362-9363.
- (13) Chao, K. J.; Cheng, M. H.; Ho, Y. F.; Liu, P. H. *Catal. Today* **2004**, *97*, 49-53.
- (14) Haruta, M. *Catal. Today* **1997**, *36*, 153-166.
- (15) Hills, C. W.; Nashner, M. S.; Frenkel, A. I.; Shapley, J. R.; Nuzzo, R. G. *Langmuir* **1999**, *15*, 690-700.
- (16) Zhang, P.; Sham, T. K. *Appl. Phys. Lett.* **2002**, *81*, 736-738.
- (17) Schmid, G. *Clusters and Colloids*; VCH: Weinheim, 1994.
- (18) Hayat, M. A. *Colloidal Gold: Principles, Methods, and Applications*; Academic Press: San Diego, 1991.
- (19) Brust, M.; Walker, M.; Bethell, D.; Schiffrin, D. J.; Whyman, R. *J. Chem. Soc.-Chem. Commun.* **1994**, 801-802.

- (20) Hostetler, M. J.; Wingate, J. E.; Zhong, C.-J.; Harris, J. E.; Vachet, R. W.; Clark, M. R.; Londono, J. D.; Green, S. J.; Stokes, J. J.; Wignall, G. D.; Glish, G. L.; Porter, M. D.; Evans, N. D.; Murray, R. W. *Langmuir* **1998**, *14*, 17-30.
- (21) Leff, D. V.; Ohara, P. C.; Heath, J. R.; Gelbart, W. M. *J. Phys. Chem.* **1995**, *99*, 7036-7041.
- (22) Whetten, R. L.; Khoury, J. T.; Alvarez, M. M.; Murthy, S.; Vezmar, I.; Wang, Z. L.; Stephens, P. W.; Cleveland, C. L.; Luedtke, W. D.; Landman, U. *Adv. Mater.* **1996**, *8*, 428-&.
- (23) Alvarez, M. M.; Khoury, J. T.; Schaaff, T. G.; Shafigullin, M.; Vezmar, I.; Whetten, R. L. *Chem. Phys. Lett.* **1997**, *266*, 91-98.
- (24) Schaaff, T. G.; Shafigullin, M. N.; Khoury, J. T.; Vezmar, I.; Whetten, R. L.; Cullen, W. G.; First, P. N.; GutierrezWing, C.; Ascensio, J.; JoseYacaman, M. J. *J. Phys. Chem. B* **1997**, *101*, 7885-7891.
- (25) Zamborini, F. P.; Gross, S. M.; Murray, R. W. *Langmuir* **2001**, *17*, 481-488.
- (26) Clifffel, D. E.; Zamborini, F. P.; Gross, S. M.; Murray, R. W. *Langmuir* **2000**, *16*, 9699-9702.
- (27) Tan, Y. W.; Dai, X. H.; Li, Y. F.; Zhu, D. B. *J. Mater. Chem.* **2003**, *13*, 1069-1075.
- (28) Yang, J.; Lee, J. Y.; Deivaraj, T. C.; Too, H. P. *Colloid Surf. A-Physicochem. Eng. Asp.* **2004**, *240*, 131-134.
- (29) Kim, K. S.; DembereInyamba, D.; Lee, H. *Langmuir* **2004**, *20*, 556-560.
- (30) Chen, S. W.; Sommers, J. M. *J. Phys. Chem. B* **2001**, *105*, 8816-8820.
- (31) Murthy, S.; Bigioni, T. P.; Wang, Z. L.; Khoury, J. T.; Whetten, R. L. *Mater. Lett.* **1997**, *30*, 321-325.
- (32) Chen, S. H.; Kimura, K. *Chem. Lett.* **1999**, 1169-1170.
- (33) Shon, Y. S.; Cutler, E. *Langmuir* **2004**, *20*, 6626-6630.
- (34) Branham, M. R.; Douglas, A. D.; Mills, A. J.; Tracy, J. B.; White, P. S.; Murray, R. W. *Langmuir* **2006**, *22*, 11376-11383.
- (35) Shon, Y. S.; Dawson, G. B.; Porter, M.; Murray, R. W. *Langmuir* **2002**, *18*, 3880-3885.
- (36) Templeton, A. C.; Wuelfing, M. P.; Murray, R. W. *Accounts of Chemical Research* **2000**, *33*, 27-36.

- (37) Whetten, R. L.; Shafigullin, M. N.; Khoury, J. T.; Schaaff, T. G.; Vezmar, I.; Alvarez, M. M.; Wilkinson, A. *Accounts of Chemical Research* **1999**, *32*, 397-406.
- (38) Brown, L. O.; Hutchison, J. E. *J. Am. Chem. Soc.* **1997**, *119*, 12384-12385.
- (39) Petroski, J.; Chou, M. H.; Creutz, C. *Inorg. Chem.* **2004**, *43*, 1597-1599.
- (40) Weare, W. W.; Reed, S. M.; Warner, M. G.; Hutchison, J. E. *J. Am. Chem. Soc.* **2000**, *122*, 12890-12891.
- (41) Schmid, G. *Chem. Rev.* **1992**, *92*, 1709-1727.
- (42) Brown, L. O.; Hutchison, J. E. *J. Am. Chem. Soc.* **1999**, *121*, 882-883.
- (43) Boal, A. K.; Das, K.; Gray, M.; Rotello, V. M. *Chem. Mat.* **2002**, *14*, 2628-2636.
- (44) Donkers, R. L.; Song, Y.; Murray, R. W. *Langmuir* **2004**, *20*, 4703-4707.
- (45) Guo, R.; Song, Y.; Wang, G. L.; Murray, R. W. *J. Am. Chem. Soc.* **2005**, *127*, 2752-2757.
- (46) Hostetler, M. J.; Templeton, A. C.; Murray, R. W. *Langmuir* **1999**, *15*, 3782-3789.
- (47) Song, Y.; Murray, R. W. *J. Am. Chem. Soc.* **2002**, *124*, 7096-7102.
- (48) Song, Y.; Huang, T.; Murray, R. W. *J. Am. Chem. Soc.* **2003**, *125*, 11694-11701.
- (49) Hostetler, M. J.; Green, S. J.; Stokes, J. J.; Murray, R. W. *J. Am. Chem. Soc.* **1996**, *118*, 4212-4213.
- (50) Ingram, R. S.; Murray, R. W. *Langmuir* **1998**, *14*, 4115-4121.
- (51) Miles, D. T.; Murray, R. W. *Anal. Chem.* **2001**, *73*, 921-929.
- (52) Templeton, A. C.; Cliffler, D. E.; Murray, R. W. *J. Am. Chem. Soc.* **1999**, *121*, 7081-7089.
- (53) Wolfe, R. L.; Balasubramanian, R.; Tracy, J. B.; Murray, R. W. *Langmuir* **2007**, *23*, 2247-2254.
- (54) Guo, R.; Murray, R. W. *J. Am. Chem. Soc.* **2005**, *127*, 12140-12143.
- (55) Shon, Y. S.; Wuelfing, W. P.; Murray, R. W. *Langmuir* **2001**, *17*, 1255-1261.
- (56) Templeton, A. C.; Chen, S. W.; Gross, S. M.; Murray, R. W. *Langmuir* **1999**, *15*, 66-76.

- (57) Devenish, R. W.; Goulding, T.; Heaton, B. T.; Whyman, R. *J. Chem. Soc.-Dalton Trans.* **1996**, 673-679.
- (58) Schaaff, T. G.; Whetten, R. L. *J. Phys. Chem. B* **1999**, *103*, 9394-9396.
- (59) Hicks, J. F.; Miles, D. T.; Murray, R. W. *J. Am. Chem. Soc.* **2002**, *124*, 13322-13328.
- (60) Quinn, B. M.; Liljeroth, P.; Ruiz, V.; Laaksonen, T.; Kontturi, K. *J. Am. Chem. Soc.* **2003**, *125*, 6644-6645.
- (61) Maye, M. M.; Zheng, W. X.; Leibowitz, F. L.; Ly, N. K.; Zhong, C. J. *Langmuir* **2000**, *16*, 490-497.
- (62) Zhong, C. J.; Zhang, W. X.; Leibowitz, F. L.; Eichelberger, H. H. *Chem. Commun.* **1999**, 1211-1212.
- (63) Schaaff, T. G.; Whetten, R. L. *Journal of Physical Chemistry B* **2000**, *104*, 2630-2641.
- (64) Schaaff, T. G.; Knight, G.; Shafigullin, M. N.; Borkman, R. F.; Whetten, R. L. *Journal of Physical Chemistry B* **1998**, *102*, 10643-10646.
- (65) Schnabel, U.; Fischer, C. H.; Kenndler, E. *J. Microcolumn Sep.* **1997**, *9*, 529-534.
- (66) Rodriguez, M. A.; Armstrong, D. W. *J. Chromatogr. B* **2004**, *800*, 7-25.
- (67) Liu, F. K.; Ko, F. H.; Huang, P. W.; Wu, C. H.; Chu, T. C. *J. Chromatogr. A* **2005**, *1062*, 139-145.
- (68) Wei, G. T.; Liu, F. K.; Wang, C. R. *C. Anal. Chem.* **1999**, *71*, 2085-2091.
- (69) Wei, G. T.; Liu, F. K. *J. Chromatogr. A* **1999**, *836*, 253-260.
- (70) Fischer, C. H.; Lilie, J.; Weller, H.; Katsikas, L.; Henglein, A. *Ber. Bunsen-Ges. Phys. Chem. Chem. Phys.* **1989**, *93*, 61-64.
- (71) Siebrands, T.; Giersig, M.; Mulvaney, P.; Fischer, C. H. *Langmuir* **1993**, *9*, 2297-2300.
- (72) Bos, W.; Steggerda, J. J.; Yan, S. P.; Casalnuovo, J. A.; Muetting, A. M.; Pignolet, L. H. *Inorg. Chem.* **1988**, *27*, 948-951.
- (73) Choi, M. M. F.; Douglas, A. D.; Murray, R. W. *Analytical Chemistry* **2006**, *78*, 2779-2785.

- (74) Song, Y.; Jimenez, V.; McKinney, C.; Donkers, R.; Murray, R. W. *Anal. Chem.* **2003**, 75, 5088-5096.
- (75) Song, Y.; Heien, M.; Jimenez, V.; Wightman, R. M.; Murray, R. W. *Anal. Chem.* **2004**, 76, 4911-4919.
- (76) Jimenez, V. L.; Leopold, M. C.; Mazzitelli, C.; Jorgenson, J. W.; Murray, R. W. *Anal. Chem.* **2003**, 75, 199-206.
- (77) Fischer, C. H.; Weller, H.; Katsikas, L.; Henglein, A. *Langmuir* **1989**, 5, 429-432.
- (78) Wolfe, R. L.; Murray, R. W. *Anal. Chem.* **2006**, 78, 1167-1173.
- (79) Calabretta, M.; Jamison, J. A.; Falkner, J. C.; Liu, Y. P.; Yuhas, B. D.; Matthews, K. S.; Colvin, V. L. *Nano Lett.* **2005**, 5, 963-967.
- (80) Koenig, S.; Chechik, V. *Chem. Commun.* **2005**, 4110-4112.
- (81) Tracy, J. B.; Kalyuzhny, G.; Crowe, M. C.; Balasubramanian, R.; Choi, J. P.; Murray, R. W. *J. Am. Chem. Soc.* **2007**, 129, 6706-6707.
- (82) Jimenez, V. L.; Georganopoulou, D. G.; White, R. J.; Harper, A. S.; Mills, A. J.; Lee, D. I.; Murray, R. W. *Langmuir* **2004**, 20, 6864-6870.
- (83) Lee, D.; Donkers, R. L.; Wang, G. L.; Harper, A. S.; Murray, R. W. *J. Am. Chem. Soc.* **2004**, 126, 6193-6199.
- (84) Balasubramanian, R.; Guo, R.; Mills, A. J.; Murray, R. W. *J. Am. Chem. Soc.* **2005**, 127, 8126-8132.
- (85) Alvarez, M. M.; Khoury, J. T.; Schaaff, T. G.; Shafigullin, M. N.; Vezmar, I.; Whetten, R. L. *J. Phys. Chem. B* **1997**, 101, 3706-3712.
- (86) Kreibig, U.; Vollmer, M. *Optical Properties of Metal Clusters*; Springer-Verlag: New York, 1995.
- (87) Ingram, R. S.; Hostetler, M. J.; Murray, R. W.; Schaaff, T. G.; Khoury, J. T.; Whetten, R. L.; Bigioni, T. P.; Guthrie, D. K.; First, P. N. *J. Am. Chem. Soc.* **1997**, 119, 9279-9280.
- (88) Hicks, J. F.; Templeton, A. C.; Chen, S. W.; Sheran, K. M.; Jasti, R.; Murray, R. W.; Debord, J.; Schaaf, T. G.; Whetten, R. L. *Anal. Chem.* **1999**, 71, 3703-3711.
- (89) Chen, S. W.; Murray, R. W.; Feldberg, S. W. *J. Phys. Chem. B* **1998**, 102, 9898-9907.

- (90) Chen, S. W.; Ingram, R. S.; Hostetler, M. J.; Pietron, J. J.; Murray, R. W.; Schaaff, T. G.; Khoury, J. T.; Alvarez, M. M.; Whetten, R. L. *Science* **1998**, *280*, 2098-2101.
- (91) Yang, Y.; Pradhan, S.; Chen, S. *Journal of American Chemical Society* **2004**, *126*, 76-77.
- (92) Kim, Y. G.; Garcia-Martinez, J. C.; Crooks, R. M. *Langmuir* **2005**, *21*, 5485-5491.
- (93) Chaki, N. K.; Kakade, B.; Sharma, J.; Mahima, S.; Vijayamohanan, K. P.; Haram, S. K. *J. Appl. Phys.* **2004**, *96*, 5032-5036.
- (94) Chaki, N. K.; Singh, P.; Dharmadhikari, C. V.; Vijayamohanan, K. P. *Langmuir* **2004**, *20*, 10208-10217.
- (95) Chen, S. W.; Murray, R. W. *J. Phys. Chem. B* **1999**, *103*, 9996-10000.
- (96) Cleveland, C. L.; Landman, U.; Schaaff, T. G.; Shafigullin, M. N.; Stephens, P. W.; Whetten, R. L. *Phys. Rev. Lett.* **1997**, *79*, 1873-1876.
- (97) Haberlen, O. D.; Chung, S. C.; Stener, M.; Rosch, N. *J. Chem. Phys.* **1997**, *106*, 5189-5201.
- (98) Hakkinen, H.; Barnett, R. N.; Landman, U. *Phys. Rev. Lett.* **1999**, *82*, 3264-3267.
- (99) Barnett, R. N.; Cleveland, C. L.; Hakkinen, H.; Luedtke, W. D.; Yannouleas, C.; Landman, U. *Eur. Phys. J. D* **1999**, *9*, 95-104.
- (100) Cleveland, C. L.; Landman, U.; Shafigullin, M. N.; Stephens, P. W.; Whetten, R. L. *Z. Phys. D-Atoms Mol. Clusters* **1997**, *40*, 503-508.
- (101) Yang, J. C.; Bradley, S.; Gibson, J. M. *Mater. Charact.* **2003**, *51*, 101-107.
- (102) Yang, J. C.; Bradley, S.; Gibson, J. M. *Microsc. microanal.* **2000**, *6*, 353-357.
- (103) Singhal, A.; Yang, J. C.; Gibson, J. M. *Ultramicroscopy* **1997**, *67*, 191-206.
- (104) Treacy, M. M. J.; Rice, S. B. *J. Microsc.-Oxf.* **1989**, *156*, 211-234.
- (105) Teo, B. K.; Shi, X. B.; Zhang, H. *J. Am. Chem. Soc.* **1992**, *114*, 2743-2745.
- (106) Briant, C. E.; Gardner, C. J.; Hor, T. S. A.; Howells, N. D.; Mingos, D. M. P. *J. Chem. Soc.-Dalton Trans.* **1984**, 2645-2651.
- (107) Briant, C. E.; Smith, R. G.; Mingos, D. M. P. *J. Chem. Soc.-Chem. Commun.* **1984**, 586-588.

- (108) Briant, C. E.; Hall, K. P.; Mingos, D. M. P. *J. Chem. Soc.-Chem. Commun.* **1984**, 290-291.
- (109) Briant, C. E.; Hall, K. P.; Wheeler, A. C.; Mingos, D. M. P. *J. Chem. Soc.-Chem. Commun.* **1984**, 248-250.
- (110) Smits, J. M. M.; Bour, J. J.; Vollenbroek, F. A.; Beurskens, P. T. *Journal of Crystallographic and Spectroscopic Research* **1983**, 13, 355-363.
- (111) Smits, J. M. M.; Beurskens, P. T.; Bour, J. J.; Vollenbroek, F. A. *Journal of Crystallographic and Spectroscopic Research* **1983**, 13, 365-372.
- (112) Smits, J. M. M.; Beurskens, P. T.; Vandervelden, J. W. A.; Bour, J. J. *Journal of Crystallographic and Spectroscopic Research* **1983**, 13, 373-379.
- (113) Bellon, P.; Manasser, M.; Sansoni, M. *J. Chem. Soc.-Dalton Trans.* **1973**, 2423-2427.
- (114) Albano, V. G.; Bellon, P. L.; Ciani, G. *J. Chem. Soc.-Dalton Trans.* **1972**, 1938-&.
- (115) Albano, V. G.; Bellon, P. L.; Manasser, M.; Ciani, G. *J. Chem. Soc.-Dalton Trans.* **1972**, 171-&.
- (116) Schaaff, T. G. *Anal. Chem.* **2004**, 76, 6187-6196.
- (117) Negishi, Y.; Nobusada, K.; Tsukuda, T. *J. Am. Chem. Soc.* **2005**, 127, 5261-5270.
- (118) Zhang, H. F.; Stender, M.; Zhang, R.; Wang, C. M.; Li, J.; Wang, L. S. *J. Phys. Chem. B* **2004**, 108, 12259-12263.
- (119) Menard, L. D.; Gao, S. P.; Xu, H. P.; Twisten, R. D.; Harper, A. S.; Song, Y.; Wang, G. L.; Douglas, A. D.; Yang, J. C.; Frenkel, A. I.; Nuzzo, R. G.; Murray, R. W. *J. Phys. Chem. B* **2006**, 110, 12874-12883.
- (120) Menard, L. D.; Xu, H. P.; Gao, S. P.; Twisten, R. D.; Harper, A. S.; Song, Y.; Wang, G. L.; Douglas, A. D.; Yang, J. C.; Frenkel, A. I.; Murray, R. W.; Nuzzo, R. G. *J. Phys. Chem. B* **2006**, 110, 14564-14573.

CHAPTER II

ANALYTICAL EVIDENCE FOR THE MONOLAYER PROTECTED CLUSTER



2.1 Introduction

Metal nanoparticles have been of great interest over the past decade, due in part to the entry they offer to the bridge between bulk and molecular behaviour of chemical materials.¹ Nanometer-scale materials present new chemical, electronic, and physical properties, which can be size-dependent,¹ and which have been useful in applications including instrumentation improvement,^{2,3} biological detection,^{4,5} and catalysis promotion.^{6,7} When surrounded by self-assembled monolayer shells, the stability of nanometer-sized clusters can be dramatically improved, thereby increasing the accessibility of chemical experimentation with the clusters. In the case of thiolate monolayer-coated Au cores, such nanoparticles have been dubbed monolayer-protected clusters (MPCs).¹

The initial report by Brust et. al⁸ of the organic-phase synthesis of thiolate monolayer-protected Au MPCs has been followed by growing interest in their exploration. Much literature has been produced on Au MPCs with cores ranging from 11 to 140 Au atoms, but little about relatively “larger” Au cores. It is known that very small metal clusters (with core diameters $< \sim 1.6$ nm) display molecule-like properties, while relatively larger clusters (with core diameters $> \sim 10$ nm) demonstrate properties of a bulk sample of the core metal.⁹ Exploring the intermediate sizes of metal cores offers a better understanding of the properties lying between molecular and bulk behaviour.

Many properties of Au MPCs are quantized, or size-dependent; consequently, gaining knowledge on different core-sized MPCs will be valuable in understanding these properties. Size-dependent MPC properties particularly appear in electrochemical and optical properties. The latter vary greatly with the size of the Au core;¹⁰⁻¹⁸ the absorbance spectra of MPCs with small Au cores (diameter <1.6 nm) exhibit distinct step-like transitions over ~300 to 500 nm and a weaker band at ~700 nm. These features are lost with increasing size—Au₁₄₀ cores have nearly featureless spectra, and for larger Au cores, a surface plasmon resonance absorbance peak appears at ~520 nm. This band's intensity is strongly correlated with the size of the metallic core,⁹ increasing with core size until the spectrum resembles that of the bulk metal.

The electrochemical properties of Au MPCs have been investigated by us¹⁹⁻²⁷ and others.²⁸⁻³¹ Au MPCs with core diameters less than about 1.6 nm display molecule-like electrochemistry with a clear energy gap that can be related to their optical absorbance band edge. MPCs with core diameters = 1.6 nm (Au₁₄₀) display capacitor-like quantized double-layer (QDL) charging in their voltammetry. The potentials of one electron core charge increments are separated by $\Delta V = e/C_{\text{CLU}}$ where e is the electron charge and C_{CLU} is the electrostatically-governed double layer capacitance of individual MPCs. C_{CLU} grows with MPC core size, so that ultimately, ΔV spacings between adjacent one electron steps become too small to resolve when their values approach $k_{\text{B}}T$ (which at 298 K equals *ca.* 26 mV). Besides Au₁₄₀,^{20,21} there has been only one previous description³¹ of QDL of very large core clusters (diameter 3.7 nm, *ca.* 1400 Au atoms), and judging from the pulse voltammetry peak widths reported (50-55 mV), achieving voltammetric resolution was in part because of surface adsorption effects.³² Thus, Au MPCs in the size range above 140 Au atoms are of continuing interest.

Presented here is the synthesis and investigation of hexanethiolate-protected MPCs with 225 Au atom cores. These nanoparticles, like Au₁₄₀ MPCs, display size-dependent properties, notably quantized double layer charging in their voltammetry. The behaviour of these MPCs, with core radii of 1.0 nm, thus differs from that of bulk metal. The determination of the size and exploration of the properties of these MPCs are performed using transmittance electron microscopy (TEM), thermal gravimetric analysis (TGA), electrochemical voltammetry, UV/vis absorbance spectrophotometry, and high performance liquid chromatography with absorbance and electrochemical detection. This report constitutes a more exacting study than our previous, unrefined preparation of dodecane thiolate-protected MPCs,⁹ that was modelled as producing a mixture of Au₂₂₅ and Au₃₁₄ that displayed no QDL features.

Our laboratory has previously described using high performance liquid chromatography, with columns of stationary phase C8 and phenyl in series, to separate Au MPCs of varying core sizes.²² The MPCs can be detected optically, using a photodiode array (PDA) detector,²² and amperometrically, using an electrochemical flow cell detector^{25,33} to measure currents due to electronic charging of the cores. In the latter detector, the MPCs in eluted bands transfer electrons so as to equilibrate their Fermi levels with that of the applied electrode potential. The peak current detected depends on the potential applied to the flow cell working electrode and on the double layer capacitance of the nanoparticle, which in turn depends on the MPC monolayer thickness (d) and core radius (r). We have shown that the PDA and electrochemical detectors can be used in a ratiometric manner to determine the size of the eluted MPCs,³³ and here apply this method to the Au₂₂₅ MPCs.

2.2 Experimental Section

Chemicals. Hexanethiol (HSC6, >99%), tetraoctylammonium bromide (Oct₄NBr, >98%), sodium borohydride (NaBH₄, >98%), and tetrabutylammonium perchlorate (Bu₄NClO₄, >99%) were used as received from Aldrich, as were toluene (Fisher, reagent grade), acetonitrile (Fisher, Optima), methylene chloride (Fisher, HPLC grade), and ethanol (HPLC grade). HAuCl₄·xH₂O (from 99.999% pure gold) was synthesized using a literature procedure³⁴ and stored in a freezer at -20 °C. Water was purified using a Barnstead NANOpure system (18 MO).

Synthesis of MPCs. MPCs were prepared as in previous work.⁹ Briefly, 3.19 g of HAuCl₄·xH₂O in 100 mL of deionized water was added to a vigorously stirred solution of 5.20 g of Oct₄NBr in 200 mL of toluene. The HAuCl₄·xH₂O aqueous solution changed from yellow to clear and the toluene solution from clear to orange-brown as the AuCl₄⁻ was transferred from the aqueous to the organic phase. A 2-fold molar excess, relative to gold, of hexanethiol (2.29 mL) was added to the isolated organic phase which was then stirred for 20 minutes at room temperature. Reduction to a dark solution was accomplished—while rapidly stirring at 0 °C—by quickly adding 10 mL of an aqueous solution containing 3.8 g of NaBH₄. Stirring was continued for 1 hour at 0 °C; the organic phase was then collected and the solvent removed on a rotary evaporator at room temperature. The black product was suspended in 200 mL of ethanol for 2 hours. Using a glass frit, the product was collected and cleaned with 600 mL of ethanol and 200 mL of acetonitrile.

Thermal Analysis. Thermogravimetric analysis (TGA) was performed with a Seiko RTG 220 robotic TGA. The MPC sample of 6 mg was placed in an Al crucible within a Pt crucible. The sample was heated from 30 °C to 600 °C at 15 °C per minute.

High-Resolution Transmission Electron Microscopy (TEM). TEM measurements were performed on MPC samples that were dropcast (from ~1 mg/mL in CH₂Cl₂ solution)

onto standard carbon-coated (200-300 Å) Formvar films on copper grids (600 mesh) and dried in air for at least 1 hour before imaging. Phase-contrast images of the particles were obtained using a side-entry Phillips CM12 electron microscope operating at 120 keV. Images were obtained at 580,000 X magnification. Au core diameters were measured using Scion Image Release Beta 3b (1998) software on enlarged TEM image photographs.

Spectroscopy. UV-vis spectra were collected with a Shimadzu UV-Vis (Model UV-1601) spectrometer. MPC solutions in CH_2Cl_2 were freshly prepared before each measurement.

Electrochemistry. Voltammetry was done with a Bioanalytical Systems, Inc. (BAS) Electrochemical Analyzer, Model 100B, in 0.1 M Bu_4NClO_4 in CH_2Cl_2 solutions that were degassed and blanketed with high-purity Ar during the experiment. The working electrode was a 0.4 mm Pt disk, the counter electrode a Pt wire, and the reference electrode a Ag/AgCl (aqueous) electrode. The working electrode was polished with 0.05 μm Al_2O_3 slurry and cleaned electrochemically by potential cycling in 0.1 M H_2SO_4 solution. Cyclic voltammetry was done at 100 mV/s, and Osteryoung square wave voltammetry was done with potential steps of 4 mV, square wave amplitude of 25 mV, square wave frequency of 15 s^{-1} , and quiet time of 2 s.

High-Performance Liquid Chromatography (HPLC). HPLC was performed on CH_2Cl_2 solutions containing ca. 1.0 mg/mL Au_{140} and ca. 0.5 mg/mL Au_{225} using a Waters 600 controller pump and a Rheodyne 7725 injection valve with a 50- μL loop. Two different configurations were used, one being a stainless-steel silica-bonded BioBasic C8 stationary phase column (250 x 4.6 mm i.d.) in series with a stainless-steel silica-bonded BioBasic phenyl column (150 x 4.6 mm i.d., Thermo Hypersil, Keystone Scientific Operations). Both columns had particle sizes of 5 μm with 300 Å pore size. The second

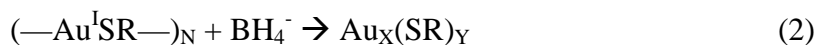
configuration, performed to test for reproducibility of MPC core size results, was a serial combination of stainless-steel inorganic/organic hybrid particle-bonded XTerra C8 stationary phase column (250 x 4.6 mm i.d.) and a stainless-steel inorganic/organic hybrid particle-bonded XTerra phenyl column (150 x 4.6 mm i.d., Waters Corporation), both with particle sizes of 5 μm and 125 \AA pore size. Columns were at room temperature. The mobile phase for both column sets was CH_2Cl_2 (with 0.1 M Bu_4NClO_4 as supporting electrolyte for the amperometry) at a flow rate of 0.7 mL/min.

To measure optical absorbance, a Waters 996 PDA detection system was used to display absorbance at 400 nm. For electrochemical detection, a cross-flow LC-44 thin-layer electrochemical cell (Bioanalytical Systems, Inc.) was connected in-line after the Waters HPLC PDA detector. The working electrode was a $\sim 3\text{-mm}$ diameter glassy carbon, the reference electrode was Ag/AgCl (aqueous), and the counter electrode was the stainless steel electrochemical cell body itself. Signals were read by a locally constructed battery-powered potentiostat (UNC chemistry department electronics shop), converted through a Waters A/D converter, and monitored by the same software used to record the PDA chromatograms. Current responses were collected in successive, repeated chromatograms with the detector working electrode set at varying potentials, so as to define, point-by-point, one-electron hydrodynamic voltammetric steps for each eluted nanoparticle peak.

2.3 Results and Discussion

Synthesis and Analytical Characterization of Au_{225} MPCs. In the original Brust reaction,⁸ reaction of a 1:1 molar ratio of dodecanethiol and AuCl_4^- followed by reduction with BH_4^- , led to dodecanethiolate-protected Au MPCs having core diameters of 1 – 3 nm. The general reaction is

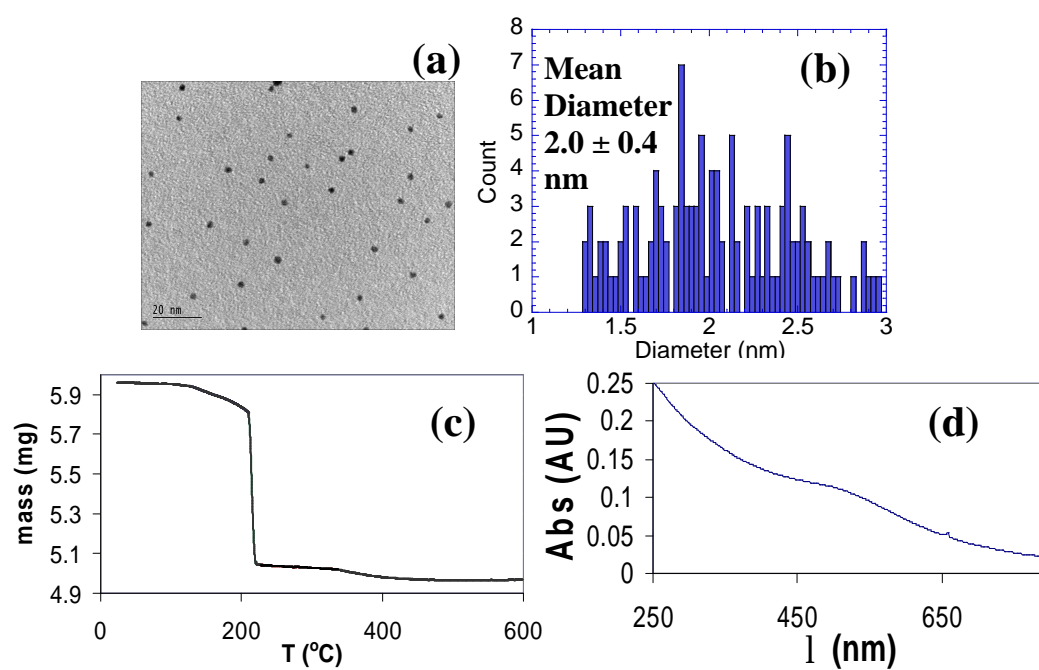




That initial report has been followed by many others, using different alkanethiols and varied reaction conditions. While the complexity of the Brust reaction still defies a truly detailed understanding, and reaction products are invariably poly-disperse in core size, its importance is in facile production of a range of smaller nanoparticle sizes than other synthetic routes. Factors important in the nanoparticle size(s) produced are⁹ the temperature of the reduction step (lower temperature reduces average size), the thiol-to-Au atom ratio (larger ratios reduce average size), and the rate of addition of NaBH₄ (faster addition reduces poly-dispersity). The reaction described here using hexanethiolate ligands produces, according to analytical data presented below, MPCs with a Au₂₂₅ core size using a ligand-to-Au ratio of 2:1, 0 °C reduction reaction temperature, and a fast (~10 s) addition of NaBH₄. The ethanol-insoluble reaction product contained the Au₂₂₅ component. Generally, ethanol-soluble MPCs have smaller cores²⁰ than their ethanol-insoluble counterparts; by collecting the ethanol-insoluble fraction and using a 2:1 thiol:Au reaction—rather than the 3:1 feed favored⁹ in preparation of Au₁₄₀ MPCs, a somewhat larger average core size MPC was produced.

Transmission electron microscopy measurements are shown in Figure 2.1a and b. The histogram in Figure 2.1b (a TEM composite from three synthetic batches) indicates a mean core diameter of 2.0 nm with a standard deviation of 0.4 nm. The 2.0 nm diameter is consistent with that of a “closed shell” truncated octahedral structure (1.96 nm) previously modelled.⁹ Thermogravimetric analysis of the reaction product gave the result in Figure 2.1c, where upon heating from 30 °C to 600 °C, the MPC sample lost 17% of its mass—this represents the organic fraction as previously shown.⁹ Taking a core mass corresponding to Au₂₂₅, the TGA result indicates the presence of 75 hexanethiolate ligands per gold core.

Figure 2.1. (a) TEM image of $\text{Au}_{225}[(\text{S}(\text{CH}_2)_5\text{CH}_3)]_{75}$ in CH_2Cl_2 ; (b) Size-distribution histogram for several TEM images of $\text{Au}_{225}[(\text{S}(\text{CH}_2)_5\text{CH}_3)]_{75}$ in CH_2Cl_2 (118 MPCs in total from three different batches synthesized separately); (c) TGA analysis of organic mass lost for a sample of $\text{Au}_{225}[(\text{S}(\text{CH}_2)_5\text{CH}_3)]_{75}$; (d) UV/Vis absorbance spectrum for $\text{Au}_{225}[(\text{S}(\text{CH}_2)_5\text{CH}_3)]_{75}$.



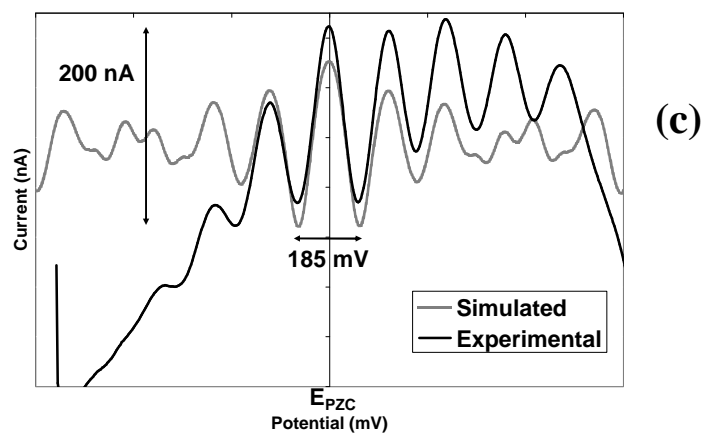
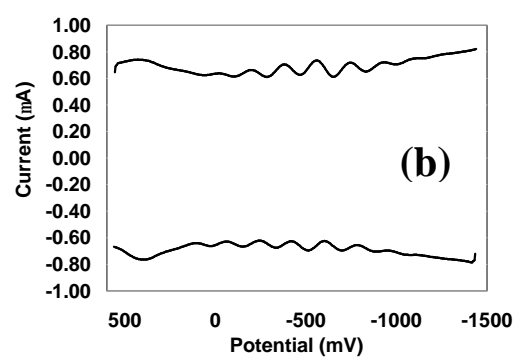
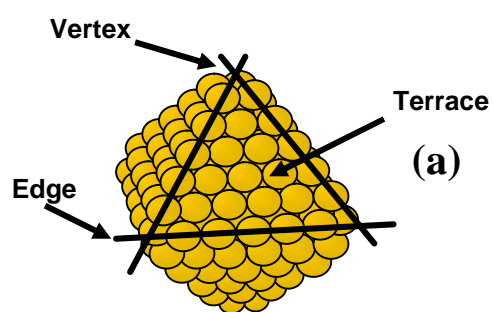
We thereby take the *average* formula for the MPC product as $\text{Au}_{225}[(\text{S}(\text{CH}_2)_5\text{CH}_3)]_{75}$.

While this must be emphasized as an average formula, in light of the evident polydispersity, the analytical ligand count is not far from the modelled⁹ number of 71.

Some comments on the model Au_{225} dimensions are in order at this point. Through extensive theory³⁵⁻³⁷ and experimental evidence from both x-ray diffraction (XRD)^{35,36} and high resolution electron microscopy (HREM),^{35,36} it has been suggested that Au MPC cores prefer truncated octahedral (TO) shapes and closed shell structures (so-called “magic numbers”). Many proposed MPC cores, including Au_{140} and Au_{225} , are truncated octahedrons, referred to as TO+ because the shapes are ($0 < n - m = 4$), where n is the number of atoms between (111) facets and m is the number of atoms between (111) and (100) facets.⁹ Generally, the actual analytical data are insufficient to distinguish the extent of truncation, which leaves a necessary uncertainty in the atom count. Thus, it is possible that a sample of Au_{140} contains some Au_{142} or Au_{144} , etc. The same uncertainty must be noted for Au_{225} , whose truncated octahedral shape is illustrated in Figure 2.2. The Figure 2.2 ideal core model has 85 internal atoms and 140 surface atoms, of which 24 are at the truncated vertexes, 36 are edge atoms, and 80 are terrace atoms.

As mentioned in the introduction, larger MPCs exhibit surface plasmon bands at *ca.* 520 nm, similar to that of bulk Au. The UV/vis absorbance spectrum of the isolated ethanol-insoluble fraction, in a CH_2Cl_2 solution, displays in Figure 2.1d a steep decay of absorbance from low to higher wavelength interrupted only by a weak, broad surface plasmon band at ~520 nm. The presence of the latter feature signals a somewhat larger core diameter than the 1.6 nm diameter of Au_{140} MPCs, where this band was largely extinguished^{9,14} by damping effects.¹² There is a population of larger core size MPCs in the present samples that might contribute to the plasmon band in Figure 2.1d, but evidence

Figure 2.2. (a) Model of Au₂₂₅ core with vertex, terrace, and edge atoms labeled; (b) Osteryoung square wave voltammogram (OSWV) of 0.2 mM Au₂₂₅[(S(CH₂)₅CH₃)]₇₅ in CH₂Cl₂ with 0.1 M tetrabutylammonium perchlorate. OSWV measured with step potential of 4 mV, square wave amplitude of 25 mV, square wave frequency of 15 s⁻¹, quiet time of 2 s, sensitivity of 1 μA/V, and sampling rate of 256 samples per point; (c) Oxidation scan only of OSWV of polydisperse Au₂₂₅[(S(CH₂)₅CH₃)]₇₅; the solid line represents the same experimental data as in part (b) of this figure. The shaded line represents a simulation which includes currents weighted according to proportions of various sizes from TEM histogram (Figure 2.1b), as shown in Ref. 32.



presented below, in which the sample has been chromatographically fractionated, shows that the Au₂₂₅ MPC does display a weak plasmon absorbance similar to that in Figure 2.1d.

Electrochemical Measurements. A small-core Au alkanethiolate-protected MPC that is not small enough to have developed a molecule-like homo-lumo energy gap, can still exhibit a size-dependent electrostatic property owing to its sub-attofarad (aF) cluster double layer capacitance (C_{CLU}). The small MPC capacitance can be attributed to a combination of small core radius and low dielectric of the surrounding hydrocarbon-like monolayer.²⁰ The capacitances, C_{CLU} , of individual MPCs dissolved in an electrolyte solution are sufficiently small that the voltage intervals (ΔV) between sequential single electron changes in their core charges are voltammetrically detectable.²⁰ This phenomenon has been called quantized double layer (QDL) charging,^{18,20,23} and the voltage interval is given by²⁰

$$\Delta V = \frac{e}{C_{CLU}} \quad (1)$$

where e is the electronic charge. Thus, the electronic charging of the MPC core is a strongly size-dependent, or quantized, process, in which macroelectrode differential pulse and cyclic voltammetry of MPC solutions yield a series of observable one-electron current peaks with diffusion-controlled²⁰ characteristics. The electrochemical current peaks are termed quantized double-layer charging (QDL) peaks.^{23,38} The location of these current peaks on the potential axis gives definitive information on the nature of the MPC core charging process, and the minimum in the overall capacitance profile gives^{38b} clues as to the potential at which the MPC has zero electronic charge (E_{PZC}).

The electrochemical principles of QDL are basically the same as those of macroscopically large electrified interfaces coated with alkanethiolate self-assembled monolayers³⁹ in electrolyte solutions, except for small radius of

curvature effects that compress the diffuse double layer.⁴⁰ The MPC capacitances are dominated by dielectric properties of the monolayer shell, and are remarkably well predicted²⁰ by the relation for a concentric sphere capacitor, in which the Au core surface and the monolayer/electrolyte interface, separated by the dielectric of the alkanethiolate monolayer (of thickness d and static dielectric constant ϵ), form the concentric spheres. The relevant relation is

$$C_{\text{CLU}} = 4\pi\epsilon_0\epsilon\left(\frac{r}{d}\right)(r + d) \quad (2)$$

where C_{CLU} is cluster capacitance, ϵ_0 is the permittivity of free space, and r is the radius of the core. A convenient combination of equations (1) and (2) can be used to calculate an apparent core radius (r) from ΔV data, provided ϵ can be estimated.

$$r^2 + (rd) - \left(\frac{ed}{4\pi\epsilon_0\epsilon\Delta V}\right) = 0 \quad (3)$$

Assuming that the hexanethiolate chains are fully extended, the thickness, d , of the hexanethiolate monolayer is 0.8 nm. We have taken $\epsilon = 3.0$ for the static dielectric constant for a hexanethiolate monolayer²¹ on a small Au cluster, which is close to the value (2.6) estimated from data on self-assembled alkanethiolate monolayers,³⁹ where it was assumed that ϵ does not change with chain length. When ΔV has been determined, the only remaining variable in equation (3) is the radius of the core, r , which can then be calculated.

QDL effects are advantageously seen using pulse voltammetry, which has the general virtue of magnifying current-potential features that may be weak in the more common cyclic voltammetry method. Osteryoung square wave voltammetry (OSWV) of the Au₂₂₅ product is shown in Figure 2.2b. The results are typical—as previously evaluated³² by simulations—of an MPC sample that has a dominant size population, but which has

numerous other sizes present that constitute background currents and blur the QDL picture. Figure 2.2c shows that the experimental OSWV correlates well, especially near E_{PZC} , with a simulated OSWV of an equally polydisperse sample of $Au_{225}[(S(CH_2)_5CH_3)]_{75}$. The simulated voltammogram takes into account the various fractions of different sized MPCs in the experimental sample as assessed from the TEM results discussed above (Figure 2.1b). The OSWV oxidation scan of simulated and experimental Au_{225} MPCs correspond well. The evenly-spaced current peaks, with $\Delta V = 183 \pm 5$ mV, are best-defined around *ca.* -0.6V vs. Ag/AgCl which should³² be near the E_{PZC} . Using Equation 3, an estimate of $r = 1.0$ nm is obtained. This result is consistent with the average core dimension obtained from TEM data (*vide supra*), and with a 225 atom core. The QDL results are thus consistent with the average formula $Au_{225}[(S(CH_2)_5CH_3)]_{75}$.

The ratio of the peak currents to overall current can be used to estimate the sample purity. We calculate that the sample in Figure 2.2 is about 20% monodisperse, meaning that 20% of the MPCs are actually Au_{225} core-sized MPCs. The pulse voltammetry gradually becomes less distinct at higher and lower electrode potentials, which is expected from simulations³² for a background current generated by the charging of the mixture of larger MPC sizes present in the poly-disperse sample.³²

High-Performance Liquid Chromatography with Absorbance and Electrochemical Detection. The HPLC experiments used optical absorbance PDA and electrochemical detectors in series. The photodiode array detector detects the optical absorbance of the MPCs in each eluted peak at their concentration C_{conc} . Theoretically, the optical absorbance (Abs) of a solution of uniform spheres that are much smaller than the wavelength of the detecting light is proportional to the volume fraction of nanoparticles, Q ,^{12,41,42} which in turn is related to MPC concentration as $Q \propto C_{conc}r^3$ (where r is core

radius and assuming that the monolayer does not contribute to Q). These two relationships can be combined and simplified to show³³ that the MPC absorbance (Abs) is proportional to the product of MPC concentration and MPC core radius cubed,³³

$$\text{Abs} \propto C_{\text{conc}} r^3 \quad (4)$$

The electrochemical detector is a channel flow cell. The general equation for the current that arises from a one-electron step (determined as described below) in the electrochemistry in the channel-like setup in the electrochemical detector is⁴³

$$i_{\text{lim}} = 1.467 n F C_{\text{conc}} \left(\frac{DA}{b} \right)^{2/3} U_v^{1/3} \quad (5)$$

where n is one, F is Faraday's constant, A is the area of the working electrode, C_{conc} and D are the concentration and diffusion coefficient (cm^2/s), respectively, of the MPCs, b is the height of the channel, and U_v is the volume flow rate (cm^3/s). D is inversely proportional to MPC hydrodynamic radius ($r + d$) through the Stokes inversely proportional to MPC hydrodynamic radius ($r + d$) through the Stokes equation.⁴⁴

Both the optical and electrochemical signals are related to the size of the cluster, but neither alone can be used to determine cluster size because each also depends on the unknown concentration, C_{conc} , in the eluted band. However, if their ratio is taken,³³ MPC size determination can be achieved since C_{conc} cancels, giving

$$\frac{A}{i_{\text{lim}}} a \frac{C_{\text{conc}} r^3}{C_{\text{conc}} D^{2/3}} = r^3 (r + d)^{2/3} \approx r^{11/3} \quad (6)$$

The absorbance-to-current ratio can be used to determine r of an unknown MPC, provided another MPC of known r is also eluted in the chromatogram, and similarly measured.

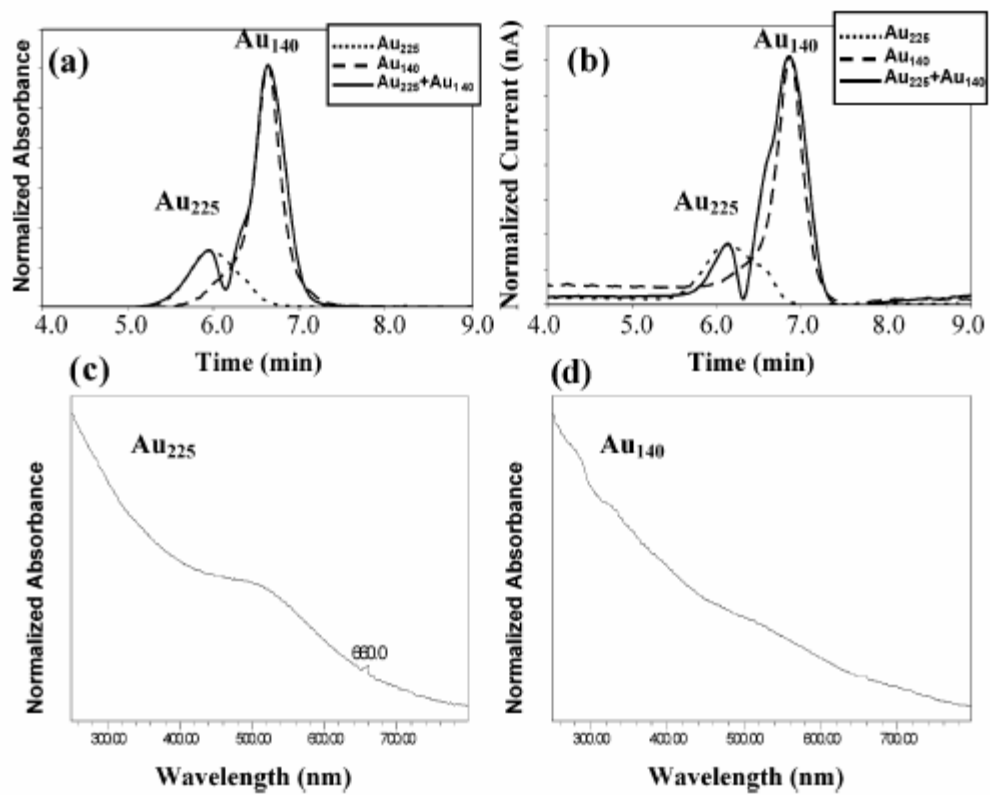
The ratiometric experiment was performed with a deliberate mixture of $\text{Au}_{225}[(\text{S}(\text{CH}_2)_5\text{CH}_3)]_{75}$ and $\text{Au}_{140}[(\text{S}(\text{CH}_2)_5\text{CH}_3)]_{53}$ MPCs, and was also done on two

different sets of serial columns as described in the Experimental Section. All other experimental conditions were held constant for both experiments. Figure 2.3a and b, solid line, show the chromatography of the mixture, using the XTerra columns, giving both optical and electrochemical outputs. The chromatography of the individual Au₁₄₀ and Au₂₂₅ MPC samples is shown by the dashed and dotted lines in Figure 2.3a and 3b. There is a slight difference (~0.2 s) in the retention times in Figure 2.3a and b due to the flow delay time between the two detectors. The ratios of the Abs and current responses differ, as expected from Equation 6, since the MPC core radii differ.

Each chromatogram consists of two peaks. From the corresponding absorbance spectra, Figure 2.3c and d, it is evident that the larger Au₂₂₅ MPC sample elutes before the Au₁₄₀ MPC sample, indicating a size-exclusion-like separation mechanism in these small-pore-diameter columns. While the columns are selective enough to separate the Au₁₄₀ and Au₂₂₅ MPCs, they are not sufficiently selective to separate any slightly differently sized MPCs within the Au₂₂₅ MPC sample. Thus, although the Au₂₂₅ MPC sample is poly-disperse, only one peak appears in each chromatogram for the Au₂₂₅ sample. (It is also possible that some larger MPCs are irreversibly retained by the column.)

The double layer charging of the electrochemically detected MPCs is detected without interference from double layer charging of the working electrode itself because the working electrode is at a fixed potential. That potential determines the potential to which the MPC cores are charged, as a kind of pseudoredox process.^{23,38} It is desirable to define i_{lim} as a single electron current ($n = 1$ in equation 5), which makes it necessary to map out complete hydrodynamic voltammograms of the eluted MPCs, to find the current corresponding to a one electron charge change, as for example, Au₂₂₅ to Au₂₂₅¹⁺. Thus, in Figure 2.3, repeated chromatograms were performed using serially adjusted changes in the

Figure 2.3. HPLC chromatograms for a solution of a mixture of $\text{Au}_{225}[(\text{S}(\text{CH}_2)_5\text{CH}_3)]_{75}$ and $\text{Au}_{140}[(\text{S}(\text{CH}_2)_5\text{CH}_3)]_{57}$ (solid line), $\text{Au}_{225}[(\text{S}(\text{CH}_2)_5\text{CH}_3)]_{75}$ alone (dotted line), and $\text{Au}_{140}[(\text{S}(\text{CH}_2)_5\text{CH}_3)]_{57}$ alone (dashed line) from (a) the PDA absorbance detector and (b) the electrochemical detector taken at a potential of 350 mV. The corresponding absorbance spectra are shown for the (c) $\text{Au}_{225}[(\text{S}(\text{CH}_2)_5\text{CH}_3)]_{75}$ and (d) $\text{Au}_{140}[(\text{S}(\text{CH}_2)_5\text{CH}_3)]_{57}$ peaks obtained from the absorbance chromatogram of the mixture.



electrochemical detector's working electrode potential, from +50 to +850 mV, in 50 mV increments. Figure 2.4 shows the results for the two MPCs. The current peak heights change in a step-like pattern corresponding to single electron i_{lim} increments in the MPC core charge.

Table 2.1 gives the results for Abs and i_{lim} for the two MPCs, and on the two sets of serial columns. When Equation 6 is applied to these results, the relative radii can be calculated and are reported in Table 2.1. The core radius (0.8 nm)⁹ of Au₁₄₀ MPCs is taken as the calibrant, giving the indicated results for the actual radius of the Au₂₂₅ MPCs. The results are very consistent with those from TEM and ΔV evaluations above. The ΔV values evident in the hydrodynamic voltammetry of Figure 2.4 are larger than those in Figure 2.2. This is attributed to the large IR drop associated with the channel-like flow cell electrochemical detector, which affects potential values, but not limiting currents.

2.4 Conclusions

Using various analytical techniques and calculations that take advantage of the one-electron charging properties of monolayer protected clusters, the core size of a newly synthesized MPC sample was identified to be 225 Au atoms with a radius of 1.0 nm. Through multiple analytical techniques the formula for this new MPC was determined to be Au₂₂₅[(S(CH₂)₅CH₃)]₇₅. It is interesting to see that although Au₂₂₅ MPCs are larger than most previously reported, they still exhibit double layer charging peaks consistent with a simple concentric sphere capacitor model, which pushes the boundary of nanoparticle and bulk metal further into larger sized clusters. The HPLC separation with optical and electrochemical ratiometric detection proved to be an extremely useful method of confirming the Au₂₂₅ MPC core size. In the future, this technique should continue

Figure 2.4. Current vs. potential curves for the single electron charging event of the 0 to +1 state of the eluted bands of (a) $\text{Au}_{225}[(\text{S}(\text{CH}_2)_5\text{CH}_3)]_{75}$ and (b) $\text{Au}_{140}[(\text{S}(\text{CH}_2)_5\text{CH}_3)]_{57}$ with limiting current shown (i_{lim}).

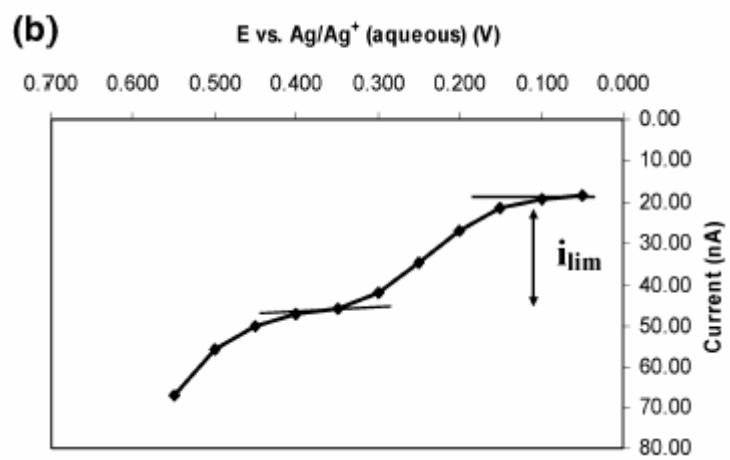
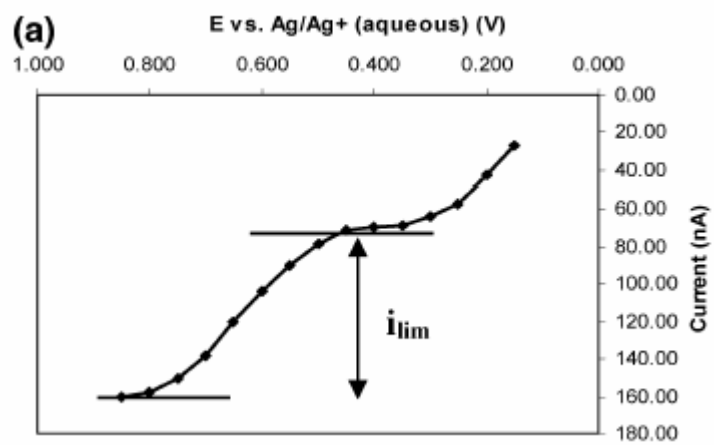


Table 2.1. Estimation of Core Size of Au₂₂₅[(S(CH₂)₅CH₃)]₇₅ MPCs Using HPLC and Ratio of Optical Absorbance Detector Signal and One-Electron Charging Currents of MPCs in Two Separate Experiments

retention time (min)	absorbance peak heigh (at $\lambda = 400$ nm)	i_{lim} (nA)	Abs / i_{lim}	rel core radii $[Abs / i_{\text{lim}}]^{3/11}$	est core radius (r) of MPCs (nm)
Experiment 1 (BioBasic Columns)					
5.9	0.37	4.72	0.078	0.50	1.1
7.4	0.70	28.4	0.025	0.36	0.8
Experiment 2 (XTerra Columns)					
5.8	0.71	25.1	0.028	0.31	1.0
6.5	1.94	115	0.017	0.26	0.8

to prove helpful, for example in studying how or whether core sizes change during various nanoparticle reactions, such as ligand-exchanges.

2.5 Acknowledgments

This research was supported by grants from the National Science Foundation and Office of Naval Research.

2.6 References

- (1) Templeton, A.C.; Wuelfing, W.P.; Murray, R.W. *Acc. Chem. Res.* **2000**, *33*, 27 – 36.
- (2) Neiman, B.; Grushka, E.; Lev, O. *Anal. Chem.* **2001**, *73*, 5220-5227.
- (3) Park, J. H.; Lim, Y. T.; Park, O. O.; Kim, Y. C. *Macromol. Rapid Commun.* **2003**, *24*, 331-334.
- (4) Reynolds, R. A.; Mirkin, C. A.; Letsinger, R. L. *J. Am. Chem. Soc.* **2000**, *122*, 3795-3796.
- (5) Taton, T. A.; Mucic, R. C.; Mirkin, C. A.; Letsinger, R. L. *J. Am. Chem. Soc.* **2000**, *122*, 6305-6306.
- (6) Guczi, L.; Horváth, D.; Pászti, Z.; Tóth, L.; Horváth, Z. E.; Karacs, A.; Pető, G. *J. Phys. Chem. B* **2000**, *104*, 3183-3193.
- (7) Franceschetti, A.; Pennycook, S. J.; Pantelides, S. T. *Chem. Phys. Lett.* **2003**, *374*, 471-475.
- (8) Brust, M.; Walker, M.; Bethell, D.; Schiffrin, D.J.; Whyman, R. J. *Chem. Soc., Chem. Commun.* **1994**, 801 – 802.
- (9) Hostetler, M.J.; Wingate, J.E.; Zhong, C.-J.; Harris, J.E.; Vachet, R.W.; Clark, M.R.; Londono, J.D.; Green, S.J.; Stokes, J.J.; Wignall, G.D.; Glish, G.L.; Porter, M.D.; Evans, N.D.; Murray, R.W. *Langmuir* **1998**, *14*, 17 – 30.
- (10) Optical Properties of Metal Clusters; Kreibig, U.; Vollmer, M., Eds. Springer-Verlag: New York, 1995.
- (11) Underwood, S.; Mulvaney, P. *Langmuir* **1998**, *10*, 3427 – 3430.
- (12) Mulvaney, P. *Langmuir* **1996**, *12*, 788 – 800.
- (13) Kreibig, u.; Fauth, K.; Quintern, M.; Schönauer, D. *Z. Phys. D* **1989**, *12*, 505.
- (14) Alvarez, M. M.; Khoury, J. T.; Schaaff, T. G.; Shaffigullin, M. N.; Vezmar, I.; Whetten, R. L. *J. Phys. Chem. B* **1997**, *101*, 3706 – 3712.
- (15) Schaaff, T.G.; Shafigullin, M. N.; Khoury, J. T.; Vezmar, I.; Whetten, R. L.; Cullen, W. G.; First, P. N. *J. Phys. Chem. B* **1997**, *101*, 7885 – 7891.
- (16) Landes, C. F.; Braun, M.; El-Sayed, M. A. *J. Phys. Chem. B* **2001**, *105*, 10554 – 10558.

- (17) Huang, T.; Murray, R. W. *J. Phys. Chem. B* **2001**, *105*, 12498 – 12502.
- (18) Chen, S.; Ingram, R. S.; Hostetler, M. J.; Pietron, J. J.; Murray, R.W.; Schaaf, T. G.; Khoury, J. T.; Alvarez, M. M.; Whetten, R. L. *Science* **1998**, *280*, 2098 – 2101.
- (19) Ingram, R. S.; Hostetler, M. J.; Murray, R. W.; Schaff, T. G.; Khoury, J. T.; Whetten, R. L.; Bigioni, T. P.; Guthrie, D. K.; First, P. N. *J. Am. Chem. Soc.* **1997**, *119*, 9279 – 9280.
- (20) Hicks, J. F.; Templeton, A. C.; Chen, S.; Sheran, K. M.; Jasti, R.; Murray, R. W.; Debord, J.; Schaaff, T. G.; Whetten, R. L.;. *Anal. Chem.* **1999**, *71*, 3703-3711.
- (21) Hicks, J. F.; Miles, D. T.; Murray, R. W.; *J. Am. Chem. Soc.* **2002**, *124*, 13322 – 13328.
- (22) Jimenez, V.L.; Leopold, M.C.; Mazzitelli, C.; Jorgenson, J. W.; Murray, R.W. *Anal. Chem.* **2003**, *75*, 199 – 206.
- (23) Chen, S.; Murray, R. W.; Feldberg, S. W. *J. Phys. Chem. B* 1998, *102*, 9898 – 9907.
- (24) Lee, D.; Donkers, R. L.; Wang, G.; Harper, A. S.; Murray, R. W. *J. Am. Chem. Soc.* **2004**, *126*, 6193 – 6199.
- (25) Song, Y.; Heien, M. L; Jimenez, V. L.; Wightman, R. M.; Murray, R. W. *Anal. Chem.* **2004**, *76*, 4911 – 4919.
- (26) Jimenez, V. L.; Georganopoulou, D. G.; White, R. J.; Harper, A. S.; Mills, A. J.; Lee, D.; Murray, R. W. *Langmuir* **2004**, *20*, 6864 – 6870.
- (27) Brennan, J. L.; Branham, M. R.; Hicks, J. F.; Osisek, A. J.; Donkers, R. L.; Georganopoulou, D. G.; Murray, R. W. *Anal. Chem.* **2004**, *76*, 5611 – 5619.
- (28) Quinn, B. M.; Liljeroth, P.; Ruiz, V.; Laaksonen, T.; Kontturi, K. *J. Am. Chem. Soc.* **2003**, *125*, 6644 – 6645.
- (29) Yang, Y.; Pradhan, S.; Chen, S. *J. Am. Chem. Soc.* **2004**, *126*, 76 – 77.
- (30) Kim, Y.-G.; Garcia-Martinez, J. C.; Crooks, R. M. *Langmuir* **2005**, *21*, 5485 – 5491.
- (31) (a) Chaki, N. K.; Singh, P.; Dharmadhikari, C.V.; Vijayamohan, K. *Langmuir* **2004**, *20*, 10208 – 10217. (b) Chaki, N. K.; Kakade, B.; Sharma, J.;Mahima, S.; Vijayamohan, K. P.; Haram, S. K. *J. Appl. Phys.* **2004**, *96*, 5032 – 5036.
- (32) Miles, D. T.; Leopold, M. C.; Hicks, J. F.; Murray, R. W. *J. Electroanal. Chem.* **2003**, *554*, 87 – 97.

- (33) Song, Y.; Jimenez, V.; McKinney, C.; Donkers, R.; Murray, R. W. *Anal. Chem.* **2003**, *75*, 5088 – 5096.
- (34) Handbook of Preparative Inorganic Chemistry; Brauer, G., Ed.; Academic Press: New York, 1965; p 1054.
- (35) Cleveland, C. L.; Landman, U.; Shafigullin, M. N.; Stevens, P. W.; Whetten, R. L. *Z. Phys. D* **1997**, *40*, 503 – 508.
- (36) Whetten, R. L.; Khoury, J. T.; Alvarez, M. M.; Murthy, S.; Vezmar, I.; Wang, Z. L.; Stephens, P. W.; Cleveland, C. L.; Luedtke, W. D.; Landman, U. *Adv. Mat.* **1996**, *8*, 428-433.
- (37) Häberlen, O. D.; Chung, Sai-Cheong; Stener, M.; Rösch, N. *J. Chem. Phys.* **1997**, *106*, 5190 – 5201.
- (38) a) Chen, S.; Murray, R. W. *Langmuir* **1999**, *3*, 682 – 689. b) Chen, S.; Murray, R. W. *J. Phys. Chem. B*, **1999**, *103*, 9996-10000.
- (39) Porter, M. D.; Bright, T. B.; Allara, D. L.; Chidsey, C. E. D. *J. Am. Chem. Soc.* **1987**, *109*, 3559 – 3568.
- (40) Guo, R.; Georganopoulou, D.; Feldberg, S. W.; Donkers, R.; Murray, R. W.; *Anal. Chem.* **2005**, *77*, 2662 – 2669.
- (41) Mie, G. *Ann. Phys.* **1908**, *25*, 377 – 445.
- (42) Doremus, R.H. *Langmuir* **2002**, *18*, 2436 – 2437.
- (43) Bard, A.; Faulkner, L. R. *Electrochemical Methods, Fundamentals and Applications*, 2nd Ed.; Chapter 11, p. 448 (Table 11.6.1).
- (44) Wuelfing, W. P.; Templeton, A. C.; Hicks, J.; Murray, R. W. *Anal. Chem.* **1999**, *71*, 4069 – 4070.

CHAPTER III

FULLY FERROCENATED HEXANETHIOLATE MONOLAYER-PROTECTED GOLD CLUSTERS

3.1 Introduction

There has been substantial recent interest¹⁻³ in the optical, electronic, and chemical properties of metal nanoparticles, including the dimensional sensitivity of their properties. Stable protecting monolayer coatings offer the advantages of facilitating purification, permitting the investigation of properties according to nanoparticle size, and enabling analytical characterization and chemical modification of the monolayer, so that an initial chemically simple monolayer can be transformed into an elaborately functionalized one. We have reported on the properties of stable gold nanoparticles coated with monolayers of thiolate ligands, dubbed monolayer protected clusters (MPCs),⁴ and having various (closed shell) average atom counts.⁵ Additionally we have investigated how the MPC monolayer can be chemically changed by functional group coupling reactions⁶ or by exchange of one ligand for another⁷ to create MPCs with mixed monolayer compositions. Au MPCs have a core size-dependent set of properties and a protecting monolayer-dependent set of properties. Further, via dielectric⁸ or electron-inductive characteristics⁹ of the monolayer, core properties can become monolayer-dependent.

Presented here is an investigation of monolayer-protected Au nanoparticles which, for the first time, have monolayers composed exclusively of **w**-ferrocenyl hexanethiolate ligands, and the cores have, variously, average atom counts of 75, 140, 225, or 314 Au atoms. These novel MPCs have monolayers that exhibit strong steric effects, and this paper presents a unique analysis of these effects as a function of core size.

These new ferrocenated Au MPCs undergo electrochemical reactions both by the redox chemistry of the monolayer's ferrocene units and by the charging of the Au cores of the nanoparticles. The result is a capacity to store or release many equivalents of electrochemical charge over a small potential range. Having a full monolayer of the redox moiety on the MPC core in particular enhances the number of charges stored per nanoparticle. Because the MPCs are nanoscopic objects, they exhibit large volume charge-densities (i.e., volume-based energy densities). The charge is further stored in a spatially organized manner, in effect being on two spherical surfaces—one being the sphere of the Au-thiolate bond interface (the core charging), and the other the sphere of ferrocene termini of the thiolate ligands (the redox charging). This study demonstrates how a fully electroactive protecting monolayer can combine with the intrinsic, size-dependent electrochemistry properties of the Au core to create nanoparticles that can transfer as many as 60 electrons over a small range of electrochemical potential. This charge storage ability leads to a volume charge density of *ca.* $7 \times 10^9 \text{ C/m}^3$ which is significantly larger than the previous largest volume charge density (*ca.* $5 \times 10^9 \text{ C/m}^3$) among earlier reported¹⁰ electroactive mixed monolayer MPCs.

A further influence on redox charge storage capacity is the steric requirements of the redox moiety on the spherical outer surface of the MPC. Redox functionalities (ferrocenes and other moieties) have been previously introduced to Au MPC monolayers¹⁰⁻¹⁸ as a

second step, either by ligand exchange or by coupling reactions with functionalized monolayers. All previous studies have lead to mixed monolayer MPCs with less than 100% surface loading with the redox moiety. As is presented in this paper, synthesizing MPCs using only redox-labeled thiols for the protecting monolayer raises the potential issue of steric interactions during the assembly of the fully functionalized redox-active monolayer. There have been reports that show that bulky ligands can affect the core size,^{19,20} size dispersity,¹⁹ core shape,²⁰ stability,^{21,22} and chemical reactivity^{18,21,23,24} of nanoparticles. While the steric hindrances of bulky ligands have been shown before, this study is unique in that it investigates the steric effects of a fully functionalized monolayer on the MPCs as a function of core size. Qualitatively, the severity of steric interactions between redox sites should decrease for smaller and smaller nanoparticles, owing to their steeper surface curvature. There are no previous data demonstrating this, so the investigation included a range of small average Au core sizes.

The preponderance of the charge storage capacity of a fully redox labeled MPC lies in the redox monolayer charging rather than in core charging. The redox capacity, in charge/volume terms, given the surface area/volume properties of a sphere, is expected to increase inversely with the overall MPC radius. The double layer charge capacity—for which the relevant spherical surface area is the core-thiolate interface—is similarly expected to increase inversely with the overall MPC radius (at least down to where molecule-like properties emerge). One is therefore driven to examine small MPCs, leading to choices of Au MPCs with 75, 140, 225, or 314 average atom count cores.

A third factor possibly influential on redox charge storage capacity is the degree to which a diversity of electrochemical potentials is generated by electrostatic (or other) interactions between redox sites. These interactions are well-known in electrochemistry of

chemically modified electrodes²⁵ and self-assembled monolayers.^{26,27} While the charge capacity may be un-diminished, its availability becomes spread over a wider span of electrochemical potentials.

These fully ferrocenated Au MPCs markedly enlarge the growing field of dissolved nanoscopic materials that can accept or release multiple equivalents of charge of which several noteworthy examples are discussed here. The electrochemical oxidation²⁸ of a dissolved redox polymer molecule like poly-vinylferrocene can release as many as 75 electrons per molecule, for example. The poly-vinylferrocene oxidation, and that of the 64 peripheral ferrocenyl moieties²⁹ bound to a fifth generation poly-(propylenamine)-based ferrocenyl dendrimer, act as independent redox centers so that the reaction has the voltammetric characteristics of multiple single electron transfers. Nanocomposites of metal-oxide nanoparticles³⁰ incorporated into conducting polymers like polypyrrole can be prepared and electrochemically charged and discharged. Conducting polymers³¹ like polyaniline can be doped with polyoxometalate anions (e.g., phosphomolybdate) and can intercalate cations while taking advantage of the reversible multielectron reduction processes of the anion to electrochemically charge and discharge the polyaniline. Although an electrostatic rather than chemical phenomenon, the electrical double layers of metal colloids³² require multiple electrons for charging. C₆₀ fullerenes³³ undergo six successive reductions owing to the triple degeneracy of their LUMO. These examples expose the diversity of known multi-electron nanoscopic materials.

Comment is needed on the core charging of Au MPCs (with electroinactive protecting thiolate monolayers), whose electrochemistry^{8,14,34-47} has been shown over the past several years to exhibit interesting, size-dependent properties. Very small Au nanoparticles with core radii below *ca.* 0.8 nm display molecule-like behavior in their voltammetry by the

spacing seen between the potentials of the first one-electron reduction and the first one-electron oxidation peaks. The spacing reflects a HOMO-LUMO energy gap between molecular orbitals.^{36,40} Au MPCs with larger core radii (between *ca.* 0.8 nm and *ca.* 2.0 nm) and with a low dielectric monolayer shell, so that they have a very small double layer capacitance (C_{CLU}), display single-electron double layer charging voltammetry in a phenomenon called “quantized double-layer (QDL) charging”.⁴ These MPCs have a more-or-less continuous density of electronic states. For example, charging of the double layer of an MPC having a capacitance of 1 aF occurs in one-electron current peaks evenly spaced by an easily detected 160 mV on the potential scale (according to the expression $\Delta V = e/C_{\text{CLU}}$ where e is the electron charge). Core double layer charging of course also occurs for large nanoparticles, but when $\Delta V < k_{\text{B}}T$ (thermal spreading, *ca.* 26 mV at 298 K), it is seen as an unresolved current continuum.³² While these core-based electrochemical processes are expected to continue to occur when the monolayer is functionalized with electroactive or other groupings, in previous reports where larger Au cores were protected by mixed monolayers containing functionalized ligands, the size-dependent core charging electrochemistry could not be discerned. Here, for the first time, we show that the core charging features are indeed retained in the MPC electrochemistry.

3.2 Experimental

Chemicals. Hexanethiol (HSC6, >99%), *tetra*-octylammonium bromide (Oct₄NBr, >98%), sodium borohydride (NaBH₄, >98%), and *tetra*-butylammonium perchlorate (Bu₄NClO₄, >99%) from Aldrich, and toluene (reagent grade), acetonitrile (Optima), methylene chloride (HPLC grade), and ethanol (HPLC grade) from Fisher were used as received. H₂AuCl₄·xH₂O (from 99.999% pure gold) was synthesized using a literature

procedure⁴⁸ and stored in a freezer at -20 °C. Water was purified using a Barnstead NANOpure system (18 MO).

Ferrocene hexanethiol (HSC6Fc) was synthesized as follows. Alkyl bromide substituted ferrocene, synthesized by a published method,⁴⁹ was converted to the corresponding thiol by refluxing it (1.106 g, 3.17 mmol) with thiourea (0.600 g, 7.88 mmol) in ethanol (50 mL) overnight. Aqueous sodium hydroxide was added to the reaction mixture and refluxed for a further 3h, followed by acidification with HCl to pH ~ 2. The reaction mixture was diluted with water and extracted with CH₂Cl₂, and the combined organic phase washed copiously with water. The material obtained after rotary evaporation of the CH₂Cl₂ was chromatographed on silica gel with ethyl acetate/hexanes to give spectroscopically satisfactory ferrocene hexanethiol.

MPC Synthesis. Four MPC sizes were synthesized. Three of the syntheses were completed as in previous work,^{5,42} but with ferrocene hexanethiol as the sole ligand. The only difference between the three syntheses is the feed mole ratio of thiol-to-gold. Briefly, 3.19 g HAuCl₄·xH₂O in 100 mL deionized water was vigorously mixed with a solution of 5.20 g Oct₄NBr in 200 mL toluene. The aqueous phase changed from yellow to clear and the toluene phase from clear to orange-brown. Ferrocene hexanethiol was then added to the isolated organic phase—in 3:1, 2:1, and 1:1 ligand-to-gold mole ratios, and the colorless reaction mixture was stirred for 20 minutes at room temperature. Cooling it to 0 °C, and rapidly stirring, 3.8 g of NaBH₄ in 10 mL water was quickly added, producing a dark solution that was further stirred for 1 hour at 0 °C. The organic phase was collected and the solvent removed on a rotary evaporator at room temperature. The black solid was suspended in 400 mL of acetonitrile for 6 hours. Using a glass frit, the solid product was collected and cleaned with excess acetonitrile.

The fourth synthesis performed was a ligand exchange reaction between ferrocene hexanethiol and $\text{Au}_{55}(\text{PPh}_3)_{12}\text{Cl}_6$ MPCs. The $\text{Au}_{55}(\text{PPh}_3)_{12}\text{Cl}_6$ synthesis and ligand exchange reaction of other, non-electroactive thiols has been described elsewhere.⁴⁰

Transmission Electron Microscopy (TEM). TEM was performed on a Hitachi HF-2000, operated at 200 kV. Samples for TEM were prepared by dispersing the MPCs in CH_2Cl_2 and drop casting onto grids with ultrathin carbon films supported by holey carbon (Ted Pella). The MPC sizes were measured using ImageJ.

Electrochemistry. Voltammetry was done with a Model 100B Bioanalytical Systems, Inc. (BAS) Electrochemical Analyzer, in 0.1 M Bu_4NClO_4 in CH_2Cl_2 solutions that were degassed and blanketed with high-purity Ar during the experiment. The working electrode was a 0.4 mm Pt disk, the counter electrode a Pt wire, and the reference electrode a Ag/AgCl (aqueous) electrode. The working electrode was polished with a 0.05 μm Al_2O_3 slurry and cleaned electrochemically by potential cycling in 0.1 M H_2SO_4 solution. Cyclic voltammetry was done at 100 mV/s, and Osteryoung square wave voltammetry with potential steps of 4 mV, square wave amplitude of 25 mV, square wave frequency of 15 s^{-1} , and quiet time of 2 s.

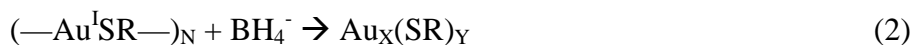
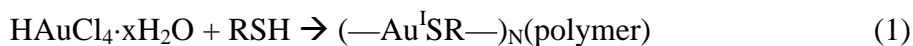
Bulk electrolysis of MPC solutions was performed on the same BAS instrument in 0.050 M Bu_4NClO_4 in CH_2Cl_2 solution degassed with high-purity Ar. The working electrode was a Pt mesh electrode, the counter electrode a Pt wire (in a separate cell compartment), and the reference electrode a Ag/AgCl (aqueous) electrode.

Other Measurements. ^1H NMR of Au MPCs in CD_2Cl_2 was obtained using a Bruker 400 MHz Avance spectrometer, with a 5 s relaxation delay time. UV-vis spectra of freshly prepared MPC solutions in CH_2Cl_2 were taken on a Shimadzu UV-Vis (Model UV-1601) spectrometer. Thermogravimetric analysis (TGA) was performed with a Seiko RTG 220

robotic TGA. Samples of 5 mg were placed in an Al crucible within a Pt crucible. The samples were heated from 30 °C to 600 °C at 15 °C per minute.

3.3 Results and Discussion

Synthesis of Ferrocenated MPCs. In the original Brust et al⁵⁰ report, reaction of a 1:1 mole ratio of dodecanethiol and AuCl₄⁻ followed by reduction with BH₄⁻, led to dodecanethiolate-protected Au MPCs with core diameters of 1 – 3 nm. The general reaction can be stated as



There have been numerous applications and modifications of this basic procedure, one virtue of which is that it gives synthetic access to very small MPC core sizes. Ligand exchange procedures¹⁶ have also been frequently employed to create MPCs with mixed monolayers of alkanethiolate and other thiolate ligands; mixed reaction feeds also accomplish this. There have been relatively fewer reports⁵¹⁻⁵⁴ on direct synthesis of MPCs using solely functionalized thiols in the reaction feed, to produce fully functionalized monolayers, and even fewer involving electroactive thiols.⁵⁵

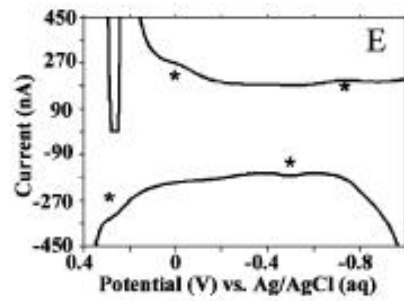
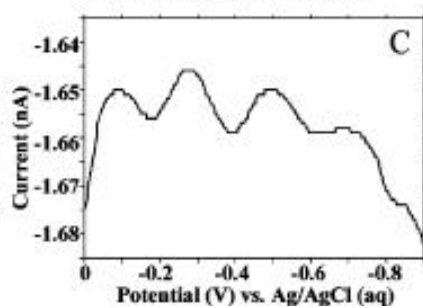
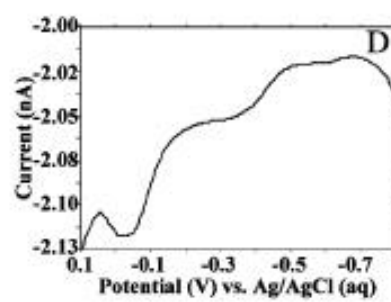
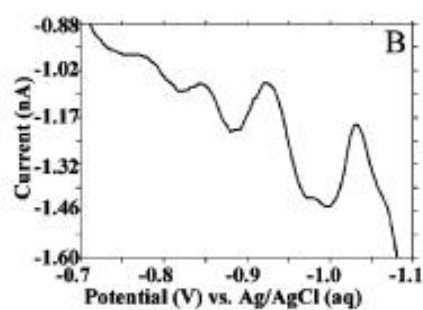
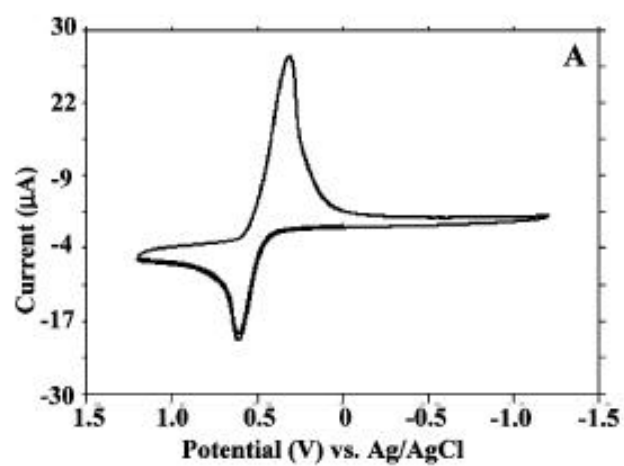
To prepare MPCs with fully ferrocene-functionalized ferrocene monolayers, we employed a modified Brust procedure in which the usual alkanethiol was replaced by ferrocene hexanethiol, in either 3:1, 2:1, or 1:1 mole ratios to Au. In previous work^{5,35,42} with hexanethiol, these proportions produced nanoparticles in which Au MPC core sizes Au₁₄₀, Au₂₂₅, and Au₃₁₄ were present. Evidence is given below that these average core sizes are retained in the new fully ferrocenated MPCs, but that the average number of ligands in the protecting monolayers is diminished by steric constraints.

A fourth synthesis of fully ferrocenated MPCs was based on reaction of the ferrocene hexanethiol with an already synthesized Au₅₅ cluster that was protected⁵⁶ by a triphenylphosphine/chloride monolayer. We have shown⁴⁰ that such a reaction, using hexanethiol, is accompanied by a core size change to an MPC with an average atom count of Au₇₅. The same result was obtained when using the ferrocene hexanethiol. Completeness of the ligand replacement was determined from the ¹H NMR spectrum of the MPC product, in which triphenylphosphine resonances were found to be absent.

Determination of Core Sizes of Ferrocenated MPCs. The cyclic voltammograms of dilute solutions of all four samples of ferrocenated Au MPCs exhibit a well-defined anodic peak and a cathodic peak that is larger, showing that some oxidized product tends to accumulate on the working electrode. The voltammetry of Au₇₅(SC6Fc)₃₇ shown in Figure 3.1A is a typical example. This voltammetric result is consistent with the previously reported voltammetry of a dilute poly-vinylferrocene solution by Flanagan et al.¹⁰ and Merz et al.,⁵⁷ where the oxidized species also accumulated on the electrode. The ferrocene voltammetry in Figure 3.1A was not investigated in detail, but it is notable that the wave is not broadened or split as would be the case with strong interactions between the redox sites. Such splitting is seen in self-assembled monolayer ferrocene voltammetry²⁷ if the monolayer is not severely diluted with alkanethiolate sites.

Au MPCs with average core counts of Au₁₄₀ and of Au₂₂₅ and protected by hexanethiolate monolayers exhibit^{8,34,37,58} size-dependent electrostatic properties owing to their attofarad (aF) cluster double layer capacitances (C_{CLU}). The small MPC capacitance arises from the combination of a small core radius and the low dielectric constant of the surrounding hexanethiolate monolayer.⁸ When dissolved in electrolyte solution, these MPCs display nearly evenly spaced (by $\Delta V = e/C_{CLU}$, where e is the charge of an electron)

Figure 3.1. (A) Cyclic voltammogram of 0.2 mM $\text{Au}_{75}(\text{SC6Fc})_{37}$ in 0.1 M $\text{Bu}_4\text{NClO}_4/\text{CH}_2\text{Cl}_2$ under Ar atmosphere, at 284 K, potential scan rate 500 mV/s, sample interval of 1 mV; (B) Osteryoung square wave voltammogram (OSWV) of $\text{Au}_{314}(\text{SC6Fc})_{58}$; (C) OSWV of $\text{Au}_{225}(\text{SC6Fc})_{43}$; (D) OSWV of $\text{Au}_{140}(\text{SC6Fc})_{39}$; (E) OSWV of $\text{Au}_{75}(\text{SC6Fc})_{37}$ (asterisks indicate first one-electron oxidation and reduction peaks of gold core). For all four MPC core sizes, OSWV was performed on 0.2 mM MPC in 0.1 M $\text{Bu}_4\text{NClO}_4/\text{CH}_2\text{Cl}_2$ with step potential of 4 mV, square wave amplitude of 25 mV, and square wave frequency of 15 s^{-1} .



one electron charging peaks which have been termed quantized double layer (QDL) charging.^{37,58,59} Hexanethiolate-protected Au₁₄₀ MPCs have core diameters of 1.6 nm and $\Delta V = 265 \pm 14$ mV,³⁵ while similarly protected Au₂₂₅ MPCs (core diameter 2.0 nm) exhibit peak spacings of 183 ± 5 mV⁴². Smaller, molecule-like Au MPCs, such as Au₁₁,^{60,61} Au₃₈,^{38,39} and Au₇₅,⁴⁰ display a HOMO-LUMO energy gap in the electrochemistry⁵⁸ by a larger spacing between the first one-electron oxidation and the first one-electron reduction. This spacing is 0.74 V for Au₇₅(hexanethiolate)₄₀.

Thus, for Au₇₅, Au₁₄₀, and Au₂₂₅ cores, the spacing of core charging voltammetric peak currents is diagnostic for hexanethiolate-protected MPC core sizes. Since the hexyl segment offers a similar dielectric shell for the core in the ferrocenated MPCs, a similar spacing is expected for charging of Au cores of the same size. Quantized double layer charging peaks cannot be discerned on the compressed current scale of Figure 3.1A, against the much larger currents for the multiple ferrocenes that are present, but on an expanded scale and at potentials negative of the ferrocene peak, square wave voltammetry reveals charging peaks as shown in Figure 3.1B-E. Voltammetry of the ferrocenated MPCs made by the reaction of ferrocene hexanethiol with the Au₅₅ nanoparticle, and by the 3:1, 2:1, and 1:1 mole ratio syntheses, are shown in Panels E, D, C, and B, respectively. The charging peaks are reasonably evenly spaced, with different ΔV values. The average ΔV is compared to previous results in Table 3.1; the agreement is rather good for the Au₇₅, Au₁₄₀, and Au₂₂₅ cores. QDL for MPCs produced in a 1:1 mole ratio synthesis had not been previously reported. The smaller ΔV in Figure 3.1B suggests a larger core; we preliminarily assign this to a Au₃₁₄ core, the next truncated octahedron closed shell core size above 225 Au atoms.

Table 3.1. Voltammetric Quantized Double Layer Charging Results for Ferrocene-hexanethiolate Protected Au Clusters (Figure 3.1) and Literature Values for

Hexanethiolate Protected Au Clusters

Avg. Core size	Au _x (SC6Fc) _y MPCs Expt. ΔV, mV	Au _x (SC6) _y MPCs Lit. ΔV, mV	Ref.
Au ₇₅	740 ± 10	740 ± 10	40
Au ₁₄₀	256 ± 22	265 ± 14	35
Au ₂₂₅	184 ± 2	183 ± 5	42
Au ₃₁₄	100 ± 20	n/a	not previously reported

The square wave voltammetry peaks in Figure 3.1 are small, and lie atop a substantial background current which presumably reflects unresolved charging peaks of a mixture of other MPC core sizes. The specific core atom counts assigned to the different synthesis products thus simply represent a small but electrochemically recognizable sub-population of the total. The assignments as *average* core sizes coincide, however, with other results, given below.

Thiolate-protected Au MPCs have distinctive, size-dependent electronic spectra.^{54,58,62-68} Au MPCs with core radii $< ca. 0.7$ nm (such as Au₃₈³⁶) give optical spectra with a step-like pattern over *ca.* 300 to 500 nm, and a weaker band at *ca.* 700 nm. This fine structure is damped and largely featureless for MPCs with *ca.* 0.7 and 0.8 nm core radii (including Au₇₅⁴⁰ and Au₁₄₀³⁵). Au cores with radii $> ca. 1.0$ nm (including Au₂₂₅⁴² and Au₃₁₄⁵) exhibit a surface plasmon resonance (SPR) absorbance band at *ca.* 520 nm that grows in intensity with further increase in core size, approaching the spectrum of bulk metal.⁵

Against this literature background, the UV-vis absorbance spectra (Figure 3.2) for the four ferrocenated MPCs are consistent with the electrochemical core size assignments. The presumed ferrocenated Au₃₁₄ MPC has the strong SPR band expected for a larger Au core size, and the Au₂₂₅ core size assignment is consistent with the weak SPR band seen for the 2:1 thiol-to-Au synthetic product. Both the assigned Au₁₄₀ and Au₇₅ core sizes are consistent with the nearly featureless absorbance spectra observed in the figure.

The TEM images and histograms shown in Figure 3.3 confirm and complete the assignments of average core size for the four MPC samples. The samples are seen to have roughly $\pm 10\%$ poly-dispersity and have average core diameters that match the dimensions expected for Au₇₅, Au₁₄₀, Au₂₂₅ and Au₃₁₄ cores. Lattice plane spacings of 2.2 ± 0.1 Å, which we assign to the $\langle 111 \rangle$ planes of Au, can be seen in a high-resolution image of one

Figure 3.2. UV/Vis absorbance spectra for the four separately synthesized ferrocene hexanethiolate protected Au clusters in CH₂Cl₂.

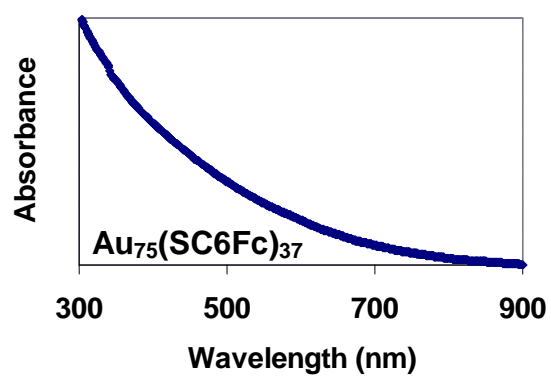
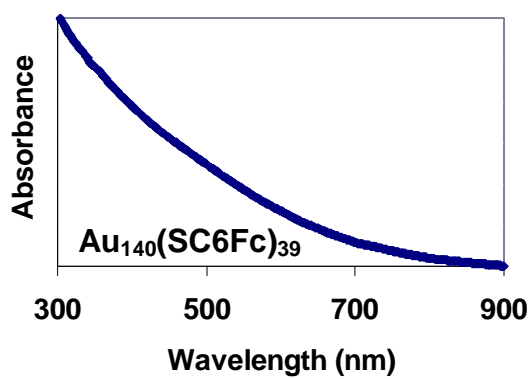
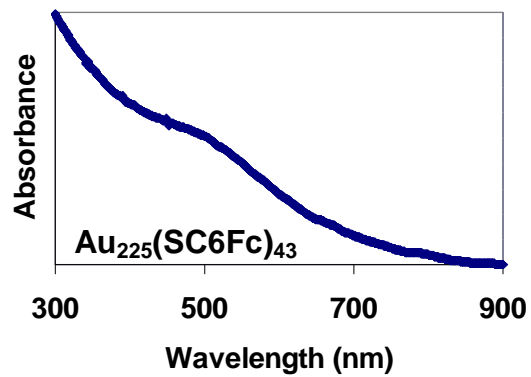
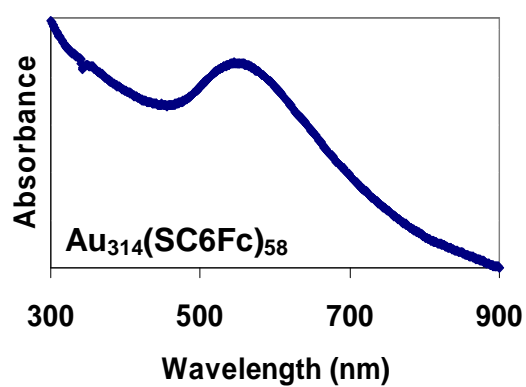
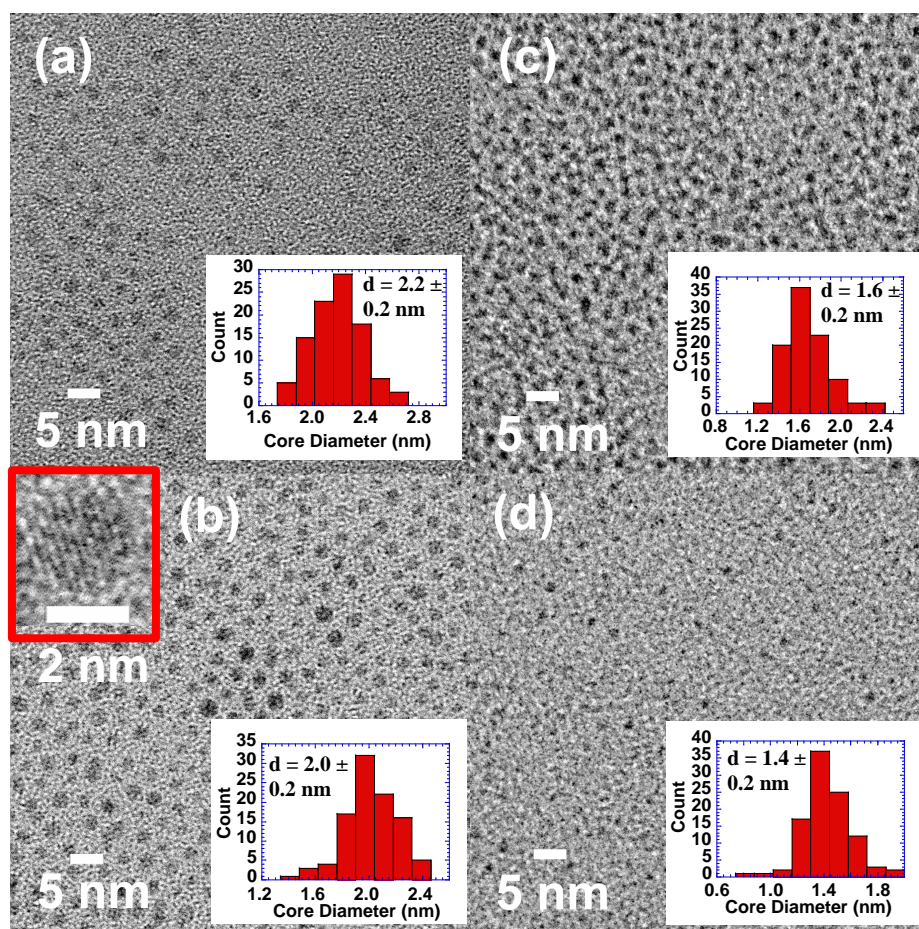


Figure 3.3. TEM images of (a) $\text{Au}_{314}(\text{SC6Fc})_{58}$, (b) $\text{Au}_{225}(\text{SC6Fc})_{43}$, (c) $\text{Au}_{140}(\text{SC6Fc})_{39}$, and (d) $\text{Au}_{75}(\text{SC6Fc})_{37}$. Corresponding core diameter histograms with average core diameters labeled, each from 100 sampled MPC cores, are inset in the bottom right corner of each image. Inset in the top left corner of (b) is a high-resolution image of a $\text{Au}_{225}(\text{SC6Fc})_{43}$ core clearly showing lattice planes.



of the MPCs (Figure 3.3b). The histograms show that the 1.4, 1.6, 2.0, and 2.2 nm core diameter MPCs comprise between 1/4 and 1/3 of the overall MPC population, which is consistent with the peak to background current ratios in the square wave voltammetry of Figure 3.1. Comparable TEM information for hexanethiolate-protected Au₇₅, Au₁₄₀, Au₂₂₅ and Au₃₁₄ MPCs is found in Figure 3.4.

Voltammetric Artifacts. As part of a careful examination of the patterns of QDL charging currents of the three larger MPCs, their CV curves were differentiated, with the (initially surprising) results of Figure 3.5. QDL peaks expected from the square wave voltammetry of Figure 3.1 appear as the larger derivative peaks, but there is an additional underlying pattern of smaller, evenly spaced peaks. Remarkably, the pattern of smaller peaks is *also* seen in the differentiated CV (Panel D, at two different sampling intervals) of an *MPC-free* electrolyte solution of composition identical to that used in the MPC voltammetry. The phenomenon was traced to the data sampling protocol of the electrochemical instrument. The small peaks in Figures 3.5A, B, C, and, for the top voltammogram, D are spaced by 30 – 40 mV. Upon closer investigation, it became clear that the smaller peak spacing is dependent on the sampling interval. The smaller peak spacing increases to 100 mV when the CV sweep data sampling interval is changed from the default of 1 mV to 4 mV, as shown in the lower voltammogram of Figure 3.5D.

We report the instrumental artifacts in Figure 3.5 as a caution; the use of digitally controlled potential scanning (e.g., staircase rather than linear potential sweep) and timed data-sampling associated with staircase sweeps are a common feature of modern electrochemical instrumentation. Searching for QDL voltammetry of larger MPCs, where peaks become naturally more closely spaced, is an important pioneer topic.^{47,48} Figure 3.5 for the present ferrocenated Au MPCs could hypothetically have been interpreted as

Figure 3.4. TEM images of (a) $\text{Au}_{314}(\text{SC6})_{91}$, (b) $\text{Au}_{225}(\text{SC6})_{75}$, (c) $\text{Au}_{140}(\text{SC6})_{53}$, and (d) $\text{Au}_{75}(\text{SC6})_{40}$. Corresponding core diameter histograms with average core diameters labeled, each from 100 sampled MPC cores, are inset in the bottom right corner of each image.

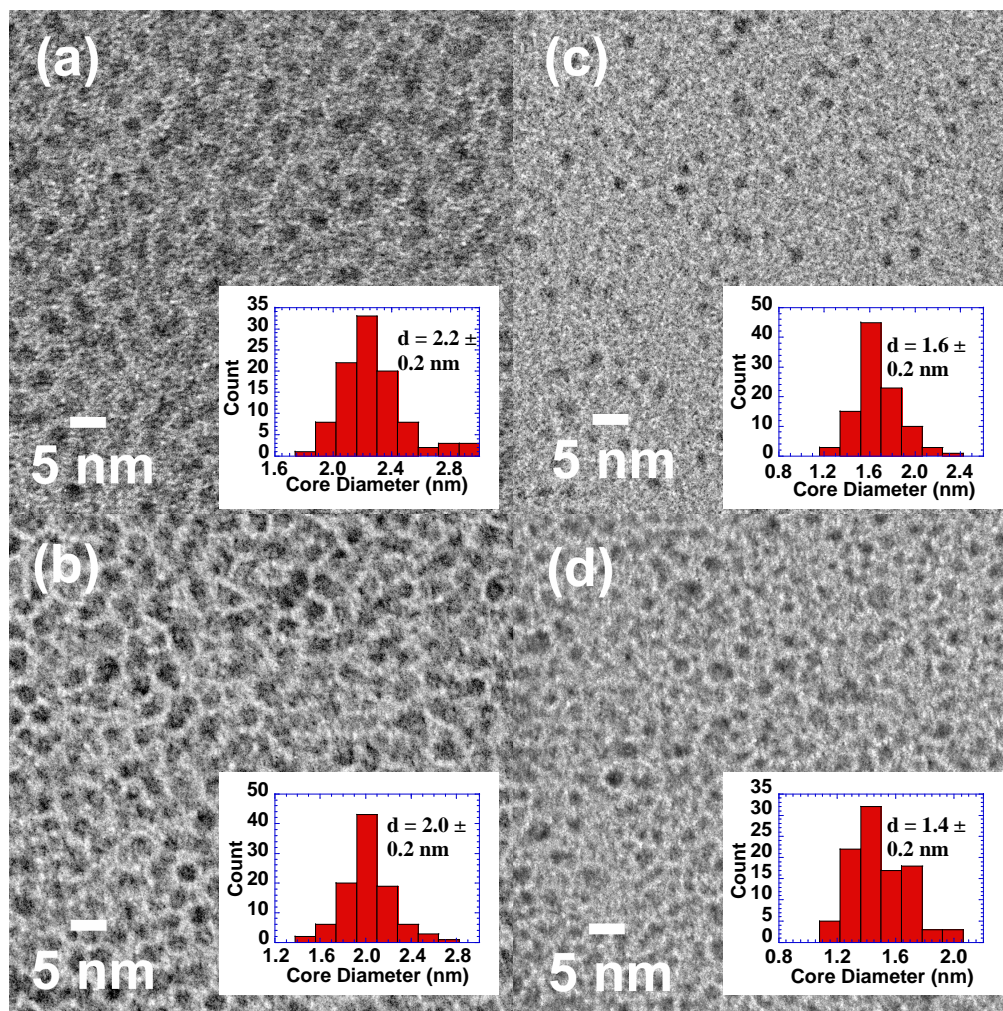
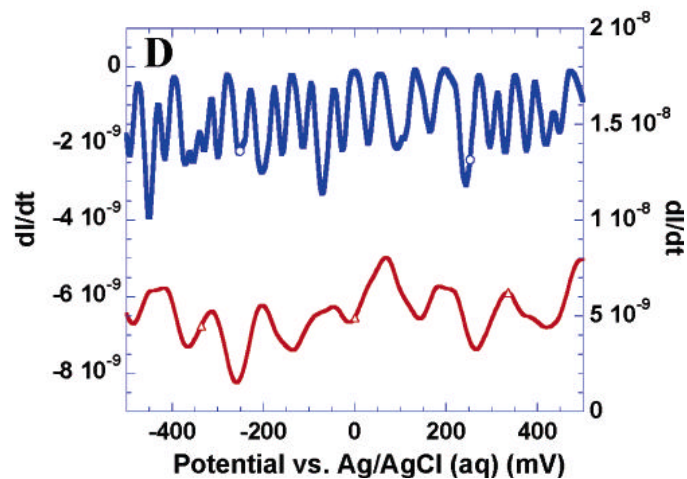
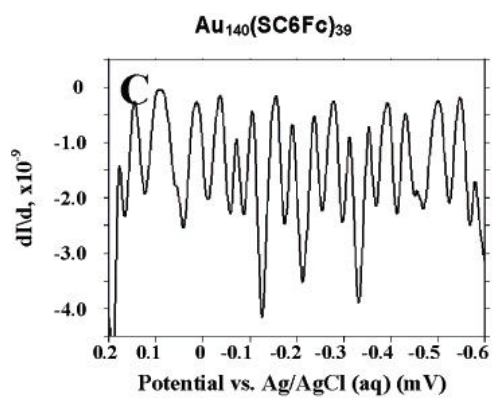
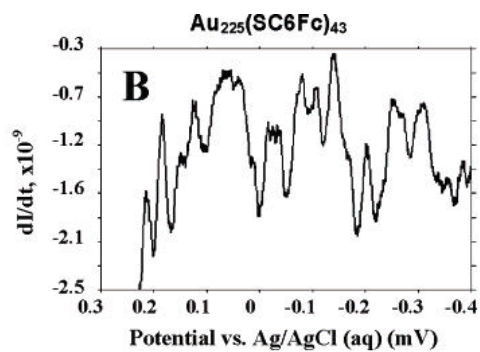
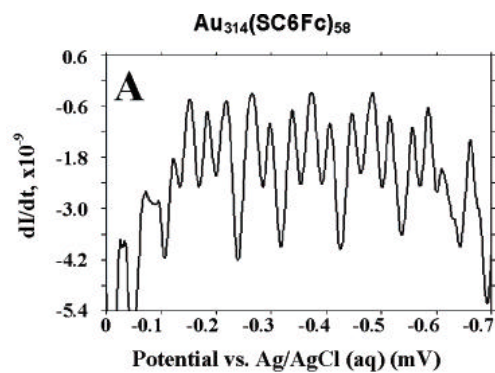


Figure 3.5. First derivative of the CV of (A) $\text{Au}_{314}(\text{SC6Fc})_{68}$, (B) $\text{Au}_{225}(\text{SC6Fc})_{43}$, and (C) $\text{Au}_{140}(\text{SC6Fc})_{39}$ done under Ar atmosphere at 284 K with potential scan rate of 100 mV/s and sample interval of 1 mV. First derivative of the CV of (D) 0.1 mM Bu_4NClO_4 in CH_2Cl_2 (*no MPC*) under identical conditions (blue, upper line, corresponding to left y-axis) and under identical conditions except with a sample interval of 4 mV (red, lower line, corresponding to right y-axis). The difference in sample interval is shown to demonstrate the dependence of peak spacing with sample interval and to show that 100 mV spacing can be achieved as in other references which attribute this spacing as QDL peaks.^{46,47}



signaling the presence of Au MPCs with significantly larger cores, and thus larger quantized double layer capacitances and smaller ΔV spacing between one-electron peaks. That interpretation (which we never made!) can be demonstrated as erroneous by changing the data-sampling interval and by observations in MPC-free solutions, as done above.

Determination of Number of Ferrocenated MPC Ligands. Our usual procedure for determining the average ligand count on Au MPCs is thermogravimetric analysis (TGA), a process in which the organic thiol fraction of the MPC is thermally evolved as disulfide, leaving elemental gold. This experiment proved inconclusive when applied to the ferrocenated Au MPCs. Instead of the usual roughly step-like mass loss seen when the thiolate ligands are thermolyzed, the mass loss was quite gradual and occurred over a large temperature range (100 – 600 °C). The TGA trace for the ferrocenated Au₂₂₅ MPC is compared to that for hexanethiolate-coated Au₂₂₅ in Figure 3.6B and C. Figure 3.6A shows that the TGA trace of the ferrocene-hexanethiol itself displays a sharp mass loss at a higher temperature (*ca.* 350 °C), but only *ca.* 28% of the thiol was vaporized, and a significant amount of visible rust residue was seen upon post-measurement inspection of the aluminum sample crucible. The incomplete vaporization of the ferrocene hexanethiol most likely causes the unexpectedly sluggish reaction of the ferrocenated clusters, and the TGA data proved not useful for these MPCs.

The average ligand count could, however, be assessed by direct constant potential coulometry (electrolysis). This experiment measures the redox capacity of the ferrocenated MPCs. The charge-time curves from bulk electrolysis of each MPC sample at a potential more positive than the Fc/Fc^+ formal potential are shown in Figure 3.7. The electrolysis was slow due to an inefficient cell design, but went to suitable completion. When the solution had been electrolyzed to a rest potential more positive than the Fc/Fc^+ formal

Figure 3.6. Thermogravimetric analysis (TGA) traces of (A) HSC6Fc, (B) Au₂₂₅(SC6Fc)₄₃, and (C) Au₂₂₅(SC6)₇₅, for comparison.

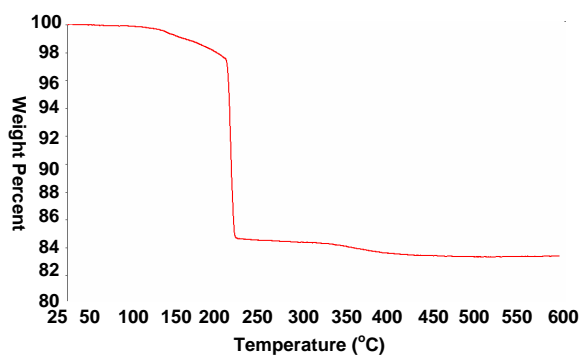
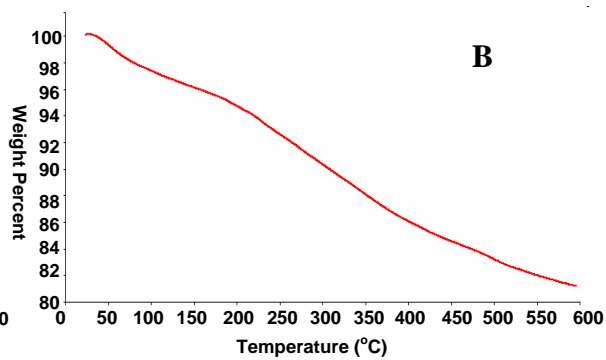
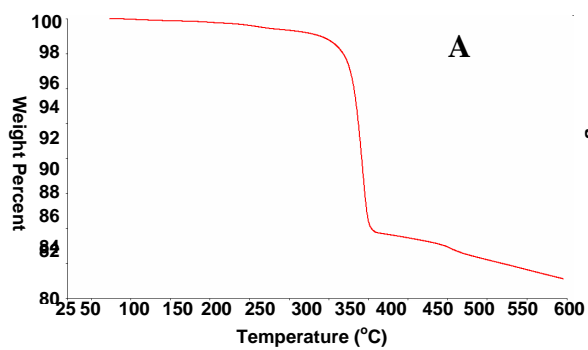
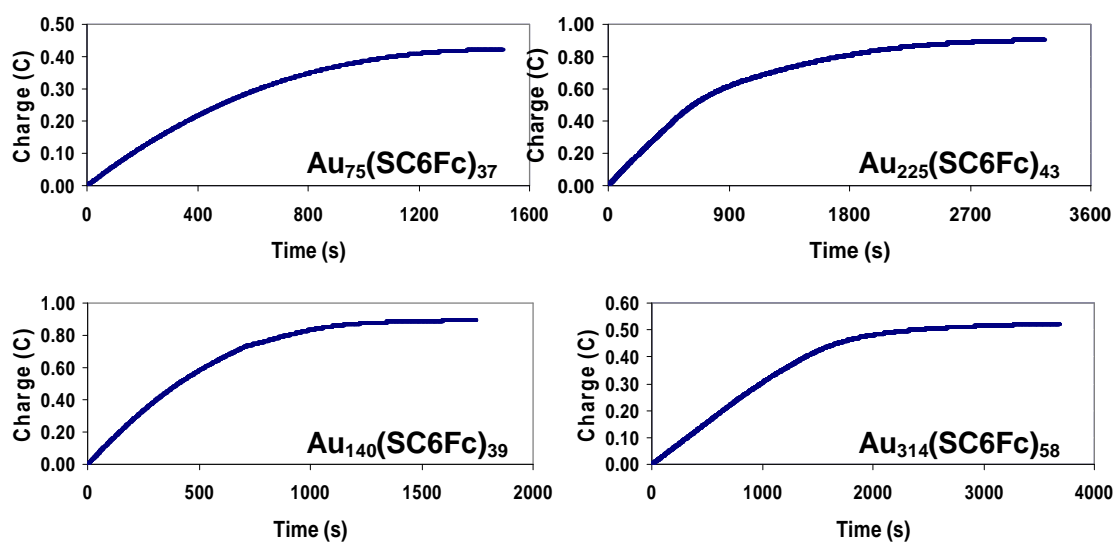


Figure 3.7. Bulk electrolysis charge vs. time curves for $\text{Au}_{75}(\text{SC6Fc})$, $\text{Au}_{140}(\text{SC6Fc})_{39}$, $\text{Au}_{225}(\text{SC6Fc})_{43}$, and $\text{Au}_{314}(\text{SC6Fc})_{58}$ at concentrations of 0.05 mM, 0.11 mM, 0.10 mM, and 0.04 mM, respectively, and over potential differences of 462 mV, 447 mV, 260 mV, and 230 mV, respectively. All measurements were performed in 50 mM Bu_4NClO_4 in CH_2Cl_2 using a Pt mesh working electrode, a Pt wire counter electrode (in a separate cell compartment), and a Ag/AgCl (aqueous) reference electrode.



potential, the solution had turned a blue-green color and a precipitate was observed. After the electrolysis was reversed (data not shown) by applying a potential more negative than the Fc/Fc^+ formal potential, in a dark brown solution similar to the original one resulted, with no precipitate remaining. The observed changes in color are consistent with ferrocene and ferrocenium colors, and the precipitation observed at positive potentials is due to the low solubility of oxidized ferrocenated MPCs in methylene chloride.

At the positive applied potential, both ferrocene and the Au core undergo electron loss, so that the total electrolysis charge (Q) can be expressed as:

$$Q = (n_{\text{CORE}} + n_{\text{LIGAND}})FN_{\text{MPC}} \quad (3)$$

where n_{CORE} is the total number of Au core electrons transferred (judged by the number of QDL peaks encompassed), n_{LIGAND} is the total number of ligand electrons transferred (from the Fc/Fc^+ redox centers), F is Faraday's constant, and N_{MPC} is moles of MPC present.

Since the molecular weight of the clusters could not be determined without the ligand count, the number of ligands and corresponding cluster molecular weight were assessed iteratively. For the electrolysis potentials used, $n_{\text{CORE}} = 1, 1, 2,$ and $2,$ respectively, for the $\text{Au}_{75}, \text{Au}_{140}, \text{Au}_{225}$ and Au_{314} cores. The equation assumes that the ferrocene sites react exhaustively; the CV behavior of the ferrocene wave of the MPCs gives no indication that the formal potentials have become widely distributed.

The results for n_{LIGAND} are given in Table 3.2, along with the ligand-to-surface Au atom ratio for each MPC. The analogous numbers for hexanethiolate-protected MPCs are listed for comparison. It is evident that the nanoparticle surface coverages of ferrocene hexanethiolate ligands are less dense than those of hexanethiolate ligands. This is unsurprising given the relative bulkiness of ferrocene as a head group. It is striking, however, that the hexanethiolate/ferrocene-hexanethiolate ligand ratio is small (1.1) for the

Table 3.2. Ligand Counts and Ligand/Surface Atom Coverages for Hexanethiolate and Fully Ferrocenated Hexanethiolate Monolayers, for Au MPCs of Varying Core Size

Avg. Core Size (# Surface Atoms)	# –SC6 Ligands, Lit. ^a (Ligand/Surface Atom ratio)	# –SC6Fc Ligands, Expt. ^b (Ligand/Surface Atom ratio)	# –SC6Fc Ligands, Calc. ^c (Ligands/Surface Atom ratio)	Refs.
Au ₇₅ (60)	40 (0.67)	37 (0.62)	36 (0.60)	40,69
Au ₁₄₀ (96)	53 (0.55)	39 (0.41)	41 (0.43)	5,35
Au ₂₂₅ (140)	75 (0.51)	43 (0.31)	48 (0.34)	5,42
Au ₃₁₄ (174)	91 (0.52)	58 (0.33)	57 (0.33)	5

^a Results of thermogravimetric analysis (TGA).

^b n_{LIGAND} results of constant potential coulometric electrolysis, not including n_{CORE}.

^c Numbers calculated based on surface areas of Au cores and of ferrocene molecules (as described in the text).

smallest Au core (Au₇₅), and rises to a rough plateau (1.6) for the two larger Au cores (Au₂₂₅ and Au₃₁₄). This behavior is qualitatively plausible; the Au₇₅ core surface has the strongest curvature and allows thereby a more acutely cone-shaped space for a ligand that has a large cross-section at its terminus. Said somewhat differently, recalling that the usual ligand/surface atom ratio for self assembled monolayers on flat Au(111) terrace surfaces is 0.33, the Au₇₅ core has a larger proportion of vertex and edge binding sites—relative to terraces. The relative proportion of terrace sites for Au₂₂₅ and Au₃₁₄ cores is larger, and changes by only a modest factor between these two core sizes.

The ferrocenated MPCs maximize the redox capacity by the design of a fully occupied monolayer shell, but at the same time encounter constraints imposed by the steric bulk of the redox moiety. That the ligand surface coverages in Table 3.2 do reflect steric limitations is supported by modeling of the ferrocenated monolayer shell to estimate the number of ferrocenes that could theoretically fit around each core size. Using a 1.5 nm² “headprint” of Fc molecules (based on⁷⁰ a Fc C-C bond length of 1.43 Å and a Fc Fe-C bond length of 2.06 Å) arranged as a sphere of radius equal to the average Au core radius plus the –SC₆Fc chainlength, the number of Fc molecules that can fit into such a sphere was calculated as given in Table 3.2. The calculations are in excellent agreement with the experimental results for electroactive ferrocene hexanethiolate ligands. Thus, it would seem possible that redox capacities for other fully redox-labeled MPCs could be anticipated from simple model calculations assuming steric constraints dominate the coverage.

Preliminary Results in the Investigation of the Electrochemical Properties of the Ferrocenated Au MPCs. These novel ferrocenated MPCs are unique in that they are stabilized by full monolayers of redox moieties despite the obvious steric hindrances of the bulky ligands. The shape of the cyclic voltammogram of Au₇₅(SC₆Fc)₃₇ shown in Figure

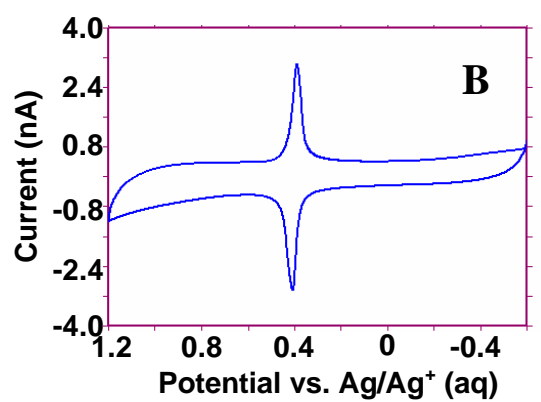
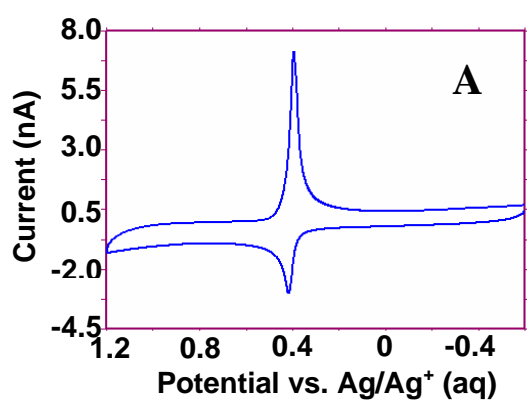
3.1A shows a multiple one-electron transfer, indicating that the Fc redox groups act independently and do not influence each other. However, in preliminary studies that investigate more thoroughly the electrochemical properties of these fully ferrocenated nanoparticles, several interesting electrochemical phenomena have been observed. Presented here is a preview of the upcoming electrochemical studies performed on these unique clusters.

At high supporting electrolyte concentrations, the ferrocenated Au MPCs adsorb strongly onto the Pt working electrode, and very sharp peaks are observed in cyclic voltammetry (Figure 3.8A). The adsorbed film is typically a monolayer thick and is highly stable. Electrochemistry can be performed on the adsorbed clusters in a blank electrolyte solution with the film on the electrode which also leads to distinct, sharp peaks (Figure 3.8B). The shape of the cyclic voltammograms of the solution as well as the film of ferrocenated Au MPCs seems to be highly scan rate dependent. These new observations are intriguing and will not be discussed further in this chapter, but they do offer some insight into the novelty of these nanoparticles.

3.4 Conclusions

Notable in the syntheses of ferrocenyl-hexanethiolate Au MPCs is that a synthetic protocol known to deliver hexanethiolate coated MPCs of a certain average Au core atom count, delivers the *same* average Au core atom count for ferrocenated MPCs. This occurs in spite of substantial changes in the surface coverage of ligands (Table 3.2) prompted by steric interactions between the ferrocene head groups. This result informs about processes occurring during the complex reduction reaction, thought to be a sequence of core nucleation, growth, and passivation. The core growth kinetics must be quite non-uniform, pausing at the thermodynamic minima represented by the closed shell atom counts

Figure 3.8. (A) Cyclic voltammogram of solution of 0.1 mM $\text{Au}_{225}(\text{SC6Fc})_{43}$ in 1 M $\text{Bu}_4\text{NPF}_6/\text{CH}_2\text{Cl}_2$ under Ar atmosphere, at 284 K, potential scan rate 25 mV/s. (B) After solution electrochemistry is performed, electrode is rinsed with 1 M $\text{Bu}_4\text{NPF}_6/\text{CH}_2\text{Cl}_2$ and used to take cyclic voltammogram of *MPC-free* solution of 1 M $\text{Bu}_4\text{NPF}_6/\text{CH}_2\text{Cl}_2$ under Ar atmosphere, at 284 K, potential scan rate 25 mV/s.



discussed above (ignoring probabilities for variability of truncation at vertices). One might expect, based on the diminished ligand/surface atom coverage results, that the passivation kinetics attained by a ferrocene hexanethiolate ligand might be more sluggish than those of unlabeled hexanethiolates. The thermodynamics favoring closed shells seem however, to dominate any change in passivation dynamics.

The redox capacity of these ferrocenated Au MPCs depends on several variables. In terms of charge/volume, the redox capacity, measured in surface area/volume, is expected to increase inversely with the overall MPC radius, meaning the Au core radius plus the linker chain length. Similarly, the double-layer charge capacity also increases inversely with the Au core radius. Thus, the choice of the four average core sizes of nanoparticles that were discussed is a logical one based on their size regime. The smallest Au cores studied have the highest radii of curvature, and also have the highest ligand-to-surface ratio due to the lessening of the steric hindrances of the bulky redox species. As the gold core increases in size, the radius of curvature decreases, and, consequently, the ligand-to-surface ratio declines. Finally, as seen in the voltammetry of the ferrocenated Au nanoparticles, each of the multitude of redox moieties on the Au cores exhibits the same electrochemical behavior. Combining the quantized double-layer charging of the gold core within a certain size regime (*ca.* 0.8 to 2.0 nm core radius) and the high redox capacity of the Fc-functionalized monolayer, these new MPCs have the ability to transfer many electrons within a small potential range, up to 60 per Au core for the largest sized MPC discussed. The impact of this ability remains to be further explored in the energy storage context, such as supercapacitors and batteries, and is under continued study.

3.5 Acknowledgments

This research was supported by grants from the National Science Foundation and Office of Naval Research. Contributions from Dr. Ramjee Balasubramanian, and Dr. Joseph Tracy from the University of North Carolina are also acknowledged.

3.6 References

- (1) Hayat, M. A. *Colloidal Gold: Principles, Methods, and Applications*; Academic Press: San Diego, 1991.
- (2) Schmid, G. *Clusters and Colloids*; VCH: Weinheim, 1994.
- (3) Daniel, M. C.; Astruc, D. *Chem. Rev.* **2004**, *104*, 293-346.
- (4) Templeton, A. C.; Wuelfing, M. P.; Murray, R. W. *Accounts of Chemical Research* **2000**, *33*, 27-36.
- (5) Hostetler, M. J.; Wingate, J. E.; Zhong, C.-J.; Harris, J. E.; Vachet, R. W.; Clark, M. R.; Londono, J. D.; Green, S. J.; Stokes, J. J.; Wignall, G. D.; Glish, G. L.; Porter, M. D.; Evans, N. D.; Murray, R. W. *Langmuir* **1998**, *14*, 17-30.
- (6) Templeton, A. C.; Hostetler, M. J.; Warmoth, E. K.; Chen, S. W.; Hartshorn, C. M.; Krishnamurthy, V. M.; Forbes, M. D. E.; Murray, R. W. *J. Am. Chem. Soc.* **1998**, *120*, 4845-4849.
- (7) Hostetler, M. J.; Templeton, A. C.; Murray, R. W. *Langmuir* **1999**, *15*, 3782-3789.
- (8) Hicks, J. F.; Templeton, A. C.; Chen, S. W.; Sheran, K. M.; Jasti, R.; Murray, R. W.; Debord, J.; Schaaf, T. G.; Whetten, R. L. *Anal. Chem.* **1999**, *71*, 3703-3711.
- (9) Guo, R.; Murray, R. W. *J. Am. Chem. Soc.* **2005**, *127*, 12140-12143.
- (10) Miles, D. T.; Murray, R. W. *Anal. Chem.* **2001**, *73*, 921-929.
- (11) Green, S. J.; Pietron, J. J.; Stokes, J. J.; Hostetler, M. J.; Vu, H.; Wuelfing, W. P.; Murray, R. W. *Langmuir* **1998**, *14*, 5612-5619.
- (12) Hostetler, M. J.; Green, S. J.; Stokes, J. J.; Murray, R. W. *J. Am. Chem. Soc.* **1996**, *118*, 4212-4213.
- (13) Templeton, A. C.; Cliffel, D. E.; Murray, R. W. *J. Am. Chem. Soc.* **1999**, *121*, 7081-7089.
- (14) Song, Y.; Heien, M.; Jimenez, V.; Wightman, R. M.; Murray, R. W. *Anal. Chem.* **2004**, *76*, 4911-4919.
- (15) Green, S. J.; Stokes, J. J.; Hostetler, M. J.; Pietron, J.; Murray, R. W. *J. Phys. Chem. B* **1997**, *101*, 2663-2668.
- (16) Ingram, R. S.; Hostetler, M. J.; Murray, R. W. *J. Am. Chem. Soc.* **1997**, *119*, 9175-9178.

- (17) Ingram, R. S.; Murray, R. W. *Langmuir* **1998**, *14*, 4115-4121.
- (18) Templeton, A. C.; Hostetler, M. J.; Kraft, C. T.; Murray, R. W. *J. Am. Chem. Soc.* **1998**, *120*, 1906-1911.
- (19) Shimmin, R. G.; Schoch, A. B.; Braun, P. V. *Langmuir* **2004**, *20*, 5613-5620.
- (20) Thunemann, A. F.; Beyermann, J. *Macromolecules* **2000**, *33*, 6878-6885.
- (21) Paulini, R.; Frankamp, B. L.; Rotello, V. M. *Langmuir* **2002**, *18*, 2368-2373.
- (22) Boal, A. K.; Das, K.; Gray, M.; Rotello, V. M. *Chem. Mat.* **2002**, *14*, 2628-2636.
- (23) Liu, P.; Rodriguez, J. A.; Muckerman, J. T. *J. Chem. Phys.* **2004**, *121*, 10321-10324.
- (24) Liu, P.; Rodriguez, J. A.; Muckerman, J. T. *J. Phys. Chem. B* **2004**, *108*, 15662-15670.
- (25) Murray, R. W. *Accounts of Chemical Research* **1980**, *13*, 135-141.
- (26) Porter, M. D.; Bright, T. B.; Allara, D. L.; Chidsey, C. E. D. *J. Am. Chem. Soc.* **1987**, *109*, 3559-3568.
- (27) Chidsey, C. E. D.; Bertozzi, C. R.; Putvinski, T. M.; Majsce, A. M. *Journal of the American Chemical Society* **1990**, *112*, 4301-4306.
- (28) Flanagan, J. B.; Margel, S.; Bard, A. J.; Anson, F. C. *J. Am. Chem. Soc.* **1978**, *100*, 4248-4253.
- (29) Cuadrado, I.; Moran, M.; Casado, C. M.; Alonso, B.; Lobete, F.; Garcia, B.; Ibisate, M.; Losada, J. *Organometallics* **1996**, *15*, 5278-5280.
- (30) Yoneyama, H.; Shoji, Y.; Kawai, K. *Chem. Lett.* **1989**, 1067-1070.
- (31) Lira-Cantu, M.; Gomez-Romero, P. *Chem. Mat.* **1998**, *10*, 698-704.
- (32) Ung, T.; Giersig, M.; Dunstan, D.; Mulvaney, P. *Langmuir* **1997**, *13*, 1773-1782.
- (33) Echegoyen, L.; Echegoyen, L. E. *Accounts of Chemical Research* **1998**, *31*, 593-601.
- (34) Ingram, R. S.; Hostetler, M. J.; Murray, R. W.; Schaaff, T. G.; Khoury, J. T.; Whetten, R. L.; Bigioni, T. P.; Guthrie, D. K.; First, P. N. *J. Am. Chem. Soc.* **1997**, *119*, 9279-9280.
- (35) Hicks, J. F.; Miles, D. T.; Murray, R. W. *J. Am. Chem. Soc.* **2002**, *124*, 13322-13328.

- (36) Jimenez, V. L.; Leopold, M. C.; Mazzitelli, C.; Jorgenson, J. W.; Murray, R. W. *Anal. Chem.* **2003**, *75*, 199-206.
- (37) Chen, S. W.; Murray, R. W.; Feldberg, S. W. *J. Phys. Chem. B* **1998**, *102*, 9898-9907.
- (38) Lee, D.; Donkers, R. L.; Wang, G. L.; Harper, A. S.; Murray, R. W. *J. Am. Chem. Soc.* **2004**, *126*, 6193-6199.
- (39) Jimenez, V. L.; Georganopoulou, D. G.; White, R. J.; Harper, A. S.; Mills, A. J.; Lee, D. I.; Murray, R. W. *Langmuir* **2004**, *20*, 6864-6870.
- (40) Balasubramanian, R.; Guo, R.; Mills, A. J.; Murray, R. W. *J. Am. Chem. Soc.* **2005**, *127*, 8126-8132.
- (41) Brennan, J. L.; Branham, M. R.; Hicks, J. F.; Osisek, A. J.; Donkers, R. L.; Georganopoulou, D. G.; Murray, R. W. *Anal. Chem.* **2004**, *76*, 5611-5619.
- (42) Wolfe, R. L.; Murray, R. W. *Anal. Chem.* **2006**, *78*, 1167-1173.
- (43) Quinn, B. M.; Liljeroth, P.; Ruiz, V.; Laaksonen, T.; Kontturi, K. *J. Am. Chem. Soc.* **2003**, *125*, 6644-6645.
- (44) Yang, Y.; Pradhan, S.; Chen, S. *Journal of American Chemical Society* **2004**, *126*, 76-77.
- (45) Kim, Y. G.; Garcia-Martinez, J. C.; Crooks, R. M. *Langmuir* **2005**, *21*, 5485-5491.
- (46) Chaki, N. K.; Singh, P.; Dharmadhikari, C. V.; Vijayamohanan, K. P. *Langmuir* **2004**, *20*, 10208-10217.
- (47) Chaki, N. K.; Kakade, B.; Sharma, J.; Mahima, S.; Vijayamohanan, K. P.; Haram, S. K. *J. Appl. Phys.* **2004**, *96*, 5032-5036.
- (48) Brauer, G. *Handbook of Preparative Inorganic Chemistry*; Academic Press: New York, 1965.
- (49) Yu, C. J.; Wang, H.; Wan, Y. J.; Yowanto, H.; Kim, J. C.; Donilon, L. H.; Tao, C. L.; Strong, M.; Chong, Y. C. *J. Org. Chem.* **2001**, *66*, 2937-2942.
- (50) Brust, M.; Walker, M.; Bethell, D.; Schiffrin, D. J.; Whyman, R. *J. Chem. Soc.-Chem. Commun.* **1994**, 801-802.
- (51) Cliffel, D. E.; Zamborini, F. P.; Gross, S. M.; Murray, R. W. *Langmuir* **2000**, *16*, 9699-9702.

- (52) Templeton, A. C.; Chen, S. W.; Gross, S. M.; Murray, R. W. *Langmuir* **1999**, *15*, 66-76.
- (53) Huang, T.; Murray, R. W. *Langmuir* **2002**, *18*, 7077-7081.
- (54) Huang, T.; Murray, R. W. *J. Phys. Chem. B* **2001**, *105*, 12498-12502.
- (55) Li, D.; Zhang, Y. J.; Jiang, J. G.; Li, J. H. *J. Colloid Interface Sci.* **2003**, *264*, 109-113.
- (56) Schmid, G.; Pfeil, R.; Boese, R.; Bandermann, F.; Meyer, S.; Calis, G. H. M.; Vandervelden, W. A. *Chem. Ber.-Recl.* **1981**, *114*, 3634-3642.
- (57) Merz, A.; Bard, A. J. *J. Am. Chem. Soc.* **1978**, *100*, 3222-3223.
- (58) Chen, S. W.; Ingram, R. S.; Hostetler, M. J.; Pietron, J. J.; Murray, R. W.; Schaaff, T. G.; Khoury, J. T.; Alvarez, M. M.; Whetten, R. L. *Science* **1998**, *280*, 2098-2101.
- (59) Chen, S. W.; Murray, R. W. *J. Phys. Chem. B* **1999**, *103*, 9996-10000.
- (60) Wang, G. L.; Huang, T.; Murray, R. W.; Menard, L.; Nuzzo, R. G. *J. Am. Chem. Soc.* **2005**, *127*, 812-813.
- (61) Yang, Y.; Chen, S. *Nano Lett.* **2003**, *3*, 75-79.
- (62) Kreibig, U.; Vollmer, M. *Optical Properties of Metal Clusters*; Springer-Verlag: New York, 1995.
- (63) Underwood, S.; Mulvaney, P. *Langmuir* **1994**, *10*, 3427-3430.
- (64) Mulvaney, P. *Langmuir* **1996**, *12*, 788-800.
- (65) Kreibig, U.; Fauth, K.; Quinten, M.; Schonauer, D. *Z. Phys. D-Atoms Mol. Clusters* **1989**, *12*, 505-514.
- (66) Alvarez, M. M.; Khoury, J. T.; Schaaff, T. G.; Shafigullin, M. N.; Vezmar, I.; Whetten, R. L. *J. Phys. Chem. B* **1997**, *101*, 3706-3712.
- (67) Schaaff, T. G.; Shafigullin, M. N.; Khoury, J. T.; Vezmar, I.; Whetten, R. L.; Cullen, W. G.; First, P. N.; GutierrezWing, C.; Ascensio, J.; JoseYacaman, M. J. *J. Phys. Chem. B* **1997**, *101*, 7885-7891.
- (68) Landes, C. F.; Braun, M.; El-Sayed, M. A. *J. Phys. Chem. B* **2001**, *105*, 10554-10558.
- (69) Cleveland, C. L.; Landman, U.; Schaaff, T. G.; Shafigullin, M. N.; Stephens, P. W.; Whetten, R. L. *Phys. Rev. Lett.* **1997**, *79*, 1873-1876.

CHAPTER IV

ANION INDUCED ADSORPTION OF FERROCENATED NANOPARTICLES

4.1 Introduction

Adsorption of ions and molecules from solutions onto electrodes and electrified interfaces is a common chemical phenomenon. During a study¹ of the electrochemistry of Au nanoparticles capped with monolayers of ferrocene alkanethiolate ligands (monolayer protected clusters, MPCs), we noticed an uncommon aspect—a nearly irreversible adsorption of a *monolayer* of *w*-ferrocenyl hexanethiolate-functionalized MPCs from CH₂Cl₂ solutions onto Pt electrodes. Further study of this adsorption has been carried out and the present report will show that the adsorption of the MPC (Au₂₂₅[(S(CH₂)₆Fc)]) is a slow, cooperative process, requiring the presence of high concentrations of particular electrolytes.

While studying the adsorption of the ferrocenated MPCs, several unusual properties of the electroactive film were discovered. Firstly, the monolayer is robust, persisting after rinsing, soaking, or sonication of the electrode in solvent (with or without dissolved electrolyte). After transferring the electrode to a nanoparticle-free CH₂Cl₂ electrolyte solution, well-defined stable voltammetry of the ferrocene ligands (*ca.* 43 per nanoparticle) can be observed. The full-width-half-maximum (E_{FWHM}) of the voltammetric peak (for monolayer and sub-monolayer coverage, *ca.* 35 mV) is considerably narrower than the value expected (90.6 mV at 298 K) for an electroactive monolayer. Interestingly, the

electrode's double layer capacitance is virtually unchanged by the adsorbed layer of MPCs. The adsorbed nanoparticles can be removed by applying potentials estimated to be more negative than the electrode's potential of zero charge, and the adsorption is completely blocked by the presence of a dodecanethiolate self-assembled monolayer. This paper will analyze the above, collectively unusual, effects.

The charge under the peaks of a cyclic voltammogram of an electroactive film on a electrode, i.e. a chemically modified electrode,²⁻⁹ gives the total surface coverage, Γ_T (mol/cm²). Many adsorbed species display near-ideal behavior, but reactions with slow monolayer electron transfer kinetics are known,¹⁰⁻¹² as are voltammetric waveshapes attributed to non-ideal surface activities,^{13,14} environmental or dipolar heterogeneity of redox sites,¹⁵⁻¹⁸ ion-pairing between redox species and electrolyte counter ions,^{19,20} and interfacial potential distribution.²¹ In the particular case of ferrocene, there are examples of adsorption from solutions that are either concentrated^{22,23} or involve a poorly solvating medium (aqueous),²⁴ adsorption of ferrocenated dendrimers,²⁵ precipitation of poly(vinylferrocenium),^{15,26-29} electrodeposition of biferrocene derivative-attached gold nanopartilces,³⁰⁻³⁵ and binding through alkanethiolate¹⁶ or siloxane linkages.^{16,36} Amongst all these reports, however, there is none of a slow, electrolyte-induced, irreversible adsorption of a *monolayer* of a ferrocenated species that yields a voltammetric surface wave that is more narrow than the ideal $E_{FWHM} = 90.6$ mV.

The ferrocenated Au MPC used has an *average* Au₂₂₅(*w*-ferrocenyl hexanethiolate)₄₃ composition and is one of a series¹ of MPCs with *average* 75, 140, 225, and 314 Au atom core sizes with *ca.* 37, 39, 43, and 48 ferrocenyl ligands, respectively. These nanoparticles all display the size-dependent voltammetry known for their non-ferrocenated alkanethiolate analogs—quantized one-electron double layer charging³⁷⁻⁴⁷ for the three larger cores and a

molecule-like energy gap^{43,48} for the Au₇₅ case. However, for these nanoparticles, the currents associated with the quantized charging are dwarfed by the much larger and more quantitatively definable currents associated with the oxidation or reduction of the multiple (*ca.* 43) ferrocene sites in the protecting monolayer surrounding each Au₂₂₅ core. We focus on the latter currents in this study of ferrocenated MPC adsorption.

4.2 Experimental

Chemicals. Hexanethiol (HSC6, >99%), dodecanethiol (HSC12, >99%), *t*-octylammonium bromide (Oct₄NBr, >98%), sodium borohydride (NaBH₄, >98%), *t*-butylammonium perchlorate (Bu₄NClO₄, >99%), *t*-butylammonium *p*-toluenesulfonate (Bu₄NC₇H₈O₃S, pure), and *t*-butylammonium hexafluorophosphate (Bu₄NPF₆, pure) from Aldrich, and toluene (reagent grade), acetonitrile (Optima), methylene chloride (HPLC grade), tetrahydrofuran (HPLC grade), and ethanol (HPLC grade) from Fisher were used as received. HAuCl₄·xH₂O (from 99.999% pure gold) was synthesized using a literature procedure⁴⁹ and stored in a freezer at -20°C. Water was purified using a Barnstead NANOpure system (18 MO).

Ferrocene hexanethiol (HSC6Fc) was synthesized by refluxing a mixture of (1.11 g, 3.17 mmol) *w*-bromohexane ferrocene (prepared by a published method⁵⁰) and thiourea (0.600 g, 7.88 mmol) in ethanol (50 mL) overnight. The reaction mixture was neutralized with NaOH (aq), refluxed for a further 3 h, and then acidified with HCl to pH ~ 2, diluted with water and extracted with CH₂Cl₂, washing the organic extract phase copiously with water. The material obtained after rotary evaporation of the CH₂Cl₂ product solution was chromatographed on silica gel with ethyl acetate/hexanes. ¹H NMR (400 MHz, CD₂Cl₂) of the thiol gave the appropriate NMR peaks: d = 4.0 (m, 9 H), 2.49 (q, J = 7.2 Hz, 2 H), 2.30 (t, J = 7.6 Hz, 2 H), 1.56 (m, 2 H), 1.46 (m, 2 H), and 1.32 (m, 5 H) ppm with no dithiol

peaks present and no significant broadening, indicating that the majority of the ferrocenyl groups were in the reduced state.

MPC synthesis. $\text{Au}_{225}(\text{SC6Fc})_{43}$ was synthesized as previously described.¹ Briefly, vigorous mixing of 3.19 g $\text{HAuCl}_4 \cdot x\text{H}_2\text{O}$ in 100 mL deionized water with 5.20 g Oct_4NBr in 200 mL toluene, gave a clear aqueous phase and an orange-brown toluene phase.

Adding *w*-ferrocenyl hexanethiol to the isolated organic phase (2:1 ligand-to-Au mole ratio) gave a colorless reaction mixture that was stirred for 20 minutes and then cooled to 0 °C. 3.8 g of NaBH_4 in 10 mL water was added with very rapid stirring and reacted for 1 hour at 0 °C, after which the dark organic phase was collected and the solvent removed on a rotary evaporator at room temperature. The black solid suspension was stirred in 400 mL of acetonitrile for 6 hours and the solid product collected and washed with acetonitrile on a fine glass frit. Determination of the average Au core size and number of ligands has been presented elsewhere,¹ based on transmission electron microscopy, UV/Vis absorbance spectroscopy, cyclic and differential pulse voltammetry, and constant potential coulometry.

A mixed monolayer MPC with a lower ferrocene population (*average* composition, by NMR, $\text{Au}_{225}(\text{SC6})_{58}(\text{SC6Fc})_{17}$) was prepared by a ligand place exchange between $\text{Au}_{225}(\text{SC6})_{75}$ (prepared as previously described⁴¹) and HSC6Fc at a 1:1 mole ratio of *w*-ferrocenyl hexanethiol to hexanethiolate ligand. A 10-mL tetrahydrofuran solution of 0.020 g $\text{Au}_{225}(\text{SC6})_{75}$ and 0.0089 g HSC6Fc was stirred for 1 hr, the solvent removed, and the mixed monolayer MPCs rinsed with acetonitrile to remove excess thiols. The relative number of the two thiolate ligands on the exchanged product was analyzed in CD_2Cl_2 solution with ^1H NMR on a Bruker 400 MHz Avance spectrometer with a 5 s relaxation delay time.

Electrochemistry. Voltammetry of typically 0.1 mM MPC degassed CH₂Cl₂ solutions containing varying concentrations of electrolyte was done at 1.5 mm Pt disk (working), Pt wire (counter), and Ag/AgCl/3 M KCl (aq) electrodes using a Model 100B Bioanalytical Systems (BAS) Electrochemical Analyzer. The Pt working electrode was polished (0.25 μ m diamond, Buehler) and cleaned electrochemically by potential cycling in 0.10 M H₂SO₄ solution. Its roughness factor (2.9) was determined from the charge under the hydrogen desorption peak in voltammetry of 0.1.0 M H₂SO₄, using the standard⁹ 210 μ C/cm².

In survey experiments probing the general features of the adsorption, clean Pt electrodes were exposed to 0.05 mM Au₂₂₅(SC6Fc)₄₃ MPC solutions in CH₂Cl₂ containing given concentrations of Bu₄N⁺X⁻ electrolyte (X⁻ = ClO₄⁻, PF₆⁻, or p-toluene sulfonate⁻) while cyclically scanning the electrode at 0.50 V/s twenty-five times between 0.2 and 1.0 V (vs. Ag/AgCl) (a total scanning time of 80 seconds), followed by rinsing the electrode with MPC-free solvent/electrolyte and placing it in an MPC-free solution of the same electrolyte concentration. Electrodes were also exposed to 0.05 mM MPC solutions in 1.0, 0.10, or 0.010 M Bu₄NClO₄/CH₂Cl₂ for three minutes without potential scanning; the electrode was then rinsed with and immersed in an MPC-free solution of the same concentration of Bu₄NClO₄.

Surface coverages, Γ_{MPC} (mol MPC/cm²), of adsorbed MPCs were calculated from the charge, Q , under the voltammetric current peaks in MPC-free electrolyte solution, using

$$Q = nFA_m\Gamma_{\text{MPC}} \quad (1)$$

where n is the number of ferrocenes per MPC (average 43, by previous coulometry¹) and A_m is the Pt electrode area corrected for roughness. The experimentally determined values of Γ_{MPC} are compared to estimates of a model MPC monolayer, based on an overall 2.4 nm

MPC radius (summing Au core radius and length of the monolayer chain, including the ferrocene), giving $18.1 \text{ nm}^2/\text{MPC}$, or $\Gamma_{\text{MONO,MPC}} \sim 9 \times 10^{-12} \text{ mol MPC/cm}^2$. In all cases, the clean-electrode double layer current background was subtracted in determining the voltammetric charge.

Adsorption Kinetics. Three different protocols were employed to measure the rate of MPC adsorption. In one, called the *fixed-time* experiment, a clean Pt electrode was exposed to a CH_2Cl_2 electrolyte solution containing either 1.0 M Bu_4NClO_4 or 1.0 M Bu_4NPF_6 electrolyte and eight different concentrations of ferrocenated MPC ranging from 0.030 mM to 1.0 mM. The electrode potential was cyclically scanned between 0 and 0.8 V (*vs.* Ag/AgCl) twenty-five times at 0.50 V/s (a total scanning time of 80 seconds); the electrode was then rinsed with MPC-free 1.0 M electrolyte and placed in MPC-free 1.0 M electrolyte/ CH_2Cl_2 . Five preliminary CV scans at 0.10 V/s were done to remove any loosely adsorbed MPCs. Surface coverages were assessed by cyclic voltammetry of the ferrocene wave in the MPC-free electrolyte; ferrocene wave charges assessed in 0 to 0.80 V *vs.* Ag/AgCl scans at six different potential scan rates (0.025 – 2.000 V/s) were independent of scan rate. The Pt working electrode was then re-polished (0.25 μm diamond paste, Buehler), rinsed, and exposed to the next concentration of ferrocenated MPCs.

In a second adsorption-kinetics protocol, called the *no-scan* protocol, the Pt disk electrode was exposed at open circuit to 0.05 mM $\text{Au}_{225}(\text{SC6Fc})_{43}$ in 1.0 M $\text{Bu}_4\text{NClO}_4/\text{CH}_2\text{Cl}_2$ for chosen periods of time. (The typical open circuit electrode potential was 0.2 to 0.3V *vs.* Ag/AgCl). The electrode was rinsed with and immersed in MPC-free 1.0 M $\text{Bu}_4\text{NClO}_4/\text{CH}_2\text{Cl}_2$, and Γ_{MPC} was determined by scanning over the ferrocene wave

at 0.025 V/s (after preliminary scans as above). The electrode was polished as above and returned to the MPC solution for another period of (no-scan) exposure.

In the third adsorption kinetics protocol, called the *scanning* protocol, the potential of the Pt disk electrode, in 0.05 mM Au(SC6Fc)₄₃ in 1.0 M Bu₄NClO₄/CH₂Cl₂, was scanned at 0.50 V/s from 0 to 0.80 V vs. Ag/AgCl for chosen periods of time. Then, the electrode was rinsed with and immersed in MPC-free 1.0 M Bu₄NClO₄/CH₂Cl₂ solution and the surface coverage determined as above. The electrode was then returned to the MPC solution for a further period of potential scanning time. (In this last protocol, the electrode was not polished in between exposures to the MPC solution, so the adsorption coverages represent an accumulated quantity. Doing the no-scan experiment in this way gave results agreeing with those involving polishing the electrode in between solution exposures.)

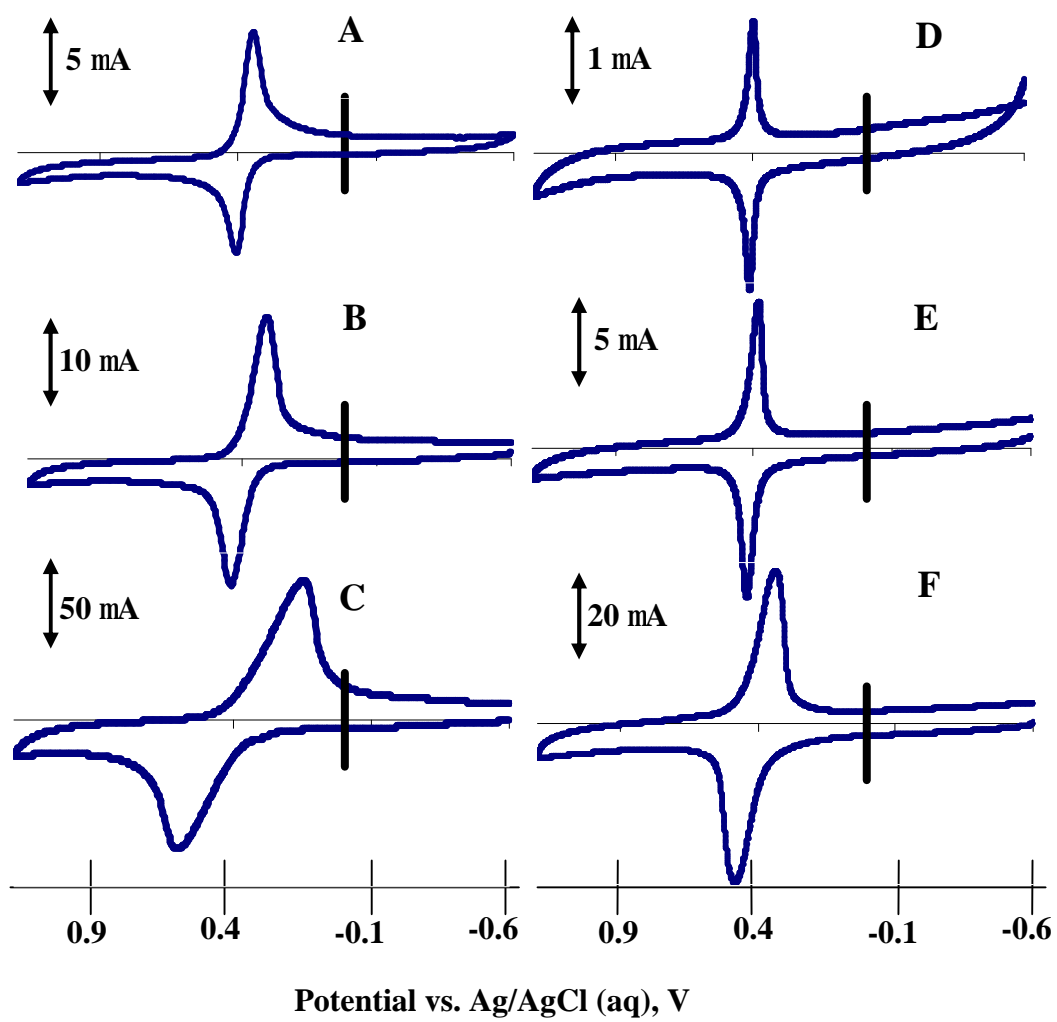
Self-assembled monolayer formation. Self-assembled monolayers (SAM) of dodecanethiolate were prepared by soaking a clean Pt electrode for 20 hours in 1 mM thiol in degassed, absolute ethanol.

4.3 Results and Discussion

Adsorption of fully ferrocenated Au₂₂₅ MPCs; Survey Experiments. Cyclic voltammetry (Figure 4.1A – C) of 0.1 mM solutions of Au₂₂₅(SC6Fc)₄₃ MPCs in 1.0 M Bu₄NPF₆/CH₂Cl₂ shows obvious product adsorption effects; the reduction peak currents are larger than the oxidation currents. The appreciable ΔE_{PEAK} values—growing larger with increasing scan rate—are substantially accountable in simulations by iR_{UNC} effects; we can identify no obvious heterogeneous electron transfer components in it.

Remarkably, after exposure to the MPC-containing electrolyte solution, the electrode can be removed, rinsed with *MPC-free* 1.0 M Bu₄NPF₆/CH₂Cl₂, and placed in *MPC-free*

Figure 4.1. Cyclic voltammetry of: Curves A-C, 0.1 mM $\text{Au}_{225}(\text{SC6Fc})_{43}$ (MPC) in 1.0 M $\text{Bu}_4\text{NPF}_6/\text{CH}_2\text{Cl}_2$ solution at potential scan rates 0.025, 0.20, and 2.0 V/s, respectively, and of Curves D-F, an adsorbed $\text{Au}_{225}(\text{SC6Fc})_{43}$ film on electrode ($\Gamma_{\text{MPC}} = 7.1 \times 10^{-12} \text{ mol/cm}^2$) formed by potential scanning in 0.1 mM MPC in 1.0 M $\text{Bu}_4\text{NPF}_6/\text{CH}_2\text{Cl}_2$ solution and transferred to an *MPC-free* 1.0 M $\text{Bu}_4\text{NPF}_6/\text{CH}_2\text{Cl}_2$ solution, at potential scan rates of 0.025, 0.20, and 2.0 V/s, respectively.

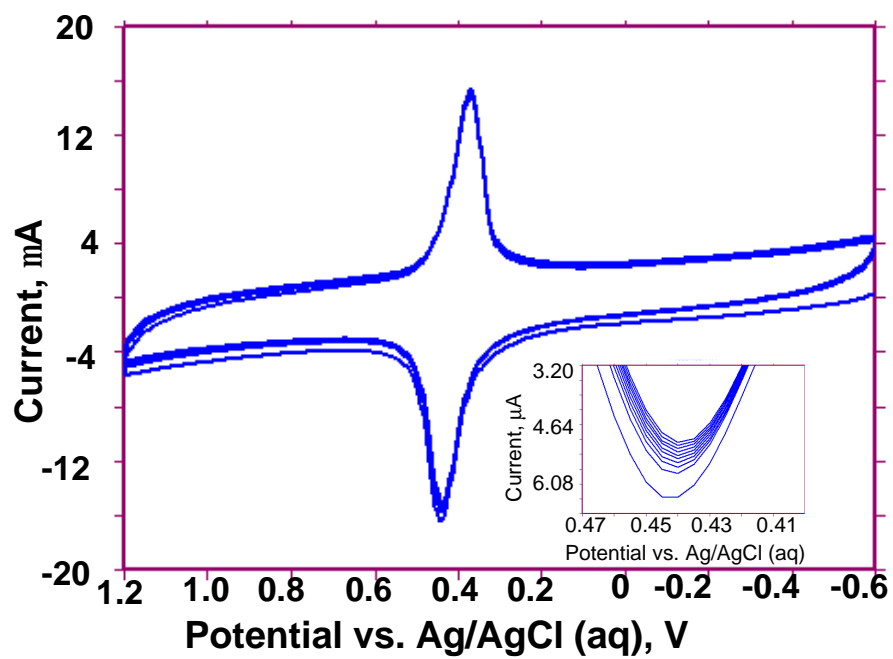


1.0 M Bu₄NPF₆/CH₂Cl₂ to produce the very stable voltammetry shown in Figure 4.1D – F. While the currents in the MPC-free electrolyte solution decay slightly upon initial potential scanning, they quickly stabilize as illustrated in Figure 4.2. The tenacity of the adsorption is illustrated by its nearly quantitative persistence after rinsing, soaking, or sonication in electrolyte-containing or electrolyte-free CH₂Cl₂; with minor variations, the same stable voltammetry (Figure 4.1D – F) was seen thereafter in MPC-free electrolyte solutions. The adsorbed MPCs could be removed by polishing the electrode.

While the adsorption of the ferrocenated Au₂₂₅ MPCs produces robust monolayers under the above circumstances, the adsorption process is shown to be sensitive to a range of factors, including the choice and concentration of electrolyte anion, the state of the Pt electrode surface, the population of ferrocene sites in the MPC monolayer, and whether the electrode's potential is scanned or not during exposure to MPC solution. Also, the adsorption does not appreciably change the Pt electrode double layer capacitance at potentials on the wings of the ferrocene wave. These features, the evidence for which follows, collectively point to an electrolyte anion-induced adsorption mechanism.

The extent of ferrocenated MPC adsorption, Γ_{MPC} , is strongly dependent on the particular electrolyte anion used, as shown by the surface coverage data in Table 4.1. The Γ_{MPC} results in Table 4.1, taken under survey experiment conditions (See Experimental) with potential scanning, are all less than the model estimate for a full MPC monolayer, *ca.* 9×10^{-12} mol/cm². This result shows that the adsorption phenomenon is not trivially a precipitated film; charges equivalent to many MPC monolayers were passed during potential scanning in the MPC-containing electrolyte solution (i.e., under the waves of voltammograms like Figure 4.1B), yet less than one monolayer is retained on the electrode. The importance of the chosen electrolyte anion is seen by comparing results

Figure 4.2. First 10 cyclic voltammograms (1.0 V/s) of an adsorbed MPC layer formed in a 0.1 mM MPC, 1.0 M Bu₄NPF₆/CH₂Cl₂ solution after transfer to an *MPC-free* 1.0 M Bu₄NPF₆/CH₂Cl₂ solution. Inset: blow-up of oxidation current peak, showing slight initial change. Thereafter, peak currents are stable and reproducible.



when the electrolyte is 1.0 M Bu_4NPF_6 , Bu_4NClO_4 , or $\text{Bu}_4\text{NC}_7\text{H}_7\text{SO}_3$. More adsorption is seen when using Bu_4NPF_6 than with Bu_4NClO_4 , but *none* occurs with $\text{Bu}_4\text{NC}_7\text{H}_7\text{SO}_3$ electrolyte. The reason(s) for differences between Γ_{MPC} in Bu_4NPF_6 and in Bu_4NClO_4 electrolytes are not clear; they may reflect differences in contact ion-pair formation constants, the counter anion size, lateral electrostatic forces, and/or differences in specific adsorption of the anion.

Table 4.1 further shows that the adsorption is promoted by larger concentrations of electrolyte; increasing Bu_4NClO_4 concentration from 0.1 M to 1.0 M in the MPC-containing solution from which adsorption is induced increases Γ_{MPC} by *ca.* 2-fold (as observed upon transfer to MPC-free solution). Adsorption from MPC-containing 0.010 M Bu_4NClO_4 was weak and non-persistent; the ferrocene currents dissipated quickly after a few potential scans in MPC-free 0.010 M $\text{Bu}_4\text{NClO}_4/\text{CH}_2\text{Cl}_2$.

Adsorption does not require scanning of potential, but its amount is enhanced by oxidizing the ferrocenated MPC to its multi-cationic state. Using the survey experiment procedure, a clean Pt electrode, either at open circuit (for three minutes) or with potential scanning (See Experimental), was exposed to a 0.05 mM MPC solution of varying concentrations of Bu_4NClO_4 in CH_2Cl_2 . The electrode was rinsed with and then immersed in the corresponding MPC-free electrolyte solution to assess the extent of adsorption by cyclic voltammetry. Table 4.2 shows that a smaller surface coverage is observed when the potential is not scanned in the MPC solution; the voltammetry of the lower coverage adsorption is however, equally persistent in MPC-free electrolyte solution.

One might infer from Table 4.2 that ferrocene sites need not be oxidized for adsorption to occur. Ferrocenated dendrimers do adsorb without oxidation.²⁵ However, a small

Table 4.1. Effect of type and concentration of supporting electrolyte on coverage Γ_{MPC} of ferrocenated MPCs adsorbed on Pt electrode from a 0.05 mM MPC solution, during survey potential scanning (between 0.2 and 1.0 V at 0.50 V/s).

Supporting Electrolyte	[Supporting Electrolyte], M	G_{MPC} , mol MPC/cm ²
Bu ₄ NC ₇ H ₇ SO ₃	1.0	no film formed
Bu ₄ NPF ₆	1.0	6.3 x 10 ⁻¹²
Bu ₄ NClO ₄	1.0	2.9 x 10 ⁻¹²
Bu ₄ NClO ₄	0.10	1.4 x 10 ⁻¹²
Bu ₄ NClO ₄	0.010	no film formed

Table 4.2. Effect of potential scanning (between 0.2 and 1.0 V at 0.50 V/s) on adsorption of ferrocenated MPCs from Bu₄NClO₄/CH₂Cl₂ solution in survey experiment.

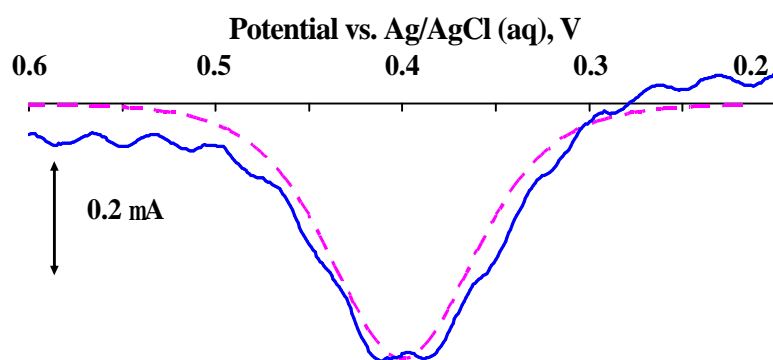
[Bu₄NClO₄],	G_{MPC} with Potential Scanning,	G_{MPC} without Potential Scanning,
M	mol MPC/cm²	mol MPC/cm²
1.0	2.9 x 10 ⁻¹²	1.0 x 10 ⁻¹²
0.10	1.4 x 10 ⁻¹²	3.0 x 10 ⁻¹³
0.010	no film formed	no film formed

fraction of the 43 ferrocene sites in the native MPC solution are oxidized, and cationic, since the 0.20 to 0.30 V rest potentials of ferrocenated MPC solutions are not far from the ferrocene formal potential (0.40 V). These oxidized ligand sites can aid adsorption by providing the bridging ion-pair interactions described in the ion-induced adsorption model discussed below.

The three minute exposure in the non-scanning experiments reported in Table 4.2 is more than sufficient (assuming $D \sim 3 \times 10^{-6} \text{ cm}^2/\text{s}$)⁵¹ to yield a complete MPC monolayer were the adsorption to occur at a diffusion-controlled rate. Also, no attempt was made to control convective effects of placing the electrode in the solution. This low coverage and the irreversibility of the adsorption suggest slow adsorption kinetics, as studied in a later section.

The ferrocenated MPC adsorption is weaker when there are fewer ferrocene sites in the MPC monolayer. Evidence for adsorption has been noticed previously^{52,53} in voltammetry (in 0.10 M $\text{Bu}_4\text{NPF}_6/\text{CH}_2\text{Cl}_2$) of hexanethiolate-coated MPCs (average 4.8 nm core dia.) where a small fraction (10-15%) of the original thiolate ligands had been replaced (by ligand exchange) by ferrocenated ligands. Those adsorbed MPCs could be removed from the Pt electrodes simply by rinsing with fresh CH_2Cl_2 solvent. This observation was probed further here, using a higher electrolyte concentration (1.0 M $\text{Bu}_4\text{NClO}_4/\text{CH}_2\text{Cl}_2$) and Au_{225} MPCs bearing *ca.* 17 ferrocene alkanethiolate ligands (see Experimental). Figure 4.3 shows the oxidation peak of the cyclic voltammogram of this adsorbed MPC in MPC-free 1.0 M $\text{Bu}_4\text{NClO}_4/\text{CH}_2\text{Cl}_2$ solution. The surface coverage is small—about 10% of that seen in Figure 4.1 and less persistent than that of fully

Figure 4.3. Oxidation peak (solid blue line) from cyclic voltammetry (2.0 V/s) of partly ferrocenated, $\text{Au}_{225}(\text{SC6})_{58}(\text{SC6Fc})_{17}$, adsorbed MPCs in 1.0 M Bu_4NClO_4 . The dashed pink line is a simulated waveshape for a reversible one-electron transfer with no lateral interactions and with E^0 the same for all ferrocenes (Equation 4). $\Gamma_{\text{MPC}} = 2 \times 10^{-13}$ mol/cm².



ferrocenated MPCs; the adsorption redox peaks gradually decreased during voltammetry in MPC-free electrolyte solution. These results show that the robust adsorption of Figure 4.1D – F is facilitated by a dense coverage of ferrocene sites on the Au MPC.

The Table 4.1 Γ_{MPC} results indicate that the adsorption of fully ferrocenated Au MPCs depends on specific adsorption of the electrolyte anion on the Pt surface in the CH_2Cl_2 medium. This was further demonstrated by coating the Pt electrode surface with a self assembled monolayer (SAM) of dodecanethiolate ligands, whereupon, in 1.0 M $\text{Bu}_4\text{NPF}_6/\text{CH}_2\text{Cl}_2$, the MPC adsorption was almost completely eliminated (Figure 4.4).

In the course of evaluating the values of Γ_{MPC} , cyclic voltammetric background currents were recorded on clean Pt electrodes in $\text{Bu}_4\text{NClO}_4/\text{CH}_2\text{Cl}_2$ and $\text{Bu}_4\text{NPF}_6/\text{CH}_2\text{Cl}_2$ solutions. Remarkably, as shown in Figure 4.5, the double-layer charging currents at potentials more positive and negative of the ferrocene wave are substantially unaffected by the ferrocenated MPC adsorption. Our prior experience with *non*-ferrocenated alkanethiolate-coated MPCs in CH_2Cl_2 solutions has been that they readily physisorb on electrodes and substantially suppress (by a factor of 2 or 3) double layer charging currents, presumably by forming a hydrocarbon-like film.⁵² The adsorbed fully ferrocenated Au_{225} MPCs are unique in our experience with MPC voltammetry in that they do not disturb the electrode double layer capacitance. An additional implication is that small electrolyte ions can facilely access the electrode surface through the interstices in the layer of relatively large (avg. overall dia. near 5 nm) adsorbed MPCs.

The persistence of $\text{Au}_{225}(\text{SC6Fc})_{43}$ MPC adsorption in MPC-free 1.0 M $\text{Bu}_4\text{NClO}_4/\text{CH}_2\text{Cl}_2$ was evaluated by cyclically scanning the potential of an adsorbate-coated electrode between 0.20 and 0.55 V at 0.20 V/s. Over 1840 scans of the ferrocene redox states provoked only a 16 % loss in MPC coverage. On the other hand, scanning to

Figure 4.4. (A) Cyclic voltammetry (blue curve, 0.20 V/s) of an adsorbed $\text{Au}_{225}(\text{SC6Fc})_{43}$ film formed on a clean Pt electrode from a 0.1 mM MPC, 1.0 M $\text{Bu}_4\text{NPF}_6/\text{CH}_2\text{Cl}_2$ solution and transferred to an *MPC-free* 1.0 M $\text{Bu}_4\text{NPF}_6/\text{CH}_2\text{Cl}_2$ solution. (B) Cyclic voltammetry (red curve, 0.20 V/s) of an identically treated Pt electrode, except that the Pt electrode had been first coated with a dodecanethiolate self-assembled monolayer (SAM).

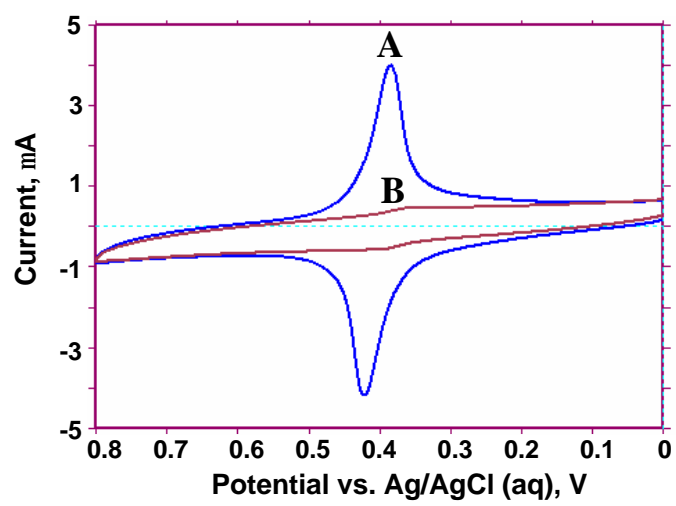


Figure 4.5. Cyclic voltammograms of an MPC-free 1.0 M Bu₄NClO₄/CH₂Cl₂ solution at (A) a bare Pt electrode and (B) a Pt electrode with an adsorbed film of Au₂₂₅(SC₆Fc)₄₃ (made in 0.1 mM MPC solution). The cyclic voltammograms were collected at 0.20 V/s.

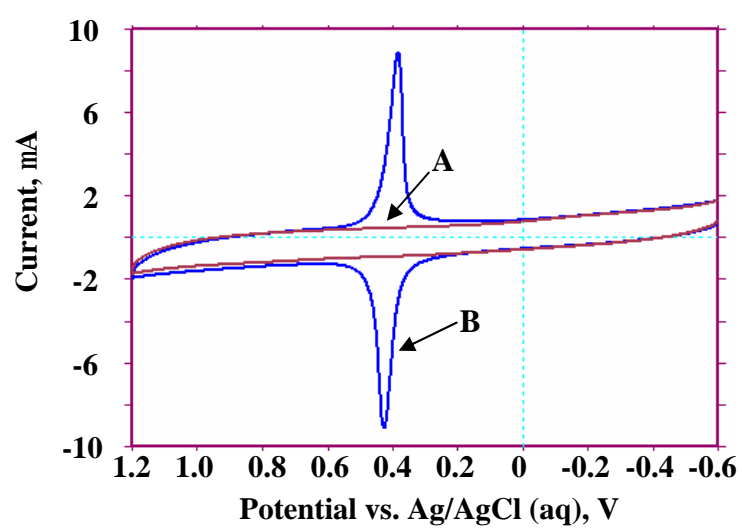
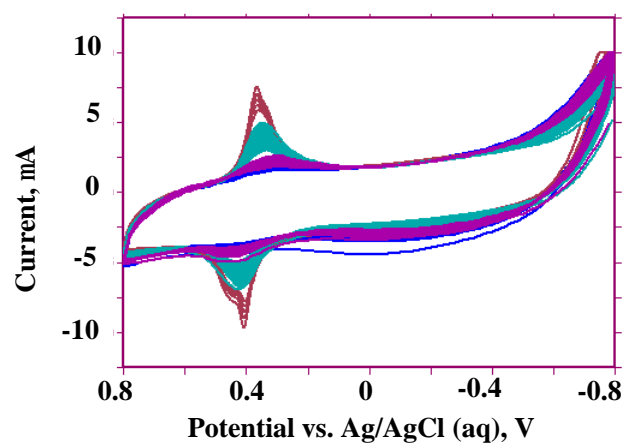


Figure 4.6. Potential cycling on 1 M Bu₄NClO₄/CH₂Cl₂ of a Pt electrode with an adsorbed film of Au₂₂₅(SC6Fc)₄₃ (made in 0.1 mM MPC/1.0 M Bu₄NClO₄/CH₂Cl₂ solution). A 90 % loss in coverage was observed over the course of 280 scans that included the negative potential region. The cycling was performed at 0.2 V/s with a Pt wire auxiliary electrode and a Ag/AgCl (aq) reference electrode.

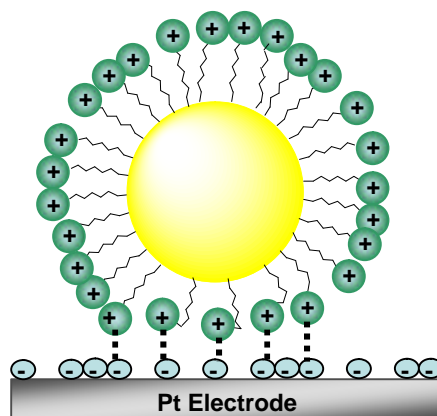


a more negative potential limit (-0.80 V) caused a rapid decrease in Γ_{MPC} as shown in Figure 4.6; after only 280 scans Γ_{MPC} decreased *ca.* 90 % of its original value. The -0.8 V limit of the voltammetric scan is more negative than the -0.1 V potential of zero charge (E_{PZC}) for Pt in an organic medium.⁵⁴ The significance of this statement is that anions should be driven off the Pt electrode at such potentials—an observation in harmony with the results in Figures 4.4 and 4.6. At the same time, we note that the MPCs are not immediately desorbed at negative potentials, which is consistent with the slow adsorption kinetics discussed later.

While further aspects of ferrocenated MPC adsorption are evaluated below, we pause here to outline how the above results suggest a mechanism for the ferrocenated MPC adsorption. We propose that its origin involves electrolyte anions in the electrochemical double layer forming bridging ion-pairs between the electrode and ferrocenium sites on the MPC, as cartooned in Figure 4.7. Ion-pairing has been detected previously between ferrocenium and ClO_4^- and PF_6^- in aqueous voltammetry of ferrocenated SAMs,¹⁹ in intervalent charge transfer of acetylene bridge biferrocene,⁵⁵ and in NMR⁵⁶ and QCM²² experiments. The present results show the importance of a) the electrolyte anions and their concentrations, b) their largely unchanged retention in the electrode double layer following MPC adsorption, c) the population of ferrocene sites on the MPC, and d) the nullifying of anion specific adsorption on the Pt surface with a hydrophobic SAM.

A likely essential aspect of Figure 4.7 is the *multiplicity* of the ion-pair bridges made possible by the concentrated ferrocenium population on the MPC. We propose that the strong persistence of the adsorption is at least partially due to entropic stabilization, akin to the well-known chelate effect.⁵⁷ Probably, ionic bridges also form laterally between

Figure 4.7. Cartoon of ion-induced adsorption, where ferrocenium cations on the MPC form ion-pair bridges with electrolyte anions specifically adsorbed to the Pt electrode. It can be imagined that the ligand shell may become deformed to form ion-pair bridges of similar dimensions. Formation of ion-pair bridges shown stabilizes successive ion-pair bridges and can cause a successive shift in Fc/Fc^+ formal potentials ($E_{j_{\max}}$ scheme, see later). It is also possible to imagine lateral ion-pair bridges between adsorbates (not shown).

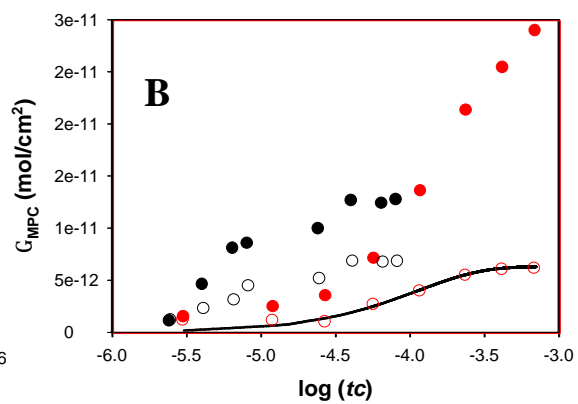
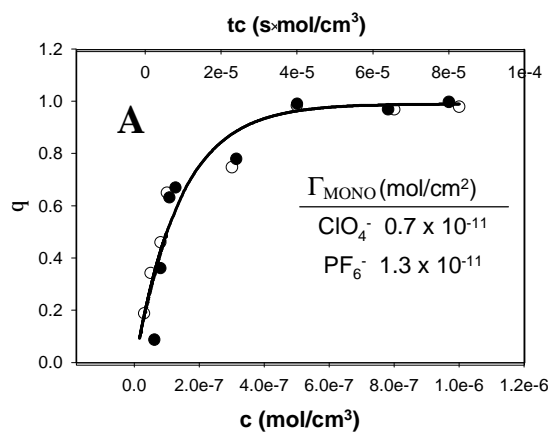


neighbor adsorbates. Such a stability picture would rely heavily on a combination of ion-pair formation constants (which increase when multiple bonds to one species are formed), the anion structure, the population of anions in the double layer, and the population of ferroceniums on the MPCs; effects all seen in the experimental behavior. There may be some consequent ordering in the monolayer, causing the overall process of producing a robust adsorption, and of desorbing it, to be kinetically slow. The model of Figure 4.7 is a nanomaterials reincarnation of the “anion-induced adsorption” model proposed many years ago by Anson, et al.⁵⁸ to account for the (much weaker) adsorption of small metal complexes on Hg electrodes.

The ferrocenated MPCs are not soluble in most electrochemically useful solvents. Less comprehensive tests in tetrahydrofuran showed adsorption effects similar to those in CH_2Cl_2 . MPCs adsorbed from 1.0 M $\text{Bu}_4\text{NPF}_6/\text{CH}_2\text{Cl}_2$ solutions could be rinsed with MPC-free 1.0 M $\text{Bu}_4\text{NPF}_6/\text{CH}_2\text{Cl}_2$ and placed in 1.0 M $\text{Bu}_4\text{NPF}_6/\text{CH}_3\text{CN}$ where stable voltammetry similar to that discussed above could be observed (results not shown).

Adsorption Kinetics. As noted above, the apparently slow adsorption of the fully ferrocenated Au MPCs prompted a study of adsorption kinetics. Three different protocols (See Experimental section) were used in assessing adsorption kinetics. The *fixed-time* protocol involved exposure, while scanning the electrode potential for a uniform time, of a clean Pt electrode to 1.0 M Bu_4NClO_4 or 1.0 M $\text{Bu}_4\text{NPF}_6/\text{CH}_2\text{Cl}_2$ solutions containing varied concentrations of ferrocenated MPCs. In a second, *no-scan* protocol, the Pt electrode was exposed at open circuit to a 0.05 mM MPC solution in 1.0 M $\text{Bu}_4\text{NClO}_4/\text{CH}_2\text{Cl}_2$ for varying periods of time. A third, *scanning* kinetics protocol, involved cyclically scanning the electrode potential in a 0.05 MPC/1.0 M

Figure 4.8. Panel A: Fractional coverages (θ) of MPCs measured in *fixed-time* experiments at different MPC concentrations (lower horizontal axis) in 1.0 M Bu₄NClO₄ (open black circles, $\Gamma_{\text{MONO}} = 0.7 \times 10^{-11}$ mol/cm²) and 1.0 M Bu₄NPF₆ (filled black circles, $\Gamma_{\text{MONO}} = 1.3 \times 10^{-11}$ mol/cm²) electrolytes. The upper horizontal axis is normalized MPC concentration*time (tc), where $t = 80$ s for all data points. Panel B: Coverage of MPCs (Γ_{MPC}) measured as a function of $\log(tc)$ in *no-scan* (open red circles), *scanning* (filled red circles), and *fixed-time* (ClO₄⁻ open black circles, PF₆⁻ filled black circles) protocol experiments. *No-scan and scanning* experimental protocols used a fixed (0.05 mM) MPC concentration in 1.0 M Bu₄NClO₄/CH₂Cl₂. The solid lines in both Panels are fits to the first-order rate expression, Equation 3, for the rate constants displayed in Table 4.3. No fit was performed on the *scanning* protocol as it leads to multilayers and does not appear to attain a saturation coverage.



Bu₄NClO₄/CH₂Cl₂ solution through the ferrocene potential for varying periods of time. There were thus four sets of kinetic results.

The results of the four experiments are displayed in Figure 4.8. Panel A displays the data of the *fixed-time* experimental protocol for the two electrolyte systems as plots of fractional coverage, $\theta = \Gamma_{\text{MPC}}/\Gamma_{\text{MONO}}$, where Γ_{MONO} is the apparent saturation monolayer coverage, versus MPC concentration, c (lower x -axis), and versus time multiplied by concentration, tc (upper x -axis), where the exposure time was constant at 80 s. Panel B displays the MPC coverages, Γ_{MPC} , for all four sets of data (*fixed-time*, *no-scan*, and *scanning* protocols) plotted versus $\log [tc]$ (in which MPC concentrations in the *scanning* and *no-scan* protocols were constant at 0.05 mM). Apparent adsorption rate constants can be derived from these experimental data using the Langmuirian rate equation

$$\frac{dq}{dt} = kc(1 - q) \quad (2)$$

where k is the first-order adsorption rate constant, t is the time the electrode spent in the MPC solution, and c is the MPC concentration (mol/cm³). The solid curves shown in Figure 4.8 are fits to this first-order rate law where Equation 2 was rearranged to form

$$q = 1 - \exp(-kct) \quad (3)$$

The corresponding rate constants are listed in Table 4.3. This first-order rate law assumes that the Langmuir isotherm applies with the concomitant presumption that there is a maximum monolayer surface coverage, that the adsorption coefficient is so large that the adsorption is effectively irreversible, that the kinetics for adsorption are slow, and that there is no concentration polarization of the MPC near the electrode.

Figure 4.8A presents the fixed-time results, where Γ_{MPC} adsorption occurred from varied MPC concentrations for a fixed time. It is apparent that although Γ_{MONO} is

Table 4.3. Rate constants for MPC adsorption derived from fixed-time and no-scan experimental protocols. G_{MPC} was measured as a function of MPC concentration in fixed-time experiments and as a function of time in no-scan protocol. (All scans were taken between 0 and 0.8 V/s.)

Experimental Protocol		$k, \text{cm}^3/\text{mol}\cdot\text{s}$
No-scan	(1.0 M $\text{Bu}_4\text{NClO}_4/\text{CH}_2\text{Cl}_2$)	9×10^3
Fixed-time	(1.0 M $\text{Bu}_4\text{NClO}_4/\text{CH}_2\text{Cl}_2$)	9×10^4
Fixed-time	(1.0 M $\text{Bu}_4\text{NPF}_6/\text{CH}_2\text{Cl}_2$)	9×10^4

somewhat larger in 1.0 M Bu₄NPF₆/CH₂Cl₂ ($\Gamma_{\text{MONO}} = 1.3 \times 10^{-11}$ mol/cm²) than in 1.0 M Bu₄NClO₄/CH₂Cl₂ ($\Gamma_{\text{MONO}} = 0.7 \times 10^{-11}$ mol/cm²), the rates of MPC adsorption are identical in the two electrolyte media. Calculated from Equation 3, a single value of k (Table 4.3) serves to fit the results in both media.

Figure 4.8B plots all four sets of data on the same graph so as to compare them. The no-scan results are well-fit (solid line) by Equation 3 and produce an adsorption rate constant (Table 4.3) that is *ca.* 10-fold slower than seen in the fixed-time experiment (Figure 4.8A). This rate difference is consistent with the results of Table 4.2 and the model of Figure 4.7, and we believe it reflects the influence of potential scanning in the latter (fixed-time) experiment, provoking a more rapid accumulation of adsorbed nanoparticles by generating larger populations of ferrocenium sites.

The results for the scanning protocol in Figure 4.8B reveal an additional aspect of the ferrocenated MPC adsorption, namely that adsorbed multilayers can form under the combined impetus of long exposure times (over 3 hours) and potential scanning. The largest Γ_{MPC} attained was 2.9×10^{-11} mol/cm², which is equivalent to about 3 monolayers, and the adsorbed MPCs do not appear to have reached a saturation point. From the plot, it is evident that as long as $\Gamma_{\text{MPC}} < \Gamma_{\text{MONO}}$, the rate of accumulation of Γ_{MPC} is roughly similar to that seen in the other experimental protocols, and presumably occurs with a similar rate constant. However, when $\Gamma_{\text{MPC}} > \Gamma_{\text{MONO}}$, the adsorption rate profile changes. Because of the increased complexity of multilayer formation, we did not attempt to extract a rate constant from the scanning protocol data.

The voltammetry of the adsorbed ferrocenated MPCs throughout the preceding experiments continued to exhibit quite narrow peaks, as illustrated in Figure 4.1D, at all

monolayer or sub-monolayer coverages. When multilayers were formed in the scanning kinetics protocol (Figure 4.8B), however, the current peaks broadened by a factor of two in E_{FWHM} (although remained narrower than the ideal 90.6 mV). Additionally, the behavior illustrated in Figure 4.2—where a small loss of MPC coverage occurred upon preliminary potential scanning after transfer to MPC-free solution—was seen in all experiments involving sub-monolayer adsorption, but not when MPC multilayers formed. There is apparently no “loosely adsorbed” component of a multilayer film.

Although the kinetic slowness of the MPC adsorption is striking, we have only speculation regarding the underlying reason(s). The adsorption kinetics is much slower than the realm of diffusion-controlled adsorption, as was noted above. Some kind of slow surface reaction⁵⁹ must be involved; examples mentioned in a recent discussion⁵⁹ include surface precipitation, surface site bonding energy heterogeneity, and formation of ordered surface structures. The conversion of the MPC to the ferrocenium form—which is not very soluble in CH_2Cl_2 and the specific adsorption of and ion-pair bridging by presumably multiple electrolyte anions must play important roles in the slow surface reaction(s). We also speculate that the MPCs may slowly generate ordered domains on the Pt electrode, and it is solely these slowly-formed domains that survive the transfer to MPC-free electrolyte.

Voltammetric Waveshape Analysis. We turn lastly to the narrowed voltammetric peaks noted above for adsorbed ferrocenated MPCs (Figure 4.1D, $E_{\text{FWHM}} = 35$ mV). A one-electron reaction of an ideal adsorbed layer has in contrast a voltammetric $E_{\text{FWHM}} = 90.6$ mV and a waveshape following the equation^{14,60-62}

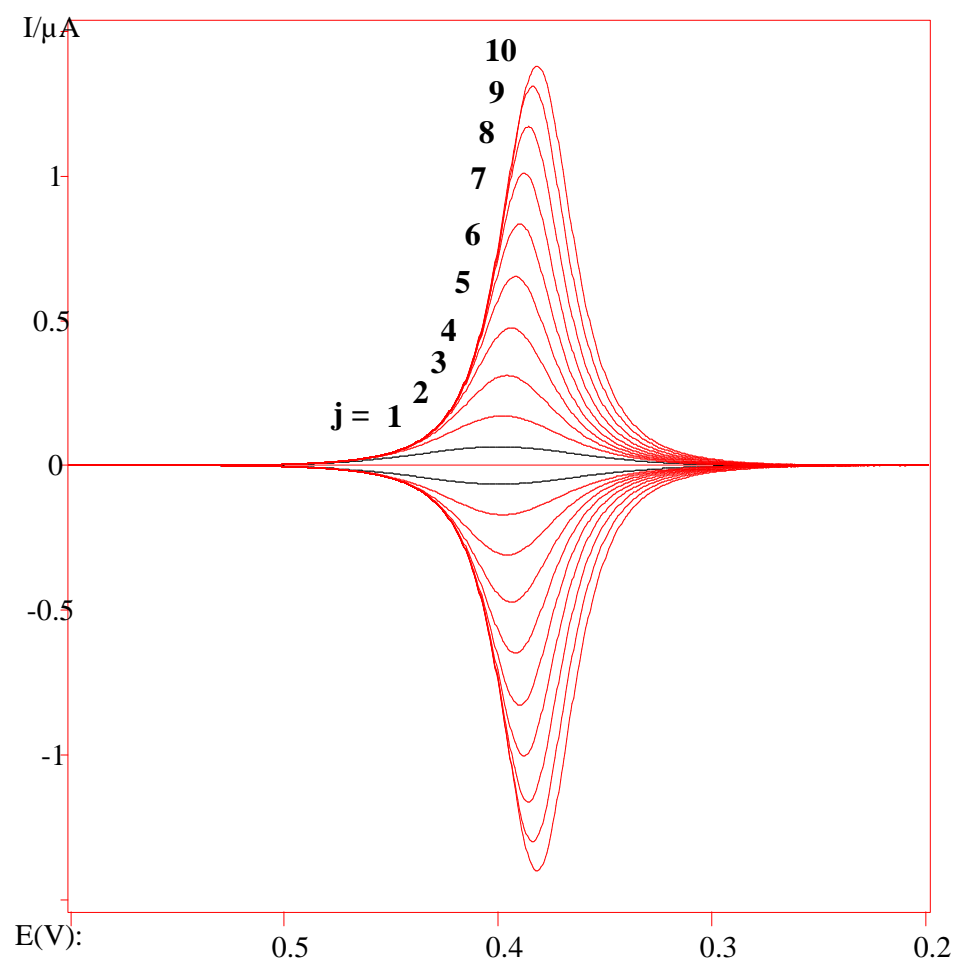
$$i = -\frac{bF^2\Gamma_T v}{RT} \frac{\exp\left[\frac{F}{RT}(E - E^{0'})\right]}{\left(1 + \exp\left[\frac{F}{RT}(E - E^{0'})\right]\right)^2} \quad (4)$$

where b is the number of ferrocenes per MPC, Γ_T is adsorbed MPC coverage ($\Gamma_{\text{MPC,Red}} + \Gamma_{\text{MPC,Ox}}$), and v is potential scan rate. Equation 4 assumes that all redox sites react independently, have the same formal potential, $E^{0'}$, and have adsorbate activities proportional to Γ_{Red} and Γ_{Ox} . Figure 4.1D shows that one or more of these assumptions fail for the adsorbed ferrocenated MPCs.

We offer two alternative interpretations of the narrow voltammetric waveshape based on failures of the above assumptions. The first considers that ferrocene formal potentials are not all equal, but instead $E^{0'}$ gradually becomes less positive (by increments $\Delta E^{0'}$) as successive ferrocene sites become oxidized. The shift is promoted by the successive stabilization of the adsorbed ferrocene MPC ligand through ion-pair bridging between ferrocenium sites, electrolyte anions, and the electrode (and possibly, laterally between MPCs). For example, the cartoon in Figure 4.7 shows five ion-pair bridges; as each of the five ferrocenes was oxidized, formation of an ion-pair bridge stabilizes the adsorbed MPC, so that the next ferrocene site can be oxidized at a slightly less positive $E^{0'}$. The scheme comprises j_{max} sequential reversible electron transfers which we will refer to as the $E_{j_{\text{max}}}$ scheme. We assume that $E_j^{0'} - E_{j-1}^{0'}$ is negative and constant.

In the $E_{j_{\text{max}}}$ scheme, each sequential electrochemical reaction is accompanied by formation of ion-pair bridges (IB) between the electrode, counter anion, and individual ferroceniums. The number of steps that involve $\Delta E^{0'}$ changes (j) is undoubtedly $< ca. 43$ and may involve only the ferrocene sites closest to the electrode (Figure 4.7). The reverse

Figure 4.9. Simulations of $E_{j_{\max}}$ scheme voltammetry for sequential electron transfer reactions of 10 ferrocene ligands per adsorbed MPC, where each successively reacting ferrocene's formal potential is incrementally shifted by $\Delta E^{0'} = -4$ mV. The numbers by the curves are values of j ; i.e., $j = 3$ is the voltammetry predicted for reaction of the first three ferrocenes only and $j = 10$ for overall current after the tenth ferrocene has reacted.



occurs during reduction. To our knowledge, this type of effect has not been previously considered. Statistical aspects of many-electron transfer reactions of redox polymers^{9,26} have been presented, but that theory does not predict peak-narrowing, and the statistical shifts predicted are opposite to those proposed here.

The voltammetric peak-narrowing of adsorbed MPCs with the $E_{j_{\max}}$ scheme is illustrated by the simulations in Figure 4.9 for $\Delta E^{0'} = -4$ mV and $j_{\max} = 10$. (Curve 10 is thus an overall 10 electron wave.) The extent of peak narrowing for $j_{\max} = 10$ is larger for smaller $\Delta E^{0'}$, as shown by Figure 4.10. Our choice of $j_{\max} = 10$ and $\Delta E^{0'} = -4$ mV is only illustrative of the peak narrowing effect, but in Figure 4.11 these parameters do yield a good fit to the observed adsorbed MPC voltammetry in both 1.0 M Bu₄NPF₆/CH₂Cl₂ and 1.0 M Bu₄NClO₄/CH₂Cl₂ solutions (Curves B, D). Other combinations of j and $\Delta E^{0'}$ may however fit the data equally well; we do not propose that the Figure 4.11 comparisons are unique. The main point is that a model based on progressive formation of ion-pair bridges, causing formal potential changes, can well-represent the peak narrowing experimental results. It is important to note that the model implicitly assumes that surface activities of all species are proportional to their surface concentrations.

A second analysis of the narrowed MPC voltammetric waveshapes is based on a known surface activity model invoking attractive lateral interactions between adsorbed nanoparticles, so that activities of the adsorbates do not scale linearly with their surface coverages. There have been several theoretical analyses^{9,14,15,63-68} of how activity effects change surface waveshapes using a quantity-dependent activity, a parameterized interaction between *Ox* and *Red* sites, or other theoretical models.⁶² For a one-electron

Figure 4.10. Simulations of a 10 e^- transfer with 10 successive $E^{o'}$ values, each less positive (by $\Delta E^{o'}$) than the previous one ($E_{j_{\max}}$ scheme); each simulation has a different $\Delta E^{o'}$, with the numbers by the curve representing the values of $\Delta E^{o'}$ ranging from -1 mV (the sharpest peak) to -11 mV (the broadest peak).

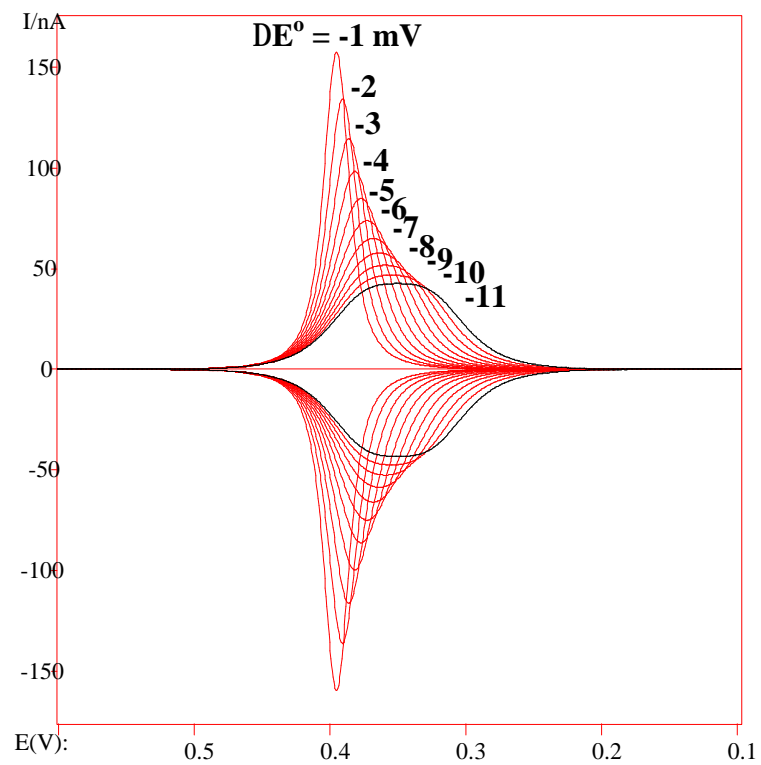
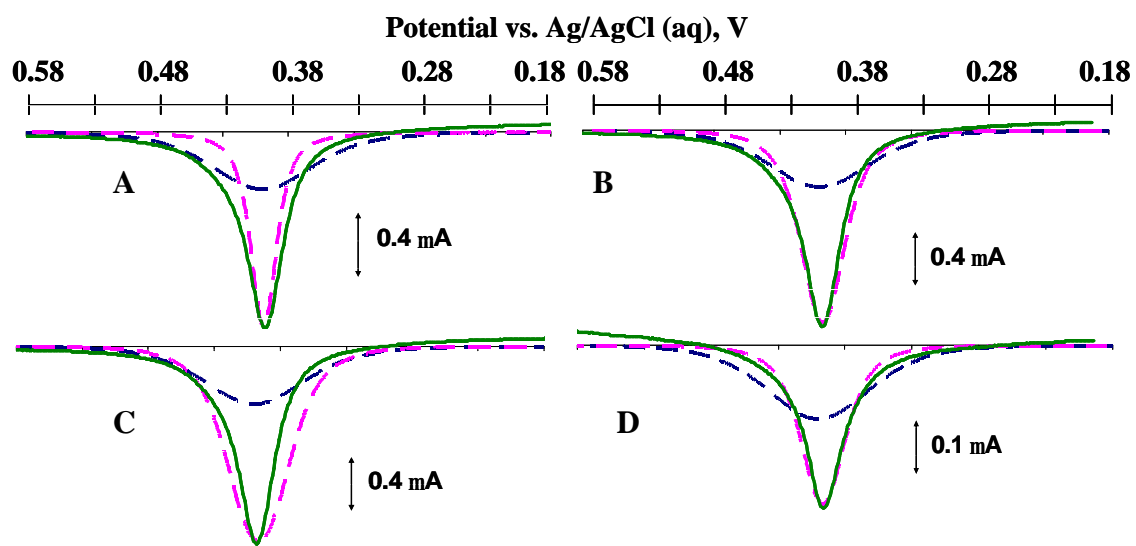


Figure 4.11. Simulations of the oxidative peak of a one electron transfer of an ideal adsorbed ferrocene monolayer (blue dashed line) and $E_{j_{\max}}$ scheme with $j = 10$ and varied $\Delta E^{\circ'}$ (pink dashed line), compared to experimental voltammetry (green solid line, 0.025 V/s) of ferrocenated MPCs adsorbed from a 0.1 mM MPC solution in 1.0 M $\text{Bu}_4\text{NPF}_6/\text{CH}_2\text{Cl}_2$ (Curves A – C) and 1.0 M $\text{Bu}_4\text{NClO}_4/\text{CH}_2\text{Cl}_2$ (Curve D). Varied $\Delta E^{\circ'}$ fits (blue dashed line) for Curve A has $\Delta E^{\circ'} = -1$ mV (FWHM = 23 mV), for Curve B and D $\Delta E^{\circ'} = -4$ mV (FWHM = 35 mV), and for Curve C $\Delta E^{\circ'} = -6$ mV (FWHM = 53 mV); the best fit for both electrolytes is at $\Delta E^{\circ'} = -4$ mV. To compare the curves, all are normalized to the experimental $E^{\circ'}$ and peak current.



reaction, representing interaction parameters between *Ox* and *Red* as r_{Ox} and r_{Red} yields the equation¹⁴

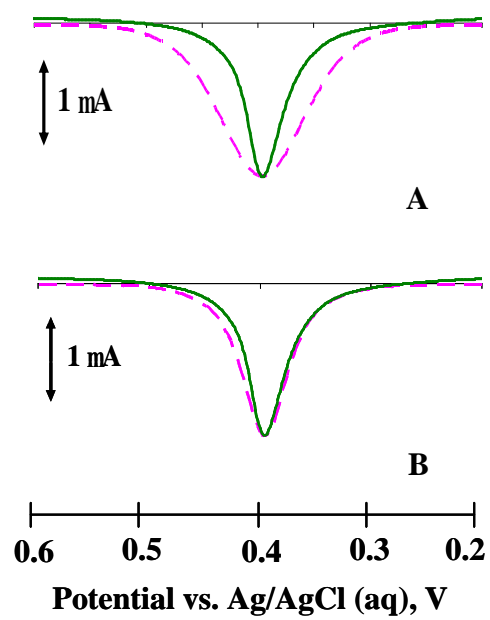
$$i = -\frac{bF^2 G_T n f (1-f)}{RT[1-fG_T(r_{\text{Ox}} + r_{\text{Red}})(1-f)]} \quad (5)$$

where f is the fraction of the molecules on the surface in their oxidized form. For $r_{\text{Ox}} = r_{\text{Red}} = 0$ (i.e., no interactions), Equation 5 reduces to Equation 4. The interaction parameter is signed positive and negative for attractive and repulsive interactions, respectively; attractive interactions in Equation 5 lead to voltammetric peak narrowing.

The experimental data seems to support the idea that the adsorbed layers of ferrocenated MPCs are stabilized by lateral interactions, possibly involving the counter ions, and it is also likely that the activities of the ferrocene moieties are changing during the redox process. Figure 4.12 compares Equations 4 and 5 (dashed pink lines, Curves A, B, respectively) to MPC adsorption data (green solid lines) taken in a survey experiment in 1.0 M $\text{Bu}_4\text{NClO}_4/\text{CH}_2\text{Cl}_2$ solution. Curve A shows that the experimental oxidative peak is substantially more narrow than predicted by Equation 4, while Curve B shows an excellent fit for Equation 5 using (quite large) attractive interaction parameters $r_{\text{Ox}} = r_{\text{Red}} = 2 \times 10^{11} \text{ mol}^{-1}\text{cm}^2$. Although not shown, the fits for Equations 4 and 5 to the experimental oxidation peak of ferrocenated MPCs in 1.0 M $\text{Bu}_4\text{NPF}_6/\text{CH}_2\text{Cl}_2$ gave identical results as shown in Figure 4.12 but required slightly larger interaction parameters: $r_{\text{Ox}} = r_{\text{Red}} = 6 \times 10^{11} \text{ mol}^{-1}\text{cm}^2$. These comparisons show that an activity-based model can also be used to represent the voltammetric peak narrowing.

The comparisons of experimental results to theory in Figures 4.11 and 4.12 are based on two rather different models, both of which are physically plausible. The $E_{j_{\text{max}}}$ scheme is physically appealing because it can be related to the chemical binding interactions

Figure 4.12. Ferrocene oxidation peak in experimental voltammetry (green solid line, 0.10 V/s) of ferrocenated MPCs adsorbed from a 0.1 mM MPC solution in 1.0 M $\text{Bu}_4\text{NClO}_4/\text{CH}_2\text{Cl}_2$ compared to waveshapes (pink dashed lines) predicted from Equations 4 (Curve A) and 5 (Curve B for $r_{\text{Ox}} = r_{\text{Red}} = 2 \times 10^{11} \text{ mol}^{-1}\text{cm}^2$). Experimental data collected from 1.0 M $\text{Bu}_4\text{PF}_6/\text{CH}_2\text{Cl}_2$ (not shown) gave a similarly good fit to Equation 5, using $r_{\text{Ox}} = r_{\text{Red}} = 6 \times 10^{11} \text{ mol}^{-1}\text{cm}^2$. Predicted curves are normalized to the experimental E^0 and peak current.



proposed in the model for ion-induced adsorption (Figure 4.7). Its weakness is the presumption of surface activity-concentration proportionality, and it is possible that the peak narrowing may reflect concurrent contributions from both of the above explanations.

Notably, when the number of ferrocene sites is diluted on the monolayer, as for the mixed monolayer $\text{Au}_{225}(\text{SC6})_{58}(\text{SC6Fc})_{17}$ MPC in Figure 4.3, the peak narrowing is not observed. Instead, the experimental waveshape shown in Figure 4.3 (blue solid line) is well represented by the ideal electroactive monolayer Equation 4 fit (pink dashed line). This result shows that peak narrowing is provoked by close proximity of the ferrocene/ferrocenium sites to each other in the MPC ligand shell.

It is worth in closing to contrast the fully ferrocenated MPC adsorption described here to other examples of adsorption of multi-ferrocenated entities. A close example is that of Abruña, et al.²⁵ who observed significant adsorption, from 0.10 M $\text{Bu}_4\text{NClO}_4/\text{CH}_2\text{Cl}_2$, of diaminobutane-based poly(propylene imine) dendrimers bearing 8, 32, and 64 peripheral ferrocenyl moieties. The adsorption followed a Langmuir isotherm and was strong, being observable from sub-micromolar concentrations, however, the voltammetric peak shapes were normal. A more distant comparison can be made with adsorption of poly(vinylferrocene) (PVF).^{15,26-29} These multilayer films showed interesting complexities, including narrowed peak shapes, however they were inferred to be caused by different environments of oxidized (and reduced) sites within the film and conversions between them.

4.4 Acknowledgments.

This research was supported by grants from the National Science Foundation and Office of Naval Research. Contributions from Dr. Ramjee Balasubramanian from the University

of North Carolina and Dr. Stephen Feldberg from the Brookhaven National Lab are also acknowledged.

4.5 References

- (1) Wolfe, R. L.; Balasubramanian, R.; Tracy, J. B.; Murray, R. W. *Langmuir* **2007**, *23*, 2247-2254.
- (2) Chidsey, C. E. D.; Murray, R. W. *Science* **1986**, *231*, 25-31.
- (3) Murray, R. W.; Ewing, A. G.; Durst, R. A. *Anal. Chem.* **1987**, *59*, A379-&.
- (4) Wrighton, M. S. *Science* **1986**, *231*, 32-37.
- (5) Faulkner, L. R. *Chem. Eng. News* **1984**, *62*, 28-&.
- (6) Murray, R. W. *Electroanalytical Chemistry* **1984**, *13*, 191-368.
- (7) Murray, R. W. *Accounts of Chemical Research* **1980**, *13*, 135-141.
- (8) Bard, A. J. *J. Chem. Educ.* **1983**, *60*, 302-304.
- (9) Bard, A. J.; Faulkner, L. R. *Electrochemical Methods: Fundamentals and Applications*; Second ed.; Wiley: New York, 2001.
- (10) Li, J. H.; Schuler, K.; Creager, S. E. *J. Electrochem. Soc.* **2000**, *147*, 4584-4588.
- (11) Brevnov, D. A.; Finklea, H. O. *J. Electrochem. Soc.* **2000**, *147*, 3461-3466.
- (12) Creager, S. E.; Wooster, T. T. *Anal. Chem.* **1998**, *70*, 4257-4263.
- (13) Matsuda, H.; Aoki, K.; Tokuda, K. *J. Electroanal. Chem.* **1987**, *217*, 15-32.
- (14) Brown, A. P.; Anson, F. C. *Anal. Chem.* **1977**, *49*, 1589-1595.
- (15) Pearce, P. J.; Bard, A. J. *J. Electroanal. Chem.* **1980**, *114*, 89-115.
- (16) Chidsey, C. E. D.; Bertozzi, C. R.; Putvinski, T. M.; Majsce, A. M. *J. Am. Chem. Soc.* **1990**, *112*, 4301-4306.
- (17) Albery, W. J.; Boutelle, M. G.; Colby, P. J.; Hillman, A. R. *J. Electroanal. Chem.* **1982**, *133*, 135-145.
- (18) Gerischer, H.; Scherson, D. A. *J. Electroanal. Chem.* **1985**, *188*, 33-38.
- (19) Rowe, G. K.; Creager, S. E. *Langmuir* **1991**, *7*, 2307-2312.
- (20) Acevedo, D.; Abruna, H. D. *J. Phys. Chem.* **1991**, *95*, 9590-9594.
- (21) Smith, C. P.; White, H. S. *Anal. Chem.* **1992**, *64*, 2398-2405.

- (22) Rivera, I. M.; Cabrera, C. R. *J. Electrochem. Soc.* **1993**, *140*, L36-L38.
- (23) Daschbach, J.; Blackwood, D.; Pons, J. W.; Pons, S. *J. Electroanal. Chem.* **1987**, *237*, 269-273.
- (24) Bond, A. M.; McLennan, E. A.; Stojanovic, R. S.; Thomas, F. G. *Anal. Chem.* **1987**, *59*, 2853-2860.
- (25) Takada, K.; Diaz, D. J.; Abruna, H. D.; Cuadrado, I.; Casado, C.; Alonso, B.; Moran, M.; Losada, J. *J. Am. Chem. Soc.* **1997**, *119*, 10763-10773.
- (26) Flanagan, J. B.; Margel, S.; Bard, A. J.; Anson, F. C. *J. Am. Chem. Soc.* **1978**, *100*, 4248-4253.
- (27) Pearce, P. J.; Bard, A. J. *J. Electroanal. Chem.* **1980**, *112*, 97-115.
- (28) Pearce, P. J.; Bard, A. J. *J. Electroanal. Chem.* **1980**, *108*, 121-125.
- (29) Merz, A.; Bard, A. J. *J. Am. Chem. Soc.* **1978**, *100*, 3222-3223.
- (30) Yamada, M.; Nishihara, H. *ChemPhysChem* **2004**, *5*, 555-559.
- (31) Yamada, M.; Nishihara, H. *C. R. Chim.* **2003**, *6*, 919-934.
- (32) Yamada, M.; Nishihara, H. *Langmuir* **2003**, *19*, 8050-8056.
- (33) Yamada, M.; Tadera, T.; Kubo, K.; Nishihara, H. *J. Phys. Chem. B* **2003**, *107*, 3703-3711.
- (34) Yamada, M.; Quiros, I.; Mizutani, J.; Kubo, K.; Nishihara, H. *Phys. Chem. Chem. Phys.* **2001**, *3*, 3377-3381.
- (35) Men, Y.; Kubo, K.; Kurihara, M.; Nishihara, H. *Phys. Chem. Chem. Phys.* **2001**, *3*, 3427-3430.
- (36) Lenhard, J. R.; Murray, R. W. *J. Am. Chem. Soc.* **1978**, *100*, 7870-7875.
- (37) Chen, S. W.; Ingram, R. S.; Hostetler, M. J.; Pietron, J. J.; Murray, R. W.; Schaaff, T. G.; Khoury, J. T.; Alvarez, M. M.; Whetten, R. L. *Science* **1998**, *280*, 2098-2101.
- (38) Hicks, J. F.; Templeton, A. C.; Chen, S. W.; Sheran, K. M.; Jasti, R.; Murray, R. W.; Debord, J.; Schaaf, T. G.; Whetten, R. L. *Anal. Chem.* **1999**, *71*, 3703-3711.
- (39) Ingram, R. S.; Hostetler, M. J.; Murray, R. W.; Schaaff, T. G.; Khoury, J. T.; Whetten, R. L.; Bigioni, T. P.; Guthrie, D. K.; First, P. N. *J. Am. Chem. Soc.* **1997**, *119*, 9279-9280.

- (40) Chen, S. W.; Murray, R. W.; Feldberg, S. W. *J. Phys. Chem. B* **1998**, *102*, 9898-9907.
- (41) Wolfe, R. L.; Murray, R. W. *Anal. Chem.* **2006**, *78*, 1167-1173.
- (42) Kim, Y. G.; Garcia-Martinez, J. C.; Crooks, R. M. *Langmuir* **2005**, *21*, 5485-5491.
- (43) Balasubramanian, R.; Guo, R.; Mills, A. J.; Murray, R. W. *J. Am. Chem. Soc.* **2005**, *127*, 8126-8132.
- (44) Chaki, N. K.; Kakade, B.; Sharma, J.; Mahima, S.; Vijayamohanan, K. P.; Haram, S. K. *J. Appl. Phys.* **2004**, *96*, 5032-5036.
- (45) Chaki, N. K.; Singh, P.; Dharmadhikari, C. V.; Vijayamohanan, K. P. *Langmuir* **2004**, *20*, 10208-10217.
- (46) Quinn, B. M.; Liljeroth, P.; Ruiz, V.; Laaksonen, T.; Kontturi, K. *J. Am. Chem. Soc.* **2003**, *125*, 6644-6645.
- (47) Yang, Y.; Pradhan, S.; Chen, S. *Journal of American Chemical Society* **2004**, *126*, 76-77.
- (48) Jimenez, V. L.; Georganopoulou, D. G.; White, R. J.; Harper, A. S.; Mills, A. J.; Lee, D. I.; Murray, R. W. *Langmuir* **2004**, *20*, 6864-6870.
- (49) Brauer, G. *Handbook of Preparative Inorganic Chemistry*; Academic Press: New York, 1965.
- (50) Yu, C. J.; Wang, H.; Wan, Y. J.; Yowanto, H.; Kim, J. C.; Donilon, L. H.; Tao, C. L.; Strong, M.; Chong, Y. C. *J. Org. Chem.* **2001**, *66*, 2937-2942.
- (51) Green, S. J.; Pietron, J. J.; Stokes, J. J.; Hostetler, M. J.; Vu, H.; Wuelfing, W. P.; Murray, R. W. *Langmuir* **1998**, *14*, 5612-5619.
- (52) Miles, D. T.; Murray, R. W. *Anal. Chem.* **2003**, *75*, 1251-1257.
- (53) Green, S. J.; Stokes, J. J.; Hostetler, M. J.; Pietron, J.; Murray, R. W. *J. Phys. Chem. B* **1997**, *101*, 2663-2668.
- (54) Marinkovic, N. S.; Hecht, M.; Loring, J. S.; Fawcett, W. R. *Electrochim. Acta* **1996**, *41*, 641-651 *Experimental conditions were 100 mM TEAP/ACN on Pt(100) and Pt(111) single crystals.*
- (55) Hupp, J. T. *Inorg. Chem.* **1990**, *29*, 5010-5012.
- (56) Yang, E. S.; Chan, M. S.; Wahl, A. C. *J. Phys. Chem.* **1980**, *84*, 3094-3099.

- (57) Schwarzenbach, G. *Helv. Chim. Acta* **1952**, 35, 2344-2359.
- (58) Anson, F. C.; Barclay, D. J. *Anal. Chem.* **1968**, 40, 1791-&.
- (59) Zhang, J. S.; Stanforth, R. *Langmuir* **2005**, 21, 2895-2901.
- (60) Laitinen, H. A.; Vincent, C. A.; Bednarsk.Tm *J. Electrochem. Soc.* **1968**, 115, 1024-1028.
- (61) Laviron, E. *Bulletin De La Societe Chimique De France* **1967**, 3717-3723.
- (62) Murray, R. W. *Molecular Design of Electrode Surfaces*; Wiley: New York, 1992.
- (63) Chidsey, C. E. D.; Murray, R. W. *J. Phys. Chem.* **1986**, 90, 1479-1484.
- (64) Coleman, S. T.; McKinnon, W. R.; Dahn, J. R. *Physical Review B* **1984**, 29, 4147-4149.
- (65) Ikeda, T.; Leidner, C. R.; Murray, R. W. *J. Electroanal. Chem.* **1982**, 138, 343-365.
- (66) Laviron, E. *J. Electroanal. Chem.* **1981**, 122, 37-44.
- (67) Ellis, D.; Eckhoff, M.; Neff, V. D. *J. Phys. Chem.* **1981**, 85, 1225-1231.
- (68) Angersteinkozłowska, H.; Klinger, J.; Conway, B. E. *J. Electroanal. Chem.* **1977**, 75, 45-60.

CHAPTER V

REDOX FUNCTIONALIZED MONOLAYER PROTECTED GOLD CLUSTERS AS ELECTROCHEMICAL CAPACITORS

5.1 Introduction

Currently much investigation is focused on electrochemical capacitors, or supercapacitors, owing to their widespread use as storage devices complementary to conventional batteries in a variety of applications requiring large amounts of power.^{1,2} New applications for supercapacitors are constantly emerging including portable electronics, power quality devices, and low-emission hybrid cars, buses, and trucks.³ Supercapacitors generate electrical energy via the formation and release of an electrochemical double layer comprising of electrolyte ions at the electrode/electrolyte surface,³ and they are generally composed of high surface area materials such as carbon,^{4,5} conductive polymers,^{6,7} and noble⁸⁻¹⁰ and transition metal-oxides.¹¹⁻²⁸ Metal oxide particles supported on porous carbon electrodes^{11,13,29-33} have become increasingly popular owing to the combination of double-layer capacitance from the porous carbon and the redox-induced pseudocapacitance of the metal oxides.

Recently we have reported the synthesis and characterization of gold clusters surrounded by *w*-ferrocenyl hexanthiolate ligands with average core radii of 1.0 nm.³⁴ In solutions with high concentrations of supporting electrolyte, the fully ferrocenated clusters are found

to undergo anion induced adsorption to platinum, gold, and carbon electrodes.³⁵ Our group has reported in the past that gold monolayer protected clusters (MPCs), within a certain size regime (core radii of *ca.* 0.8 to *ca.* 2.5 nm), exhibit quantized one-electron double-layer charging, where the gold core undergoes a series of one-electron transfers separated by an evenly spaced voltage interval (ΔV). The capacitance of the cluster (C_{CLU}) can be related to this voltage spacing as

$$C_{CLU} = \frac{e}{\Delta V} \quad (1)$$

where e denotes the charge of an electron. The sub-attofarad capacitance of the MPC is sufficiently small enough to produce voltammetry with detectable ΔV .

The capacitance of the gold MPC is dominated by the dielectric properties of the ligand shell and is remarkably well predicted by the concentric sphere capacitor model in which the gold core serves as the inner conducting sphere, the organic monolayer as the dielectric, and the supporting electrolyte forms the outer conducting sphere. Following this relationship, the capacitance of the cluster can be correlated to both the thickness (d) and static dielectric constant (ϵ) of the organic monolayer in the relationship

$$C_{CLU} = 4\pi\epsilon_0\epsilon\left(\frac{r}{d}\right)(r + d) \quad (2)$$

where ϵ_0 is the permittivity of free space and r is the gold core radius.

The goal of this work is to demonstrate how redox-functionalized MPCs can be utilized in the energy storage domain by exploiting the double-layer capacitance of the gold core with the pseudo-capacitance of the redox active ligands. It has been shown³⁴ that over a small potential range, up to 60 electrons can be transferred onto a single ferrocene-functionalized MPC, with the majority of the electrons being transferred through the redox

charging of the ferrocenes and the rest through the double-layer charging of the gold core. Practical supercapacitors of ferrocenyl-functionalized Au clusters are created here by taking advantage of the anion induced adsorption^{35,47-52} of the clusters onto carbon surfaces. When commercially available carbon nanofoam electrodes, supported mesoporous carbon aerogels already having significant specific capacitances, are coated with the adsorbed ferrocene-functionalized MPCs, the specific capacitance is shown to increase dramatically. The resulting specific capacitances are comparable and in some cases superior to those of other supercapacitor materials, thus redox-functionalized Au MPCs can be added to the growing number of exciting new materials suitable for supercapacitor application.

5.2 Experimental

Experimental

Chemicals. Hexanethiol (HSC6, >99%), dodecanethiol (HSC12, >99%), *t*-octylammonium bromide (Oct₄NBr, >98%), sodium borohydride (NaBH₄, >98%), *t*-butylammonium perchlorate (Bu₄NClO₄, >99%), *t*-butylammonium *p*-toluenesulfonate (Bu₄NC₇H₈O₃S, puress), and *t*-butylammonium hexafluorophosphate (Bu₄NPF₆, puress) from Aldrich, and sodium sulfate (NaSO₄, ACS certified), toluene (reagent grade), acetonitrile (Optima), methylene chloride (HPLC grade), methanol (HPLC grade), tetrahydrofuran (HPLC grade), and ethanol (HPLC grade) from Fisher were used as received. HAuCl₄·xH₂O (from 99.999% pure gold) was synthesized using a literature procedure⁵³ and stored in a freezer at -20°C. Water was purified using a Barnstead NANOpure system (18 MO).

Ferrocene hexanethiol (HSC6Fc) was synthesized by refluxing a mixture of (1.11 g, 3.17 mmol) *w*-bromohexane ferrocene (prepared by a published method⁵⁴) and thiourea (0.600 g, 7.88 mmol) in ethanol (50 mL) overnight. The reaction mixture was neutralized

with NaOH (aq), refluxed for a further 3 h, and then acidified with HCl to pH ~ 2, diluted with water and extracted with CH₂Cl₂, washing the organic extract phase copiously with water. The material obtained after rotary evaporation of the CH₂Cl₂ product solution was chromatographed on silica gel with ethyl acetate/hexanes. ¹H NMR (400 MHz, CD₂Cl₂) of the thiol gave the appropriate NMR peaks: 4.0 (m, 9 H), 2.49 (q, J = 7.2 Hz, 2 H), 2.30 (t, J = 7.6 Hz, 2 H), 1.56 (m, 2 H), 1.46 (m, 2 H), 1.32 (m, 5 H) with no dithiol peaks present and no significant broadening, indicating that the majority of the ferrocenyl groups were in the reduced state.

MPC synthesis. Au₂₂₅(SC6Fc)₄₃ was synthesized as described previously.³⁴ Briefly, vigorous mixing of 3.19 g HAuCl₄·xH₂O in 100 mL deionized water with 5.20 g Oct₄NBr in 200 mL toluene, gave a clear aqueous phase and an orange-brown toluene phase. Adding *w*-ferrocenyl hexanethiol to the isolated organic phase (2:1 ligand-to-Au mole ratio) gave a colorless reaction mixture that was stirred for 20 minutes and then cooled to 0 °C. 3.8 g of NaBH₄ in 10 mL water was added with very rapid stirring and reacted for 1 hour at 0 °C, after which the dark organic phase was collected and the solvent removed on a rotary evaporator at room temperature. The black solid suspension was stirred in 400 mL of acetonitrile for 6 hours and the solid product collected and washed with acetonitrile on a fine glass frit. Determination of the average Au core size and number of ligand analyses has been presented elsewhere,³⁴ based on transmission electron microscopy, UV/Vis absorbance spectroscopy, cyclic and differential pulse voltammetry, and constant potential coulometry.

A mixed monolayer MPC with a lower ferrocene population (*average* composition, by NMR, Au₂₂₅(SC6)₅₈(SC6Fc)₁₇) was prepared by a ligand place exchange between Au₂₂₅(SC6)₇₅ (prepared as previously described⁴⁰) and HSC6Fc at a 1:1 mole ratio of *w*-

ferrocenyl hexanethiol to hexanethiolate ligand. A 10-mL tetrahydrofuran solution of 0.020 g $\text{Au}_{225}(\text{SC6})_{75}$ and 0.0089 g HSC6Fc was stirred for 1 hr, the solvent removed, and the mixed monolayer MPCs rinsed with acetonitrile to remove excess ligand. The relative number of ligands on the exchanged product was analyzed in CD_2Cl_2 solution with ^1H NMR on a Bruker 400 MHz Avance spectrometer with a 5 s relaxation delay time.

Carbon nanofoam electrodes and films. Sheets of pyrolyzed carbon nanofoam electrodes were received from MarkeTech International Inc. (Grade I, 0.4 – 0.5 g/cc density, ca. 400 m^2/g surface area, ca. 60 nm average pore size). To practically utilize the carbon nanofoam electrodes, a square of the carbon nanofoam sheet was cut out with scissors, and a wire coated in a protective plastic jacket was cut on either end to expose the metal wire. One end of the wire was attached to the carbon nanofoam square using silver paste, which led to an electrical connection between the wire and the electrode material. The electrode was then left in an oven set to 70 °C to cure the silver paste overnight. The following day, the silver paste was coated completely with an epoxy to prevent electrochemistry from occurring at the metal junction. Again the electrode was allowed to cure overnight in an oven at 70 °C. Once the epoxy was dry, the electrode was used for electrochemical measurements.

To make the carbon nanofoam powder, the carbon-paper-supported carbon nanofoam was manually ground up into a fine powder using a pestle and mortar. Adsorption of $\text{Au}_{225}(\text{SC6Fc})_{43}$ MPCs onto the powder was achieved by dissolving ca. 50 mg of $\text{Au}_{225}(\text{SC6Fc})_{43}$ MPCs and ca. 50 mg of carbon nanofoam powder in a 2 mL solution of 1.0 M $\text{Bu}_4\text{NClO}_4/\text{CH}_2\text{Cl}_2$. The solution was then sonicated owing to the insolubility of the carbon nanofoam powder in CH_2Cl_2 and allowed to sit for one hour in darkness. Using a glass frit, the excess Bu_4NClO_4 was removed by rinsing the MPC-modified carbon

nanof foam powder with methanol. To cast the powder as a film on a glassy carbon electrode, the carbon nanof foam powder (bare or MPC-modified) was dissolved in CH_2Cl_2 , then dropcast onto a glassy carbon electrode surface and allowed to dry for several minutes.

Electrochemistry. Voltammetry was performed using a Model 100B Bioanalytical Systems (BAS) potentiostat. The three electrode system for investigating the voltammetry of the carbon nanof foam electrode consisted of the carbon nanof foam electrode as the working, vitreous carbon as the counter, and $\text{Ag}/\text{AgCl}/3\text{ M KCl}$ (*aq*) as the reference electrodes. For the carbon nanof foam powder voltammetry, the powder was dropcast onto a 1.5 mm glassy carbon electrode, and the other two electrodes were a Pt wire as the counter and $\text{Ag}/\text{AgCl}/3\text{ M KCl}$ (*aq*) as the reference electrodes. The same three electrode system (without the dropcast powder film) was used to investigate adsorption of the MPCs onto the glassy carbon electrode. Non-aqueous electrochemistry was performed in 0.1 mM MPC degassed CH_2Cl_2 solutions containing 1.0 M Bu_4NClO_4 . Aqueous electrochemistry was performed in 1.0 M NaSO_4 solutions in degassed Nanopure water. Electrochemically adsorbed MPC films were generated by potential cycling at six different scan rates (0.1, 0.05, 0.025, 0.010, 0.005 and 0.002 V/s from 0 to 0.8 V *vs.* Ag/AgCl , to also investigate MPC solution electrochemistry) in a 0.1 mM MPC solution of CH_2Cl_2 containing 1.0 M Bu_4NClO_4 , followed by rinsing the carbon nanof foam working electrode with MPC-free $\text{CH}_2\text{Cl}_2/1.0\text{ M Bu}_4\text{NClO}_4$.

Rotated disk electrochemistry (RDE) was performed on a BAS Model 100B potentiostat and a BAS RDE-1 rotator system. The three electrode cell used a 3 mm Au electrode (working), Pt wire (counter), and $\text{Ag}/\text{AgCl}/3\text{ M KCl}$ (*aq*) (reference) and a sonicated solution of 50 mg of bare or MPC-modified carbon nanof foam powder in 10 mL of 1.0 M

NaSO₄/H₂O. Despite being insoluble in H₂O, after sonication the powder forms a suspension that can be analyzed.

Capacitance calculations. Capacitance, C , measured in Farads (F), can be calculated from a cyclic voltammogram by integrating the area of the voltammetry (both redox peak, when applicable, and double-layer capacitance are included) to calculate the charge, Q in Coulombs (C). The charge can be related to the capacitance by

$$C = Q/V \quad (3)$$

where V is the potential range of the voltammetry over which the charge was calculated.

Scanning electron microscopy (SEM). The bare carbon nanofoam electrode and the manually ground bare carbon nanofoam powder were analyzed via scanning electron microscopy (Hitachi model S-4700). The bare carbon nanofoam electrode sample was prepared by taping a piece of the carbon-paper-supported carbon aerogel down to a glass slide with SEM double-sided tape, and the ground up carbon nanofoam powder sample was prepared by dropcasting a solution of the powder in CH₂Cl₂ (concentration *ca.* 20 mg/mL) onto a glass slide. The samples were analyzed inside the vacuum chamber of the scanning electron microscope at a pressure of 10⁻⁶ Torr.

5.3 Results and Discussion

Recently we have reported on the synthesis of novel Au monolayer protected clusters with average core radii of 1.0 nm (average 225 Au atoms) and on average 43 *w*-ferrocenyl hexanethiolate ligands³⁴ (Au₂₂₅(SC6Fc)₄₃). Intriguingly, these clusters have been shown to adsorb irreversibly to platinum, gold, and carbon electrodes in the presence of high concentrations of certain counter anions (PF₆⁻, ClO₄⁻).³⁵ The adsorption of the Au₂₂₅(SC6Fc)₄₃ MPCs was found to be kinetically slow and nearly irreversible; the only way to remove the film of clusters was to polish the electrode with diamond paste or scan

the electrode potential negative of the electrode's potential of zero charge (E_{PZC}) for hundreds of scans. The mechanism of the adsorption is believed to be an ion-pairing effect between the counter anions adsorbed onto the electrode surface and the oxidized ferroceniums on the monolayer of the MPCs.³⁵ This paper will demonstrate the creation of novel supercapacitors that exploit this strong adsorption by means of adsorbing the fully ferrocenated Au MPCs, capable of transferring 47 electrons per cluster in a small potential range of 0.8 V, to a material that is already high in double-layer capacitance.

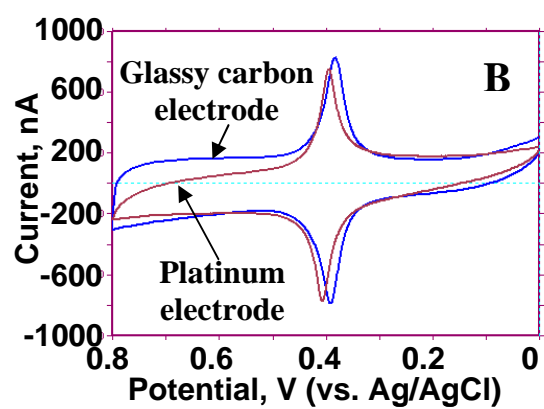
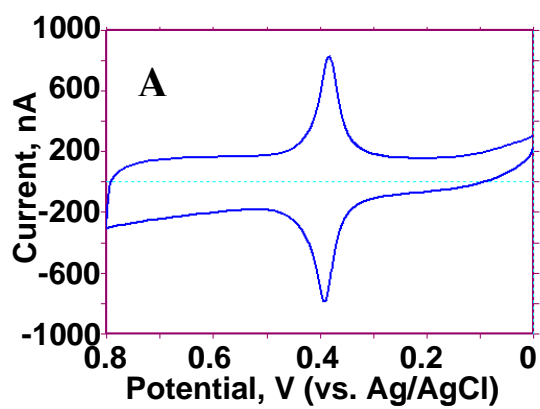
As mentioned previously, Au clusters within a certain size range (core radii of *ca.* 0.8 to *ca.* 2.5 nm) demonstrate quantized one-electron double-layer charging where the potentials of one-electron core charge increments are separated by $\Delta V = e/C_{CLU}$, where e is the charge of an electron, and C_{CLU} is the electrostatically governed double layer capacitance of individual MPCs. It has been shown previously⁴⁰ that hexanethiolate-protected Au₂₂₅ MPCs exhibit ΔV values of 185 mV, which has been demonstrated not to change significantly when redox groups are added to the monolayer.³⁴ Assuming a Au core of 225 atoms and a monolayer of 43 *w*-ferrocenyl hexanethiolate ligands, the ideal specific capacitance for charging a sample of *pure* Au₂₂₅(SC6Fc)₄₃ MPC, over a potential range of 0.8 V, can be calculated to be 79 F/g (Table 5.1). While the ideal specific capacitance of pure ferrocenated Au MPC cannot be reached, not least because of the problem of rapidly intercalating counter ions into it, it can be assumed that adsorbing the clusters on a material already high in capacitance will improve the chances of reaching its full capacitive potential.

Because carbon, in its various forms, is the most extensively used and widely investigated material in supercapacitor electrodes,^{29,55} a similar experiment to the survey experiment of adsorption of the ferrocenated MPCs on a platinum electrode described

previously³⁵ was performed with a glassy carbon disk electrode. Under identical conditions, 1.0 M Bu₄NClO₄ in CH₂Cl₂, the ferrocenated MPCs adsorbed irreversibly on the glassy carbon electrode. Figure 5.1A shows the cyclic voltammogram of the MPC-modified glassy carbon electrode in an *MPC-free* 1.0 M Bu₄NClO₄/CH₂Cl₂ solution. It is evident from the sharp ferrocene redox waves that the clusters have adsorbed strongly onto the glassy carbon electrode. Figure 5.1B compares the adsorbed ferrocenated MPCs on the glassy carbon electrode to that of the same adsorbed MPCs on a platinum electrode under identical conditions. By comparing the charge under the ferrocene redox waves, both the glassy carbon electrode and the Pt electrode lead to MPC adsorption coverages (Γ_{MPC}) of $\sim 3 \times 10^{-12}$ mol/cm² (one monolayer of MPCs is equal to $\sim 9 \times 10^{-12}$ mol/cm²), indicating that the same anion-induced mechanism of adsorption studied previously³⁵ can be applied to the fully ferrocenated Au clusters adsorbing on a carbon surface. The increase in double-layer capacitance seen in the more positive potential region with the glassy carbon electrode can be attributed to the electrode itself, not the MPCs.

Utilizing the strong adsorption of the ferrocenated MPCs onto carbon surfaces, commercially available carbon aerogel substrates (also called “nanofoms”) were used in the presence of 1.0 M Bu₄NClO₄ and ferrocenated MPCs. The MPC-modified hybrid electrodes take advantage of the high double-layer capacitance of the carbon aerogel as well as the double-layer capacitance of the gold MPC core and the pseudocapacitance of the ferrocene redox headgroups of the monolayer. To make the carbon nanofom electrodes, a plastic-protected wire with exposed metal ends was connected to the carbon-paper-supported carbon aerogel (nanofom) electrodes (Marketch International Inc., 254 μm thick) through one metal end with silver paint and cured overnight. The silver paint

Figure 5.1. (A) Cyclic voltammogram (0.025 V/s) of an adsorbed $\text{Au}_{225}(\text{SC6Fc})_{43}$ film formed on a clean glassy carbon electrode from a 0.1 mM MPC, 1.0 M $\text{Bu}_4\text{NClO}_4/\text{CH}_2\text{Cl}_2$ solution and transferred to an *MPC-free* 1.0 M $\text{Bu}_4\text{NClO}_4/\text{CH}_2\text{Cl}_2$ solution. (B) Comparison of cyclic voltammograms of two electrodes treated identically to (A) except that the blue curve is for a $\text{Au}_{225}(\text{SC6Fc})_{43}$ film formed on a clean glassy carbon electrode (same as (A)) and the maroon curve is for a $\text{Au}_{225}(\text{SC6Fc})_{43}$ film formed on a clean platinum electrode. Γ_{MPC} for Pt and glassy C electrodes $\sim 3 \times 10^{-12}$ MPC/cm².



was then covered with epoxy and cured for another 24 hours. A cartoon of the resulting electrode is shown in Figure 5.2 where the area of the electrode could easily be controlled by cutting the desired size of the carbon-paper-supported carbon nanofoam.

To study the enhancement of capacitance resulting from the adsorbed ferrocenated MPCs onto the carbon nanofoam electrodes, cyclic voltammograms of the bare carbon nanofoam electrode and the MPC-modified carbon nanofoam electrode in solutions of 1.0 M NaSO₄/H₂O were compared. The cyclic voltammograms of either the forward or reverse scan can be integrated to calculate the charge (Q) passed over the potential range scanned (V), and the capacitance (C) can then be calculated according to Equation 3 ($C = Q/V$). The procedure for adsorbing the MPCs onto the carbon nanofoam electrodes involved potential cycling the bare carbon nanofoam electrode at six different scan rates (0.1, 0.05, 0.025, 0.010, 0.005 and 0.002 V/s from 0 to 0.8 V vs. Ag/AgCl so as to compare solution MPC electrochemistry at different scan rates) in a 0.1 mM MPC solution of 1.0 M Bu₄NClO₄/CH₂Cl₂, followed by rinsing the carbon nanofoam working electrode with a solution of MPC-free 1.0 M Bu₄NClO₄/CH₂Cl₂. As can be seen in Figure 5.3A, the resulting cyclic voltammogram of the Au₂₂₅(SC6Fc)₄₃-modified carbon nanofoam electrode exhibits significantly higher current than the bare carbon nanofoam electrode over the same potential range. The calculated specific capacitance is listed in Table 5.1.

Two separate similar experiments were performed in which lightly ferrocenated Au MPCs (average composition of Au₂₂₅(SC6)₅₈(SC6Fc)₁₇) and hexanethiolate protected Au MPCs with no ferrocenes (average composition of Au₂₂₅(SC6)₇₅) were used. For the mixed monolayer MPCs, the clusters were found to adsorb onto the carbon nanofoam electrodes in the same procedure as the fully ferrocenated Au clusters, leading to increased currents in cyclic voltammetry measurements in 1.0 M NaSO₄/H₂O solutions (results not shown).

Figure 5.2. Cartoon schematic of the carbon nanofoam electrode used. A plastic-protected wire with exposed metal ends is connected to a square cut-out from a carbon-paper-supported carbon nanofoam sheet through one metal end with silver paint (cured overnight) and sealed with epoxy (cured overnight).

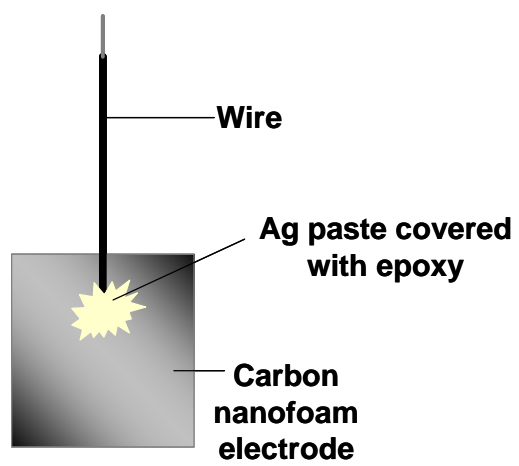


Figure 5.3. (A) Cyclic voltammogram of bare carbon nanofoam electrode (maroon line) and $\text{Au}_{225}(\text{SC6Fc})_{43}$ -modified carbon nanofoam electrode of the same size (blue line) in 1.0 M $\text{NaSO}_4/\text{H}_2\text{O}$. Scan rate was 0.005 V/s and counter electrode was vitreous carbon. (B) Cyclic voltammogram of bare carbon nanofoam electrode (maroon line) and $\text{Au}_{225}(\text{SC6})_{75}$ -modified carbon nanofoam electrode of the same size (blue line) in 1.0 M $\text{NaSO}_4/\text{H}_2\text{O}$. Scan rate was 0.050 V/s and counter electrode was vitreous carbon.

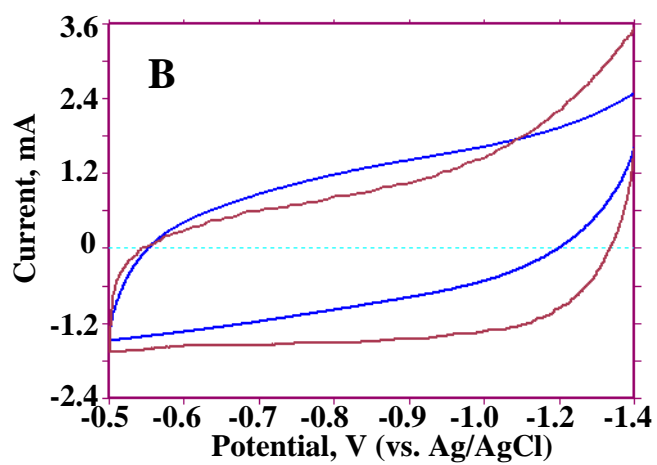
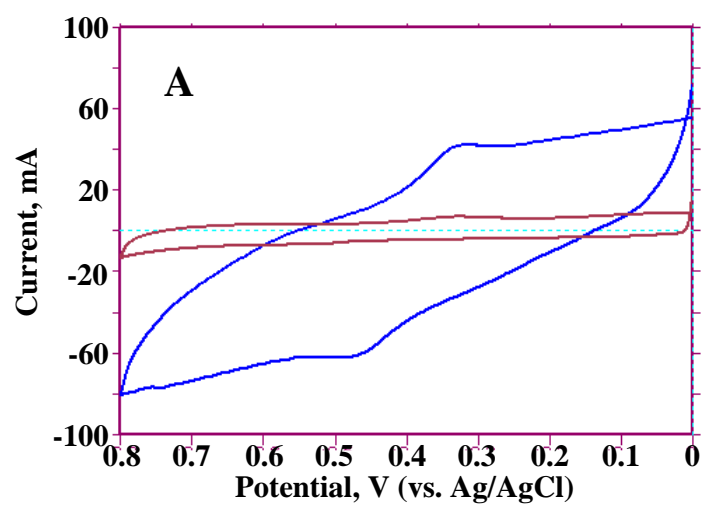


Table 5.1. Specific capacitances of bare and MPC-modified carbon nanofoam electrode and powder.

Material	Specific Capacitance (F/g)	Volumetric Capacitance (F/cm ³)	Area-Normalized Capacitance ^a (F/cm ²)
Theoretical pure, undiluted	79	130	n/a
Au ₂₂₅ (SC6Fc) ₄₃ MPC			
Bare carbon nanofoam electrode	3.9	2.7	0.053 (9.7 x 10 ⁻⁷)
Au ₂₂₅ (SC6) ₇₅ -modified carbon nanofoam electrode	3.7	2.2	0.053 (9.7 x 10 ⁻⁷)
Au ₂₂₅ (SC6) ₅₈ (SC6Fc) ₁₇ -modified carbon nanofoam electrode	28	19	0.37 (7.0 x 10 ⁻⁶)
Au ₂₂₅ (SC6Fc) ₄₃ -modified carbon nanofoam electrode	71	48	1.3 (1.8 x 10 ⁻⁵)
Bare carbon nanofoam powder (dropcast film)	3	n/a	n/a
Au ₂₂₅ (SC6Fc) ₄₃ -modified carbon nanofoam powder (dropcast film)	57	n/a	n/a

^aValues outside parenthesis are area-normalized capacitance in F/cm² using the physical area of the electrode, while values within parenthesis indicate area-normalized capacitance in F/cm² if the total surface area available is used (from manufacturer, 400 m²/g).

While the specific capacitance of the mixed-monolayer MPC-modified carbon nanofoam electrode did not increase to the same extent as that of the fully ferrocenated MPCs, most likely owing to the smaller number of redox active sites, a significant amplification of the specific capacitance is observed still (Table 5.1).

When the same experiment was also performed using hexanethiolate protected Au MPCs of the same size but with no ferrocene headgroups, the resulting cyclic voltammograms of the bare and MPC-modified carbon nanofoam electrodes, shown in Figure 5.3B, exhibit no notable change in the capacitance of the nanofoam electrode before and after introduction of the $\text{Au}_{225}(\text{SC6})_{75}$ MPCs. This lack of an increase in capacitance is most likely due to the inability of the hexanethiolate protected MPCs to adsorb to the carbon surface, despite the presence of the high electrolyte concentration. As demonstrated previously,³⁵ the adsorption of the ferrocenyl hexanethiolate protected Au clusters is believed to be caused by ion-pair interactions between the positively charged ferrocenium head groups and the negatively charged counter anions adsorbed on the electrode surface. Without these ferrocenium groups, as is the case with the hexanethiolate protected Au clusters, strong adsorption to the electrode surface does not take place.

The specific capacitances (F/g) of the bare and MPC-modified carbon nanofoam electrodes are listed in Table 5.1. Modification of the carbon nanofoam electrode with the mixed monolayer MPC ($\text{Au}_{225}(\text{SC6})_{58}(\text{SC6Fc})_{17}$) causes a nearly ten-fold increase in specific capacitance, while the adsorption of the fully ferrocenated MPCs ($\text{Au}_{225}(\text{SC6Fc})_{43}$) to the carbon nanofoam electrode leads to a nearly twenty-fold increase in specific capacitance. This huge increase is an exciting result in that it demonstrates that a simple procedure of adsorbing fully ferrocenated Au MPCs onto a carbon nanofoam electrode produces a novel electrode material of very high specific capacitance.

The stability of the fully ferrocenated MPC-modified carbon nanofoam electrode was also investigated in a 1.0 M NaSO₄/H₂O solution. Figure 5.4 shows cyclic voltammograms of a Au₂₂₅(SC6Fc)₄₃-modified electrode potential cycled fifty times between 0 and 0.8 V at 0.025 V/s, corresponding to *ca.* 53 minutes of potential scanning time. The electrode demonstrates a 34% loss in capacitance over the fifty cycles. This loss in capacitance is not ideal, however it is also not grave for approximately one hour of use.

One issue the Au₂₂₅(SC6Fc)₄₃-modified carbon nanofoam electrode does appear to present is that upon adsorption of the MPCs, along with the desired increase in capacitance to the electrode, an undesired increase in uncompensated resistance (iR_{unc}) across the electrode appears. This increase in ohmic drop can be improved through several methods, including decreasing the physical area of the electrode as well as carefully drying the electrode between the CH₂Cl₂ cycling step (to generate adsorbed MPCs) and the H₂O cycling step (to measure capacitance). Figure 5.5A and B show the effect of decreasing the carbon nanofoam physical size on uncompensated resistance, using two differently sized (areas of 9.5 and 2.3 cm²) (A) bare carbon nanofoam electrodes and (B) ferrocenated MPC-modified carbon nanofoam electrodes in 1.0 M NaSO₄/H₂O solutions. The natural log of current vs. time curves and corresponding *RC* time constant values of the differently sized electrodes are shown in Figure 5.1A and listed in Table 5.1A of the Appendix, respectively. Even without adsorbed MPCs, the larger bare carbon nanofoam electrode has significantly higher resistance than the smaller electrode demonstrating that the electrode size, as one would expect, has a considerable effect on the uncompensated resistance. However, there is still an increase in capacitance observed when the ferrocenated Au MPCs are adsorbed onto the carbon nanofoam electrodes, regardless of the size of the electrode.

Figure 5.4. Fifty cyclic voltammograms of $\text{Au}_{225}(\text{SC6Fc})_{43}$ -modified carbon nanofoam electrode in 1.0 M $\text{NaSO}_4/\text{H}_2\text{O}$ taken at scan rate 0.025 V/s. After fifty cycles, there is *ca.* 34% loss in current. Counter electrode was vitreous carbon.

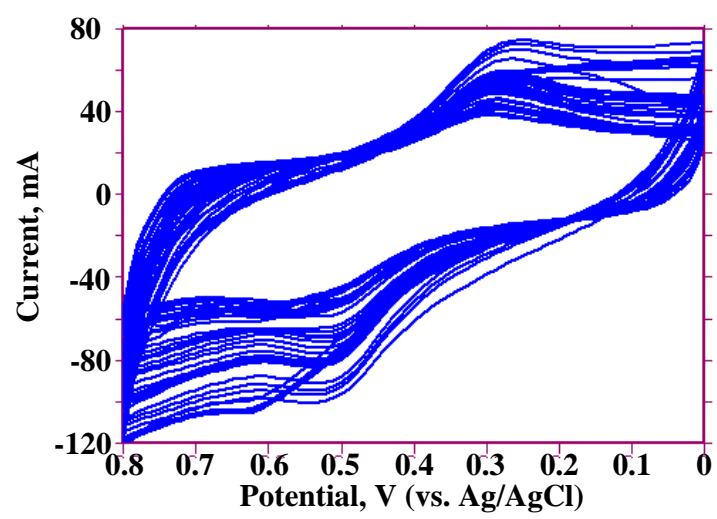
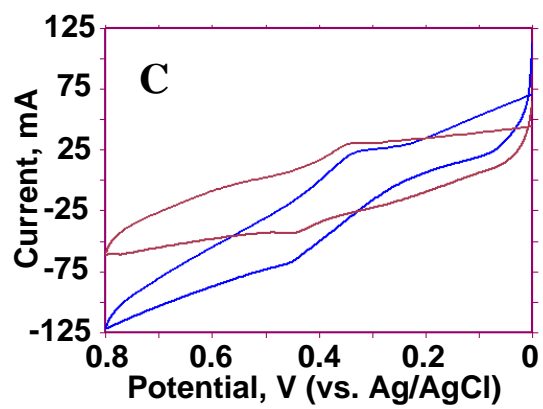
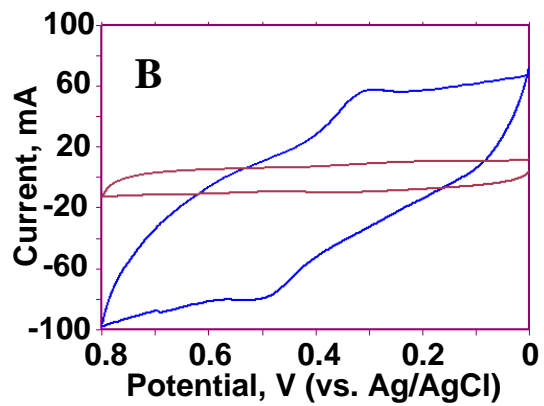
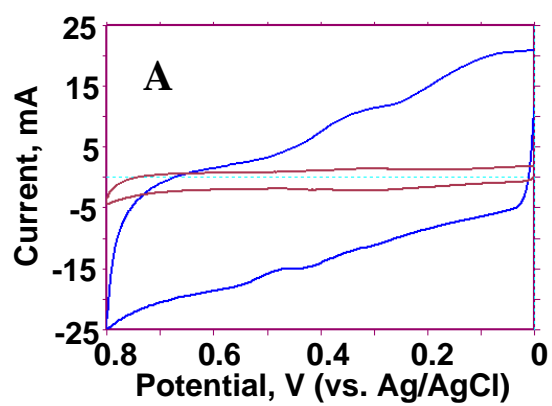


Figure 5.5. Cyclic voltammograms of (A) bare and (B) $\text{Au}_{225}(\text{SC6Fc})_{43}$ -modified carbon nanofoam electrodes in 1.0 M $\text{NaSO}_4/\text{H}_2\text{O}$ at 0.010 V/s with vitreous carbon counter electrode. The larger blue curves are for a carbon nanofoam electrode with area 9.5 cm^2 , and the smaller maroon curves are for a carbon nanofoam electrode with area 2.3 cm^2 . (C) Cyclic voltammograms of the same $\text{Au}_{225}(\text{SC6Fc})_{43}$ -modified carbon nanofoam electrode ($A = 9.5 \text{ cm}^2$) in 1.0 M $\text{NaSO}_4/\text{H}_2\text{O}$ at 0.002 V/s with (maroon curve) and without (blue curve) the drying at 70°C for one hour step between cycling in 0.1 mM MPC/1.0 M $\text{Bu}_4\text{NClO}_4/\text{CH}_2\text{Cl}_2$ (for MPC adsorption) and cycling in 1.0 M $\text{NaSO}_4/\text{H}_2\text{O}$ (for capacitance measurements). The counter electrode used for both was vitreous carbon.

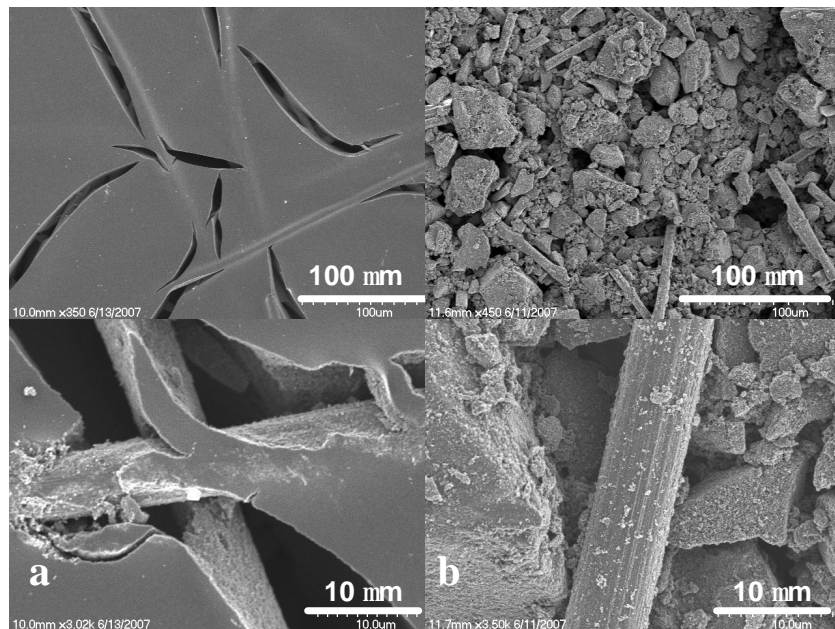


The resistance that appears in the 1.0 M NaSO₄/H₂O solutions using the MPC-modified carbon nanofoam electrodes is to a large extent owing to the lingering organic CH₂Cl₂ solvent and Bu₄NClO₄ electrolyte molecules. In an effort to remove these organic species from the MPC-modified carbon nanofoams, the electrode was allowed to dry for one hour in an oven set to 70 °C, and then the typical cycling in the 1.0 M NaSO₄/H₂O was performed. Figure 5.5C shows cyclic voltammograms of the same MPC-modified carbon nanofoam electrode with and without this drying step. From these voltammograms it is apparent that the drying significantly decreases the uncompensated resistance. Moreover, it is assumed that further drying in between organic and aqueous voltammetry, and even drying under vacuum, would greatly improve the performance of these MPC-modified carbon nanofoam electrodes in terms of ohmic effects.

In another effort to enhance the performance of the ferrocenated MPC-modified carbon nanofoam electrodes, the electrode material was manually ground up into a fine powder. Figure 5.6 shows scanning electron microscopy (SEM) images of the bare carbon nanofoam electrode (a, c) and the ground up bare carbon nanofoam powder (b, d). The SEM images of the electrodes show platelets of carbon nanofoam firmly attached to random carbon fibers, interspersed with macro-porosity (the ratio of carbon fiber is *ca.* 80% by weight). From the images it is apparent that, upon grinding, the microscale structure of the carbon aerogel is altered, and, along with the random carbon fibers, polydisperse particles with diameters ranging from several to 50 μm are formed.

Au₂₂₅(SC6Fc)₄₃ MPCs were adsorbed onto the carbon nanofoam powder by allowing the ground up carbon nanofoam (*ca.* 50 mg) to sit in a 2 mL solution of 1.0 M Bu₄NClO₄/CH₂Cl₂ containing the ferrocenated MPCs (*ca.* 50 mg) for one hour in the dark.

Figure 5.6. Scanning electron micrographs of (a and c) bare carbon-paper-supported carbon nanofoam electrode and (b and d) manually ground bare carbon nanofoam powder.



It has been shown previously³⁵ that the $\text{Au}_{225}(\text{SC6Fc})_{43}$ adsorbs onto a Pt electrode in the presence of 1.0 M Bu_4NClO_4 in CH_2Cl_2 with no applied potential. (Because the rest potential of the ferrocenated MPCs lies near the ferrocene oxidation potential, it is believed that several of the 43 redox moieties are actually in the oxidized ferrocenium state, thus the adsorption mechanism, believed to be an ion-pair formation between the adsorbed counteranions on the electrode surface and the oxidized monolayer ferroceniums, can still occur with no applied potential.³⁵)

Figure 5.7 shows the cyclic voltammograms in 1.0 M $\text{NaSO}_4/\text{H}_2\text{O}$ of the bare and ferrocenated MPC-modified carbon nanofoams dropcast as films onto a glassy carbon electrode. Clearly the adsorption of the $\text{Au}_{225}(\text{SC6Fc})_{43}$ MPCs increases the capacitance of the carbon nanofoam in the powder form just as it did in the intact carbon nanofoam electrode. The specific capacitances of the bare and MPC-modified carbon nanofoam films on the glassy carbon electrode are listed in Table 5.1. While the specific capacitance of the nanofoam powder does increase, the effect is not as great as the intact nanofoam electrode. One can speculate that the decrease in specific capacitance of the powder as compared to the intact electrode may arise from some discontinuity within the material dropcast on the electrode. As seen in the SEM images in Figure 5.6, the carbon nanofoam powder particles are quite polydisperse in size and shape, and the dropcasting method (used for SEM images as well as for electrochemical measurements) appears to lead to a non-uniform film of the powder.

The cyclic voltammograms, normalized by mass, of a film of MPC-modified carbon nanofoam powder on a glassy carbon electrode and an MPC-modified intact carbon nanofoam electrode are compared in Figure 5.8. From the two voltammograms it is evident that the intact carbon nanofoam electrode has a higher specific capacitance than the

Figure 5.7. Cyclic voltammogram of bare carbon nanofoam powder dropcast on a glassy carbon disk electrode (maroon line) and $\text{Au}_{225}(\text{SC6Fc})_{43}$ -modified carbon nanofoam powder dropcast on the same glassy carbon disk electrode (blue line) in 1.0 M $\text{NaSO}_4/\text{H}_2\text{O}$. Scan rate was 0.002 V/s and counter electrode was platinum wire.

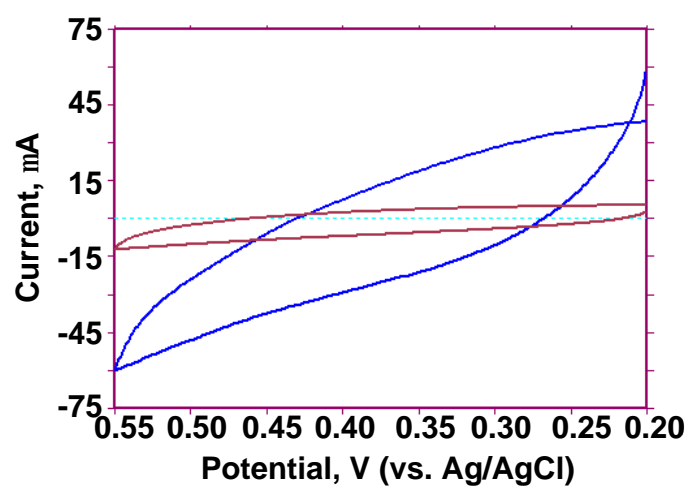
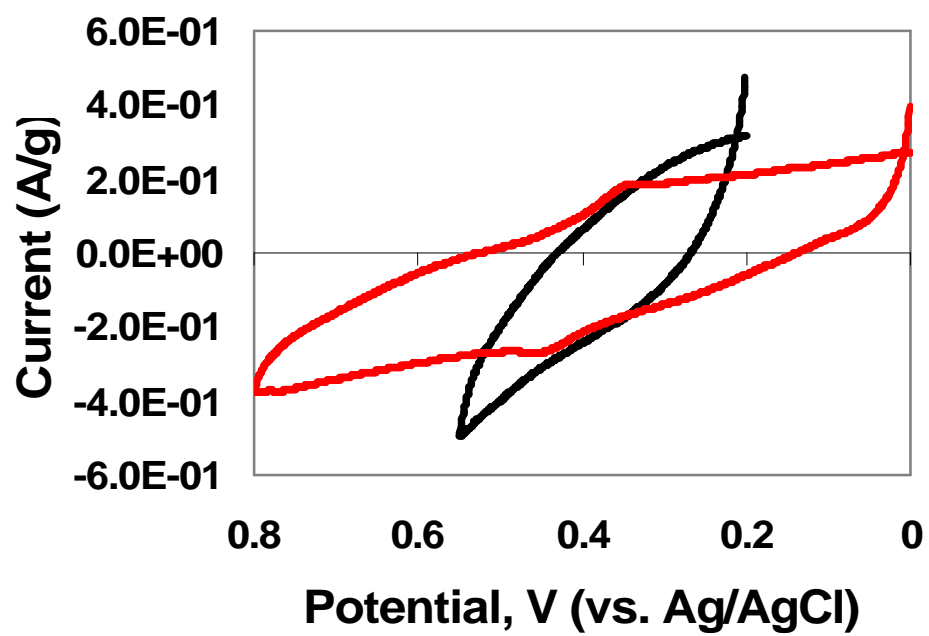


Figure 5.8. Mass normalized cyclic voltammograms of $\text{Au}_{225}(\text{SC6Fc})_{43}$ -modified carbon nanofoam electrode (red line) and $\text{Au}_{225}(\text{SC6Fc})_{43}$ -modified carbon nanofoam powder dropcast on a glassy carbon disk electrode (black line) in 1.0 M $\text{NaSO}_4/\text{H}_2\text{O}$. Scan rate was 0.005 V/s. Counter electrode was vitrous carbon for the MPC-modified nanofoam electrode and platinum wire for the MPC-modified nanofoam powder film.



powder (Table 5.1), and it can also clearly be seen that the uncompensated resistance of the intact electrode is smaller than that of the nanofoam powder. This increase in resistance upon mechanical stress to the material is also most likely owing to the polydispersity of the particles and the discontinuity of the dropcast film on the electrode. The corresponding natural log of current vs. time curve and RC value for the carbon nanofoam powder can also be seen in the Appendix in Figure 5.1A and Table 5.1A, respectively.

While it was completely expected to see large increases in capacitance within the potential range of the ferrocene/ferrocenium redox wave owing to the large increase in pseudocapacitance from the 43 ferrocenes per MPC, the large increase in capacitance that is observed at potentials more positive and more negative than the redox wave is not straight forward. One can speculate that on the carbon nanofoam material, the Au cores of the MPCs are being charged through the double-layer charging phenomenon discussed previously. However, in previous experiments where the $\text{Au}_{225}(\text{SC6Fc})_{43}$ MPC were adsorbed to a disk electrode,³⁵ no increase in double-layer capacitance was observed outside the ferrocene redox wave for Pt or glassy carbon electrodes. Because the carbon nanofoam is such a high surface area material, much more cluster is able to adsorb onto it than that of a typical disk electrode, therefore perhaps the increased amount of adsorbed MPCs leads to a more visible effect of the charging of the Au cores at the potentials more positive and more negative of the ferrocene redox wave. Another possibility is that the adsorption of the ferrocenated MPCs on the high-surface area electrode leads to an enhancement of specific adsorption of counter ions, which would also significantly increase the double-layer capacitance of the electrode.

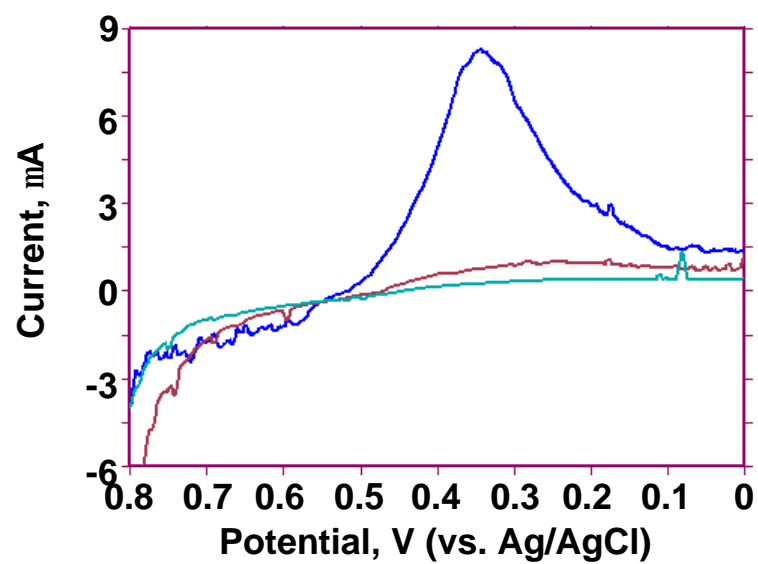
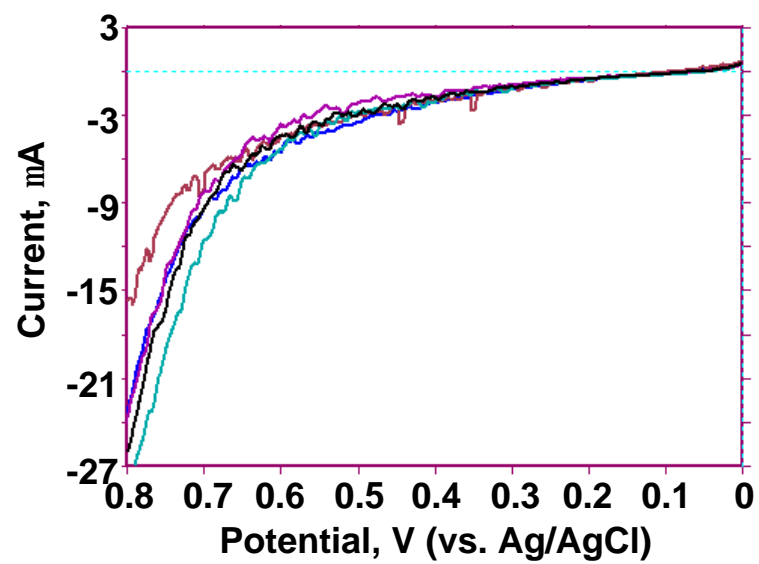
Previously our group has reported on the mass-transport control of the double layer charging of Au MPCs with mixed monolayers of octanethiolate and ω -

ferrocenyloctanethiolate.⁵⁶ Rotated disk voltammetry for the mixed monolayer MPCs exhibited a ferrocene oxidation wave with a limiting current under hydrodynamic mass transport control, however the current-potential curves preceding (“prewave”) and following (“postwave”) the ferrocene wave, also responded to the electrode rotation rate. The slopes ($\Delta i/\Delta E$) of the pre- and post-wave regions were found to be proportional to the square root of the electrode rotation rate ($\omega^{1/2}$), indicating that the charging occurring in those potentials were also under hydrodynamic control. The charging was attributed to the charging of the double layers of the MPCs, leading the authors to characterize the Au clusters as diffusing, molecule-sized “nanoelectrodes”.

In an effort to further understand the charging occurring outside the ferrocene wave in the fully ferrocenated MPCs adsorbed on the carbon nanofoam material presented here, a similar experiment was attempted. A three electrode system of a rotating disk Au electrode, Ag/AgCl (*aq*) reference electrode, and Pt wire electrode were used in a sonicated slurry of *ca.* 50 mg of Au₂₂₅(SC₆Fc)₄₃-modified carbon nanofoam powder in 10 mL of 1.0 M NaSO₄/H₂O. The hydrodynamic wave was collected at 0.010 V/s at a series of rotation rates (400 – 10000 rpm). The goal of the experiment was to not only observe the ferrocene oxidation wave but to also observe the “prewave” and “postwave” slopes as a function of the square root of the electrode rotation rate in hopes that the double-layer charging of the MPCs would be observed.

Unfortunately, the experiment could never be completed as the carbon nanofoam powder particles were simply too big to undergo fast enough hydrodynamic mass transport to the electrode to be measured. As was shown in the SEM images in Figure 5.6, the carbon nanofoam particles are quite polydisperse in size and shape with diameters ranging from several to 50 μm . This slow particle transport is evident in Figure 5.9 which shows

Figure 5.9. Rotated disk voltammetry of bare carbon nanofoam powder sonicated in 1.0 M NaSO₄/H₂O at 0.010 V/s and rotation rates of (A) 400 (teal curve), 625 (purple curve), 900 (black curve), 1600 (blue curve), and 2500 (maroon curve) rpm and (B) 1600 (maroon curve), 2500 (blue curve), and 3600 (teal curve) rpm. Counter electrode for all scans was a platinum wire.



five voltammograms of the bare carbon nanofoam powder slurry recorded at rotation rates ranging from 400 – 2500 rpm (A) and 2500 – 3600 rpm (B). The limiting current does not appear to change with rotation rate, and the small changes that are observed are not in any particular direction. In Figure 5.9, one particular scan (rotation rate of 2500 rpm) gives a very large peak which can be attributed to aggregation of the nanofoam particles at the Au electrode. Since the nanofoam particles are insoluble in H₂O, it is hard to prevent aggregation of the particles in the solution. Because this experiment worked so well previously,⁵⁶ it should be pursued, once the obstacle of carbon nanofoam particle size is overcome. A method to improve the particle size and shape monodispersity may be to use a ball mill to grind the nanofoam into a powder automatically rather than manually as it was done here.

5.4 Conclusions

In conclusion, it has been convincingly demonstrated that the simple anion-induced adsorption of ferrocenated Au MPCs onto carbon-paper-supported carbon aerogel (nanofoam) dramatically increases the specific capacitance of the material. The increase can be attributed to both the double-layer charging of the Au core of the MPCs as well as the redox charging of the on average 43 ferrocenyl ligands per MPC. The fully ferrocenated MPC-modified nanofoam electrodes have decent stability, losing *ca.* 34% capacitance over a little under one hour of nonstop usage. The uncompensated resistance of the MPC-modified electrode can be improved by decreasing the size of the electrode as well as thorough drying of the electrode to remove all excess organic solvent and electrolyte molecules prior to aqueous electrochemistry.

The carbon nanofoam material was investigated as both a carbon-paper-supported electrode and as a ground up powder. While both undergo adsorption of MPCs onto the

surface, the fully ferrocenated MPC-modified intact electrode gives a higher specific capacitance and a lower uncompensated resistance than that of the powder, most likely owing to the polydispersity in size and shape of the powder particles and the inhomogeneity of the dropcast films of the powder. Attempts were made to utilize rotating disk voltammetry to further investigate the increased double-layer capacitance at potentials more positive and more negative than the ferrocene redox wave, however the experiments are inconclusive owing to the slow mass transport of the large, bulky nanofoam powder particles.

5.5 Acknowledgments

This research was supported by grants from the National Science Foundation and Office of Naval Research. Contributions from Dr. Ramjee Balasubramanian, Dr. Christopher Beasley, and Stephanie E. A. Gratton from the University of North Carolina are also acknowledged.

5.6 References

- (1) Burke, A. J. *Power Sources* **2000**, 91, 37-50.
- (2) Conway, B. E. *Electrochemical Supercapacitors, Scientific Fundamentals and Technological Applications*; Kluwer Academic/Plenum Press: New York, 1999.
- (3) Winter, M.; Brodd, R. J. *Chem. Rev.* **2004**, 104, 4245-4269.
- (4) Lin, C. Q.; Popov, B. N.; Ploehn, H. J. *J. Electrochem. Soc.* **2002**, 149, A167-A175.
- (5) Frackowiak, E.; Beguin, F. *Carbon* **2001**, 39, 937-950.
- (6) Fusalba, F.; Ho, H. A.; Breau, L.; Belanger, D. *Chem. Mat.* **2000**, 12, 2581-2589.
- (7) Villers, D.; Jobin, D.; Soucy, C.; Cossement, D.; Chahine, R.; Breau, L.; Belanger, D. *J. Electrochem. Soc.* **2003**, 150, A747-A752.
- (8) Conway, B. E.; Birss, V.; Wojtowicz, J. *J. Power Sources* **1997**, 66, 1-14.
- (9) Zheng, J. P.; Jow, T. R. *J. Electrochem. Soc.* **1995**, 142, L6-L8.
- (10) Soudan, P.; Gaudet, J.; Guay, D.; Belanger, D.; Schulz, R. *Chem. Mat.* **2002**, 14, 1210-1215.
- (11) Fischer, A. E.; Pettigrew, K. A.; Rolison, D. R.; Stroud, R. M.; Long, J. W. *Nano Lett.* **2007**, 7, 281-286.
- (12) Hu, Y. S.; Guo, Y. G.; Sigle, W.; Hore, S.; Balaya, P.; Maier, J. *Nat. Mater.* **2006**, 5, 713-717.
- (13) Cottineau, T.; Toupin, M.; Delahaye, T.; Brousse, T.; Belanger, D. *Appl. Phys. A-Mater. Sci. Process.* **2006**, 82, 599-606.
- (14) Broughton, J. N.; Brett, M. J. *Electrochim. Acta* **2004**, 49, 4439-4446.
- (15) Brousse, T.; Toupin, M.; Belanger, D. *J. Electrochem. Soc.* **2004**, 151, A614-A622.
- (16) Brousse, T.; Belanger, D. *Electrochem. Solid State Lett.* **2003**, 6, A244-A248.
- (17) Nelson, P. A.; Owen, J. R. *J. Electrochem. Soc.* **2003**, 150, A1313-A1317.
- (18) Chang, J. K.; Tsai, W. T. *J. Electrochem. Soc.* **2003**, 150, A1333-A1338.
- (19) Kim, H.; Popov, B. N. *J. Electrochem. Soc.* **2003**, 150, A1153-A1160.
- (20) Wu, N. L.; Wang, S. Y.; Han, C. Y.; Wu, D. S.; Shiue, L. R. *J. Power Sources* **2003**, 113, 173-178.

- (21) Toupin, M.; Brousse, T.; Belanger, D. *Chem. Mat.* **2002**, *14*, 3946-3952.
- (22) Hu, C. C.; Tsou, T. W. *Electrochim. Acta* **2002**, *47*, 3523-3532.
- (23) Wu, N. L. *Mater. Chem. Phys.* **2002**, *75*, 6-11.
- (24) Chin, S. F.; Pang, S. C.; Anderson, M. A. *J. Electrochem. Soc.* **2002**, *149*, A379-A384.
- (25) Lee, H. Y.; Kim, S. W. *Electrochem. Solid State Lett.* **2001**, *4*, A19-A22.
- (26) Pang, S. C.; Anderson, M. A. *J. Mater. Res.* **2000**, *15*, 2096-2106.
- (27) Lee, H. Y.; Goodenough, J. B. *J. Solid State Chem.* **1999**, *148*, 81-84.
- (28) Lin, C.; Ritter, J. A.; Popov, B. N. *J. Electrochem. Soc.* **1998**, *145*, 4097-4103.
- (29) Frackowiak, E. *Phys. Chem. Chem. Phys.* **2007**, *9*, 1774-1785.
- (30) Fang, W. C.; Chyan, O.; Sun, C. L.; Wu, C. T.; Chen, C. P.; Chen, K. H.; Chen, L. C.; Huang, J. H. *Electrochem. Commun.* **2007**, *9*, 239-244.
- (31) Liu, H. T.; He, P.; Li, Z. Y.; Liu, Y.; Li, J. H. *Electrochim. Acta* **2006**, *51*, 1925-1931.
- (32) Lee, J. Y.; Liang, K.; An, K. H.; Lee, Y. H. *Synth. Met.* **2005**, *150*, 153-157.
- (33) Qin, X.; Durbach, S.; Wu, G. T. *Carbon* **2004**, *42*, 451-453.
- (34) Wolfe, R. L.; Balasubramanian, R.; Tracy, J. B.; Murray, R. W. *Langmuir* **2007**, *23*, 2247-2254.
- (35) Wolfe, R. L.; Balasubramanian, R.; Feldberg, S. W.; Murray, R. W. *J. Am. Chem. Soc.* **Submitted**.
- (36) Hicks, J. F.; Miles, D. T.; Murray, R. W. *J. Am. Chem. Soc.* **2002**, *124*, 13322-13328.
- (37) Ingram, R. S.; Hostetler, M. J.; Murray, R. W.; Schaaff, T. G.; Khoury, J. T.; Whetten, R. L.; Bigioni, T. P.; Guthrie, D. K.; First, P. N. *J. Am. Chem. Soc.* **1997**, *119*, 9279-9280.
- (38) Chen, S. W.; Ingram, R. S.; Hostetler, M. J.; Pietron, J. J.; Murray, R. W.; Schaaff, T. G.; Khoury, J. T.; Alvarez, M. M.; Whetten, R. L. *Science* **1998**, *280*, 2098-2101.
- (39) Chen, S. W.; Murray, R. W.; Feldberg, S. W. *J. Phys. Chem. B* **1998**, *102*, 9898-9907.

- (40) Wolfe, R. L.; Murray, R. W. *Anal. Chem.* **2006**, 78, 1167-1173.
- (41) Kim, Y. G.; Garcia-Martinez, J. C.; Crooks, R. M. *Langmuir* **2005**, 21, 5485-5491.
- (42) Quinn, B. M.; Liljeroth, P.; Ruiz, V.; Laaksonen, T.; Kontturi, K. *J. Am. Chem. Soc.* **2003**, 125, 6644-6645.
- (43) Yang, Y.; Pradhan, S.; Chen, S. *Journal of American Chemical Society* **2004**, 126, 76-77.
- (44) Chaki, N. K.; Kakade, B.; Sharma, J.; Mahima, S.; Vijayamohanan, K. P.; Haram, S. K. *J. Appl. Phys.* **2004**, 96, 5032-5036.
- (45) Chaki, N. K.; Singh, P.; Dharmadhikari, C. V.; Vijayamohanan, K. P. *Langmuir* **2004**, 20, 10208-10217.
- (46) Garcia-Morales, V.; Mafe, S. *J. Phys. Chem. C* **2007**, 111, 7242-7250.
- (47) Yamada, M.; Nishihara, H. *ChemPhysChem* **2004**, 5, 555-559.
- (48) Yamada, M.; Nishihara, H. *C. R. Chim.* **2003**, 6, 919-934.
- (49) Yamada, M.; Nishihara, H. *Langmuir* **2003**, 19, 8050-8056.
- (50) Yamada, M.; Tadera, T.; Kubo, K.; Nishihara, H. *J. Phys. Chem. B* **2003**, 107, 3703-3711.
- (51) Yamada, M.; Quiros, I.; Mizutani, J.; Kubo, K.; Nishihara, H. *Phys. Chem. Chem. Phys.* **2001**, 3, 3377-3381.
- (52) Men, Y.; Kubo, K.; Kurihara, M.; Nishihara, H. *Phys. Chem. Chem. Phys.* **2001**, 3, 3427-3430.
- (53) Brauer, G. *Handbook of Preparative Inorganic Chemistry*; Academic Press: New York, 1965.
- (54) Yu, C. J.; Wang, H.; Wan, Y. J.; Yowanto, H.; Kim, J. C.; Donilon, L. H.; Tao, C. L.; Strong, M.; Chong, Y. C. *J. Org. Chem.* **2001**, 66, 2937-2942.
- (55) Pandolfo, A. G.; Hollenkamp, A. F. *J. Power Sources* **2006**, 157, 11-27.
- (56) Green, S. J.; Stokes, J. J.; Hostetler, M. J.; Pietron, J.; Murray, R. W. *J. Phys. Chem. B* **1997**, 101, 2663-2668.

5.7 Appendix of Chapter V

In an effort to calculate the uncompensated resistance values (R) present in the various bare and MPC-modified carbon nanofoam electrodes and powders, natural log current vs. time was plotted for the reverse scans of the corresponding cyclic voltammograms. From these voltammograms, resistance times capacitance (RC) time constants were calculated. Because the capacitances (C) of the material are so big, this attempt was unsuccessful in determining the individual resistance values. The plots for the small (physical area = 2.3 cm^2) bare carbon nanofoam electrode (A), large (physical area = 9.5 cm^2) bare (B) and $\text{Au}_{225}(\text{SC6Fc})_{43}$ -modified (C) carbon nanofoam electrodes, and $\text{Au}_{225}(\text{SC6Fc})_{43}$ -modified carbon nanofoam powder (D) are shown in Figure 5.1A with the corresponding RC values in Table 5.1A. RC values were derived from the slopes of the first five points, shown in the insets of the plots in Figure 5.1A, using the equation^{1A}

$$i = \exp\left(\frac{-t}{RC}\right) \quad (1A)$$

where i is the current measured.

^{1A} Bard, A. J.; Faulkner, L. R. *Electrochemical Methods: Fundamentals and Applications*; Second ed.; Wiley: New York, 2001.

Figure 5.1A. Plots of natural log of current ($\ln(I)$) vs. time (t) for the small (physical area = 2.3 cm^2) bare carbon nanofoam electrode (A), large (physical area = 9.5 cm^2) bare (B) and $\text{Au}_{225}(\text{SC6Fc})_{43}$ -modified (C) carbon nanofoam electrodes, and $\text{Au}_{225}(\text{SC6Fc})_{43}$ -modified carbon nanofoam powder (D). The insets in each plot are of the first five points of the larger plot in which the RC values were derived from the slopes using Equation 1A.

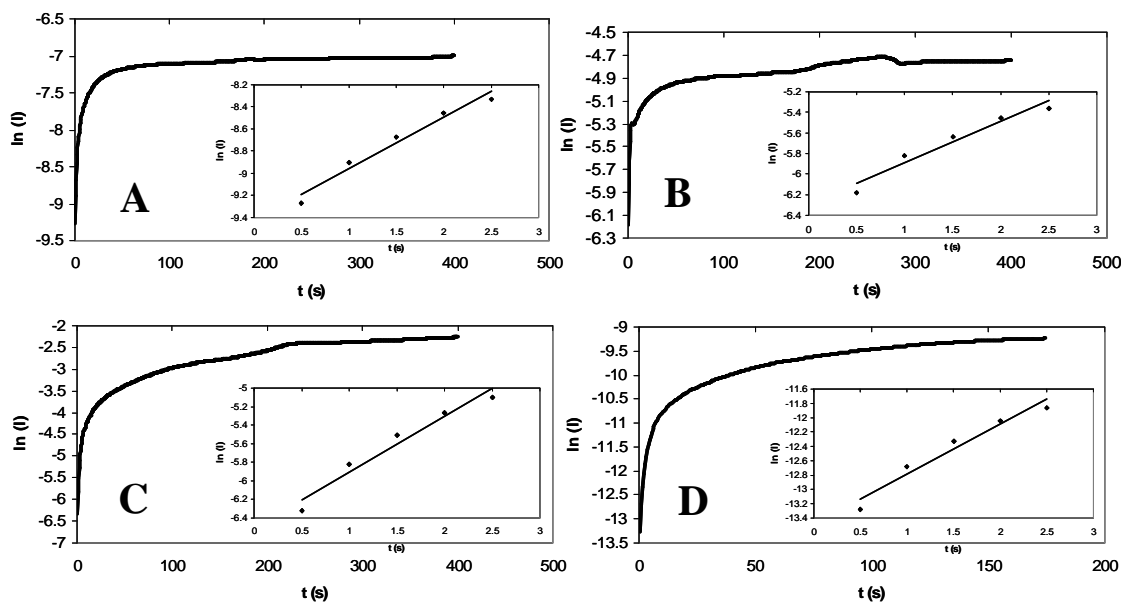


Table 5.1A. *RC* time constant and capacitance values for different carbon nanofoam electrode materials.

Electrode Material	<i>RC</i> Time Constant (s)	Capacitance (F)
Small bare carbon nanofoam electrode (physical A = 2.3 cm ²)	2.2	0.46
Large bare carbon nanofoam electrode (physical A = 2.3 cm ²)	2.4	4.4
Au ₂₂₅ (SC6Fc) ₄₃ -modified large carbon nanofoam electrode	1.7	52
Au ₂₂₅ (SC6Fc) ₄₃ -modified carbon nanofoam powder (dropcast film)	1.4	0.049

CHAPTER VI

CATALYSIS WITH MONOLAYER PROTECTED METAL CLUSTERS

6.1 Introduction

The synthesis, characterization, and applications of monolayer protected clusters (MPCs) of metal atoms have been hot topics in the recent scientific literature¹⁻⁶ owing to the unique size-dependent properties of the metal cores, bridging molecular and bulk, and the stability and reusability of the MPCs as a result of the protecting monolayer. While there are numerous routes to synthesizing MPCs,⁷ the Brust-Schiffrin two-phase synthesis,² which includes a reduction of the gold salt, growth of the gold core, and passivation of the core by the alkanethiolate monolayer, has proved to be the most successful in producing air- and solvent-stable, robust, and reusable small metal clusters. The original synthesis, for example, creates an octanethiolate monolayer, however much research has been done in functionalizing the metal core with various moieties,⁸⁻¹⁴ which has led to captivating science as well as numerous applications. Among the applications is the investigation of metal MPCs in biological systems which led to the development of a modified Brust-Schiffrin synthesis to create water-soluble metal clusters. To make these clusters soluble in aqueous solutions, the synthesis used polar ligands such as *N*-(2-mercaptopropionyl)glycine (also known as tiopronin),¹⁵ mercaptoammonium,¹⁶ *N*-acetyl-*L*-cysteine,¹⁷ and glutathione,¹⁸ among others. Further modifications to the synthesis have included changing the core metal from gold to other metals such as silver and palladium.¹⁶

Another intriguing application that has come out of the MPCs studies is their use in catalysis. While naked colloidal metals and supported clusters still dominate the catalysis literature, there has been more recent interest in examining the catalytic reactivity of metal MPCs.^{10,11,19-28} While those metals whose catalytic properties are well established, particularly those of periodic Groups 8–10, and most particularly nickel, palladium, and platinum, have a marked ability to activate the hydrogen molecule by dissociative chemisorption and to catalyze a wide variety of reactions in which hydrogen atoms are intermediates,²⁹ Au had been generally considered catalytically inactive until 1989 when Haruta et. al. reported supported gold nanoparticles being extremely active in the catalytic oxidation of CO.³⁰ Following that report, quantum chemical calculations revealed an energetically reasonable reaction path for CO oxidation on gold particles containing 10 atoms.³¹⁻³³ Now it is known that supported gold also catalyzes other oxidation reactions, as well as hydrogenation, water-gas shift, and nitrogen oxide reduction.³²

Catalytic activity has been shown to depend strongly on the method of synthesis, the nature of the support, the size of the metal nanoparticles, and the thermal history of the catalyst. While supported metal clusters have been shown to make respectable heterogeneous catalysts, reaction rates can be slow owing to the molecules having to diffuse to a surface as opposed to homogeneous catalysis in which both the catalyst and the substrate are in the same phase. This paper aims to demonstrate that monolayer protected metal clusters offer the advantage of being homogeneous catalysts over the heterogeneous catalysts of supported nanoparticles while retaining the unique catalytic ability of small metal clusters.

While Pd, Pt, and Au clusters continue to be studied for their catalytic activity, some researchers have also turned to studying bimetal clusters in catalysis.³⁴⁻³⁹ For example a

common catalyzed reaction studied is that of the hydrogenation of olefins. Research has been done using polymer-stabilized Pd, Pt, Rh, and Ir nanoparticles⁴⁰⁻⁴³ as well as Pd- including bimetallic nanoparticles, such as PdPt,^{44,45} AuPd,⁴⁶ and PdRh.⁴⁷ Another bimetal catalyst used is that of CuPd nanoparticles in the hydration of acrylonitrile.⁴⁸⁻⁵⁰ Finally the photo-induced hydrogen generation from H₂O catalyzed by Pt,⁵¹ AuPt,⁵¹ and PtRu⁵² nanoparticles has also been investigated. In all of these studies it was found that the bimetal clusters had higher catalytic efficiency than that of their monometal counterparts, although the rationale for this phenomenon has yet to be understood.

6.2 Experimental

Chemicals. H₂AuCl₄.xH₂O was synthesized according to literature.⁵³ Silver nitrate (AgNO₃, 99%), potassium tetrachloro-palladate (II) (K₂PdCl₄, 99%), N-(2-mercaptopropionyl)glycine (tiopronin, 99%), sodium borohydride (NaBH₄, 99%), and 4-nitrophenol (4-NP, 99%) were purchased from Aldrich. House-distilled water was purified on a Barnstead NANOpure system (= 18MΩ). All other chemical were reagent grade and used as received.

Synthesis of MPCs. Au and Ag Tiopronin MPCs were synthesized as reported previously.^{15,54} For Au Tiopronin MPCs,¹⁵ tetrachloroauric acid (0.50 g, 1.5 mmol) and N-(2-mercaptopropionyl)glycine (0.63 g, 3.9 mmol) were codissolved in 63mL 6:1 methanol/acetic acid, producing a ruby red solution. NaBH₄ (0.95 g, 25 mmol) in 12.5 mL of H₂O was added, immediately resulting in a black solution. Solution was stirred for 30min. The solvent was removed under vacuum (= 35 °C). The black product was dissolved in 25 mL H₂O and with drop wise addition of concentrated HCl adjusted to pH 1 and dialyzed (8 in. Spectra/Por CE, MWCO = 5000) for three days. The water was removed under vacuum resulting in the final product.

For Ag Tiopronin MPCs⁵⁴ AgNO₃ (1.0 g, 5.89 mmol) in 50 mL H₂O, N-(2-mercaptopropionyl)glycine (2.8 g, 17.6 mmol) in 20 mL of H₂O, and NaBH₄ (0.6 g, 15.9 mmol) in 15 mL of H₂O were all cooled to 0 °C. Solutions were mixed resulting in a black solution and stirred for 30 min. The Ag MPCs were precipitated with 300 mL of methanol then filtered and washed with methanol, ethanol and acetone. The black powder product was dissolved in H₂O and dialyzed (8 in. Spectra/Por CE, MWCO = 5000) for three days. Water was removed under vacuum resulting in the final product.

For Pd Tiopronin MPCs the same procedure used for Ag Tiopronin MPCs was adapted. K₂PdCl₄ (0.49 g, 1.5 mmol) in 12.5 mL of H₂O, N-(2-mercaptopropionyl)glycine (0.96 g, 5.9 mmol) in 7 mL of H₂O, and NaBH₄ (0.15 g, 3.9 mmol) in 3.8 mL of H₂O were all cooled to 0 °C. Solutions were mixed resulting in a black solution and stirred for 30 min.

The Pd MPCs were precipitated with 50 mL of methanol then filtered and washed with methanol, ethanol and acetone. The black powder product was dissolved in H₂O and dialyzed (8 in. Spectra/Por CE, MWCO = 5000) for three days. Water was removed under vacuum resulting in the final product.

For AgAu Tiopronin MPCs a similar procedure was followed, AgNO₃ (0.06 g, 0.35 mmol) in 10 mL of H₂O and tetrachloroauric acid (0.12 g, 0.35 mmol) in 10 mL of H₂O were cooled to 0 °C then mixed. Then 5 mL of N-(2-mercaptopropionyl)glycine (0.15 g, 0.92 mmol) in 10 mL of H₂O cooled to 0 °C was added to the salt solutions. The solutions were combined and NaBH₄ (0.13 g, 3.4 mmol) in 5 mL of H₂O cooled to 0 °C was added. The resulting solution was stirred for 30 min. The AgAu MPCs were precipitated with 50 mL of methanol then filtered and washed with methanol, ethanol and acetone. The black powder product was dissolved in H₂O and dialyzed (8 in. Spectra/Por CE, MWCO = 5000) for three days. Water was removed under vacuum resulting in the final product.

Spectroscopy. UV-vis spectra were collected with a Shimadzu UV-Vis (Model UV-1601) spectrometer. To keep samples oxygen-free, all solutions were kept under argon gas during data collection.

6.3 Results and Discussions

To study the catalytic properties of the tiopronin-protected Pd, Au, Ag, and AgAu clusters, 4-nitrophenol was utilized as the substrate to be reduced.¹ In the presence of NaBH₄ alone, 4-nitrophenol does not undergo reduction so the system is ideal for analyzing the catalytic activities of four tiopronin-protected water-soluble metal clusters. Three of the clusters were synthesized in a modified Brust-Schiffrin method starting with three different metal salts. The resulting MPCs had tiopronin monolayers and metal cores of Pd, Au, and Ag. The fourth MPC synthesized was a bimetal AgAu cluster which was synthesized again using the Brust-Schiffrin method but starting with equal parts Au and Ag salts. The UV/visible absorbance spectra of the four tiopronin-protected clusters are shown in Figure 6.1.

In an aqueous solution of NaBH₄ (with pH > 12), the λ_{max} of 4-nitrophenol is red shifted 377 nm to 400 nm owing to the formation of the 4-nitrophenolate ion.⁵⁵ When the metal cluster is introduced to the aqueous system, the peak at 400 nm disappears and a peak at 290 nm, corresponding to the reduced species, 4-aminophenol,⁵⁵ appears concurrently. Because of the very low concentration of the metal nanoparticles, their characteristic UV-Vis absorbance spectra do not interfere with that of the 4-nitrophenol. Figure 6.2 shows the UV-Vis absorbance spectra taken at 1 minute intervals for the reduction of 4-nitrophenol with NaBH₄ in the presence of the tiopronin-protected AgAu

¹ The idea to use the reduction of 4-nitrophenol to study the catalytic activity of the MPCs arose from a talk by Yuichi Negishi, Hironori Tsunoyama, and Tatsuya Tsukuda at the 2005 International Chemical Congress of Pasific Basin Societies (Pacifichem) in Honolulu, HI.

Figure 6.1. UV/visible absorbance spectra of tiopronin-protected clusters with metal cores of (a) Pd, (b) Au, (c) Ag, and (d) AgAu.

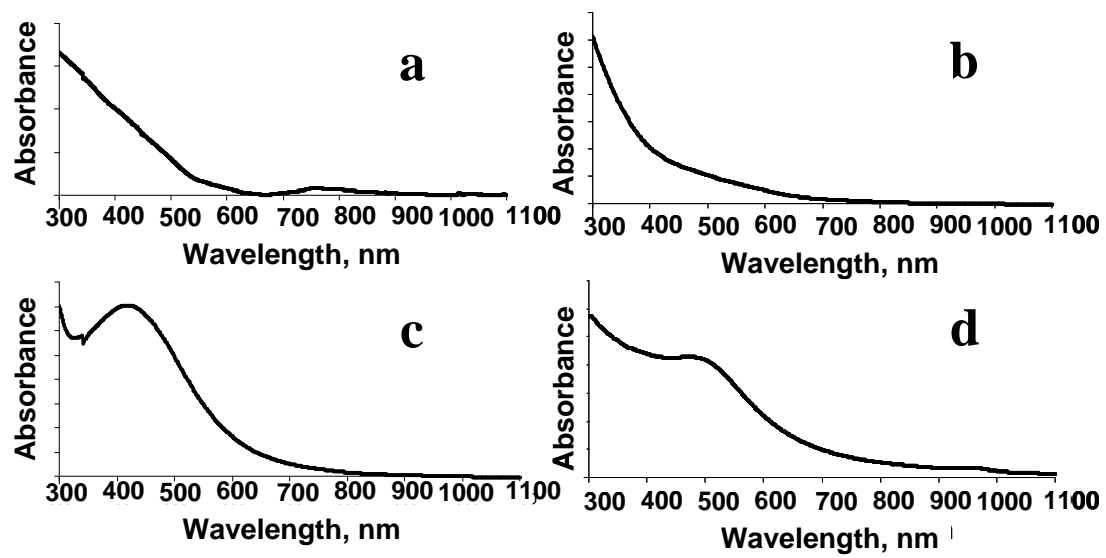
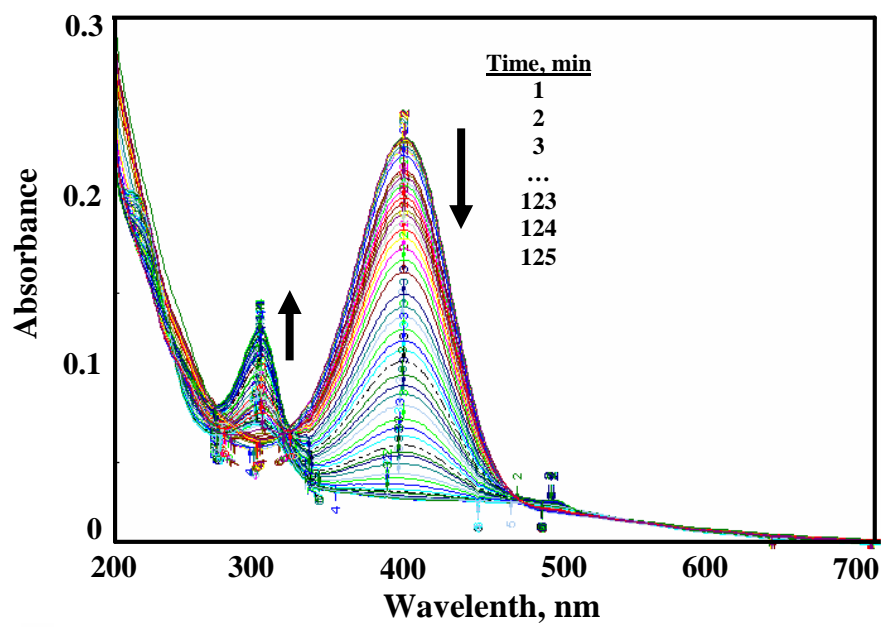


Figure 6.2. UV-Vis absorbance spectra of 0.1 mM 4-nitrophenol in H₂O (pH = 12) with 1×10^{-2} M NaBH₄ and 2.0×10^{-4} M tiopronin-protected AgAu clusters over a time period of one to 125 minutes with spectra taken every one minute.



bimetal cluster. The spectra for the other reactions of the other three clusters are not shown here but have identical features. Figure 6.3 displays a plot of absorbance vs. time for all four reactions. It is apparent that the different metal cores all demonstrate different catalytic rates with the tiopronin-protected Pd clusters catalyzing the reaction much faster than the other clusters.

In the cuvette where the catalyzed reduction of 4-nitrophenol took place, the NaBH_4 concentration was kept high so as to keep the BH_4^- in excess. This excess was needed for two reasons, the first being that the increased BH_4^- concentration caused the pH to increase, thus slowing down the degradation of BH_4^- , and, as the liberated hydrogen purged out air, minimized aerial oxidation of the reduced product.⁵⁶ The other motivation for having an excess of BH_4^- is that its concentration remains constant so that pseudo first-order kinetics with respect to 4-nitrophenol could be used in this case to study the catalytic rate of the tiopronin-protected metal clusters.⁵⁶ To determine the apparent rate-constants for the catalytic reduction of 4-nitrophenol with the four different metal clusters, $\ln(\text{Abs})$ vs. time, where *Abs* is the absorbance at 400 nm at any time, was plotted (Figure 6.4), and a good linear correlation was observed for all four reactions indicating that the catalyzed reactions were first order in substrate.

The apparent rate constants of the catalyzed reduction of 4-nitrophenol with the four different metal clusters are listed in Table 6.1 and compared to the published values of the slightly larger generations 3.0 and 5.0 poly(amidoamine) (PAMAM) and 3.0 and 4.0 poly(propyleneimine) (PPI) dendrimer-protected Au clusters catalyzing the same reduction reaction.⁵⁶ The catalytic rate constants from the tiopronin-protected MPCs are comparable to the dendrimer-protected Au clusters, with the tiopronin-protected Pd cluster clearly resulting as the superior catalyst. This result is not surprising considering

Figure 6.3. Absorbance at 400 nm vs. time plot of the reduction of 4-nitrophenol using the tiopronin-protected clusters with metal cores comprised of (a) Pd, (b) AgAu, (c) Ag, and (d) Au. Absorbance was monitored in H₂O (pH = 12) with 1.0×10^{-2} M NaBH₄, and 2.0×10^{-4} M MPC.

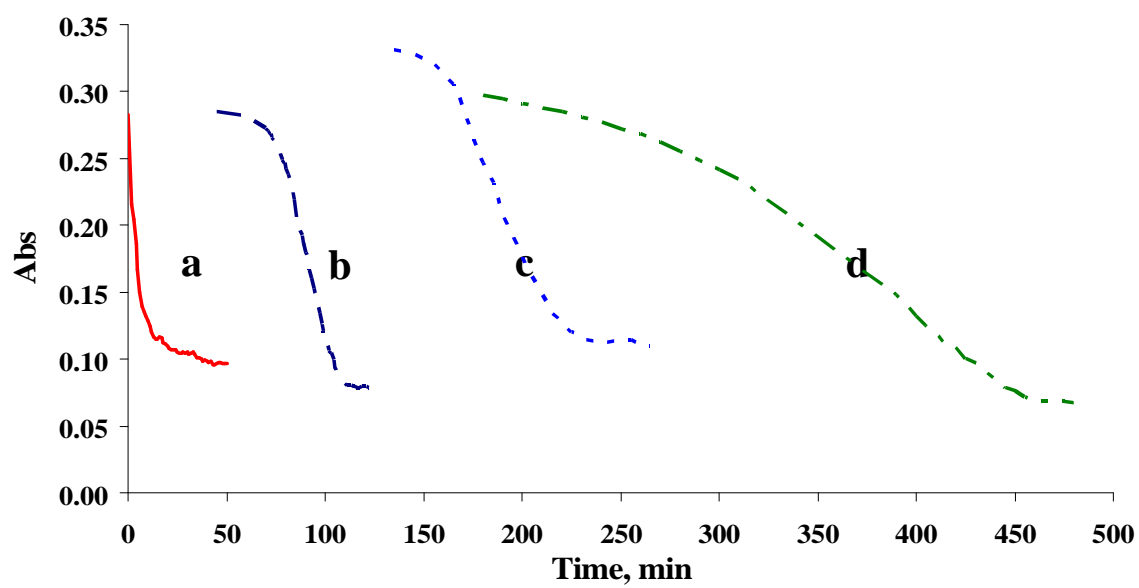
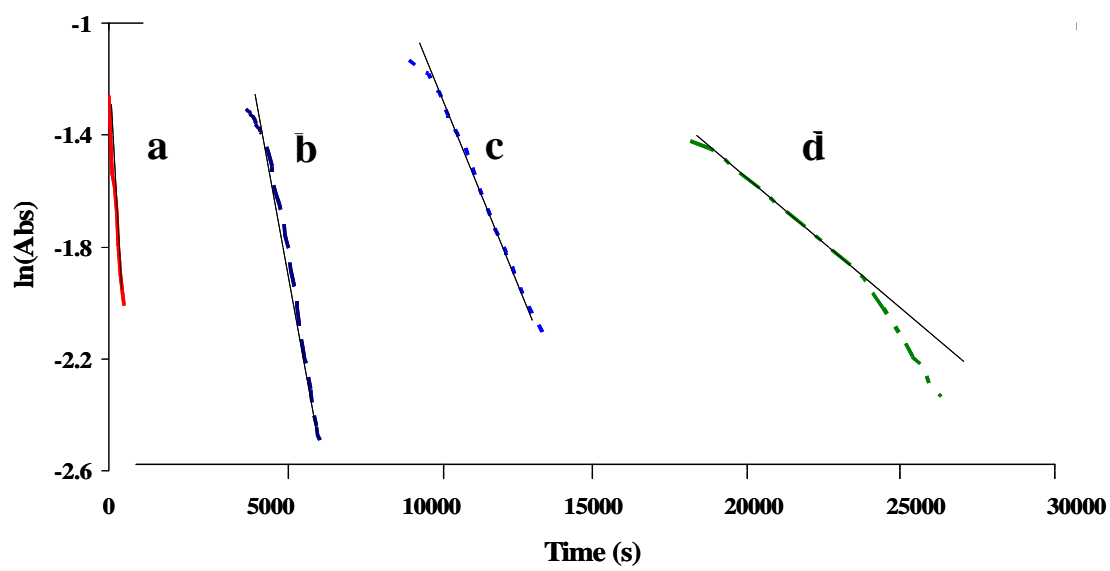


Figure 6.4. Plot of $\ln(Abs)$ vs. time, where Abs is absorbance monitored at 400 nm, of the reduction of 4-nitrophenol using as catalysts the tiopronin-protected clusters with metal cores comprised of (a) Pd, (b) AgAu, (c) Ag, and (d) Au. Absorbance was monitored in H_2O (pH = 12) with 1.0×10^{-2} M $NaBH_4$, and 2.0×10^{-4} M MPC. The straight black lines through the curves were used to determine the apparent rate constant.



the abundant use of Pd as a catalyst for organic reductions. The more intriguing result is that the rate constant for the bimetallic AgAu cluster is faster than both the single metal Ag and Au core nanoparticles. While it is beyond the scope of this study to determine why the bimetal cluster has a higher catalytic activity than the monometallic clusters, it should be noted that this has been observed for other systems.^{44,46,50}

6.4 Conclusions

It can be concluded that all four tiopronin-protected water soluble metal clusters acted as efficient catalysts in the reduction of 4-nitrophenol in the presence of NaBH₄ in an aqueous solution (pH > 12) under Ar atmosphere. The cluster with the highest catalytic activity proved to be the Pd cluster which was not surprising knowing that Pd is a common metal used in catalysis owing to its ability to activate hydrogen. A more exciting result is that the AgAu bimetal cluster demonstrated a much higher catalytic activity and faster overall rate constant than either the Ag or the Au monometal cluster.

While it is beyond the capacity of this paper to explain this result, we find it intriguing and believe it will be useful in the sizeable catalysis industry.

6.5 Acknowledgements

This research was supported by grants from the National Science Foundation and Office of Naval Research. Contribution from Alicia Douglas from the University of North Carolina is also acknowledged, in particular Dr. Douglas's syntheses of the four nanoparticles investigated were especially helpful.

Table 6.1. Apparent rate constants for the reduction of 4-nitrophenol in the presence of NaBH₄ and tiopronin-protected metal clusters.

Experimental Values		Literature Values ⁵⁶	
Tiopronin-Protected Metal Core	Apparent Rate Constant (10 ⁻³ , s ⁻¹)	Dendrimer Protecting Au Core ^a	Apparent Rate Constant (10 ⁻³ , s ⁻¹)
Pd	16.0	PPI G4	10.6
AgAu	6.0	PPI G3	9.49
Ag	3.0	PAMAM G3	3.70
Au	1.0	PAMAM G5	2.40

^a PPI symbolizes poly(propyleneimine) dendrimers, PAMAM represents poly(amidoamine) dendrimers, and G followed by a number indicates the number of generations in the dendrimer

6.6 References

- (1) Hostetler, M. J.; Wingate, J. E.; Zhong, C.-J.; Harris, J. E.; Vachet, R. W.; Clark, M. R.; Londono, J. D.; Green, S. J.; Stokes, J. J.; Wignall, G. D.; Glish, G. L.; Porter, M. D.; Evans, N. D.; Murray, R. W. *Langmuir* **1998**, *14*, 17-30.
- (2) Brust, M.; Walker, M.; Bethell, D.; Schiffrin, D. J.; Whyman, R. *J. Chem. Soc.-Chem. Commun.* **1994**, 801-802.
- (3) Balasubramanian, R.; Guo, R.; Mills, A. J.; Murray, R. W. *J. Am. Chem. Soc.* **2005**, *127*, 8126-8132.
- (4) Wolfe, R. L.; Murray, R. W. *Anal. Chem.* **2006**, *78*, 1167-1173.
- (5) Templeton, A. C.; Wuelfing, M. P.; Murray, R. W. *Accounts Chem. Res.* **2000**, *33*, 27-36.
- (6) Chen, S. W.; Ingram, R. S.; Hostetler, M. J.; Pietron, J. J.; Murray, R. W.; Schaaff, T. G.; Khoury, J. T.; Alvarez, M. M.; Whetten, R. L. *Science* **1998**, *280*, 2098-2101.
- (7) Hayat, M. A. *Colloidal Gold: Principles, Methods, and Applications*; Academic Press: San Diego, 1991.
- (8) Templeton, A. C.; Hostetler, M. J.; Warmoth, E. K.; Chen, S. W.; Hartshorn, C. M.; Krishnamurthy, V. M.; Forbes, M. D. E.; Murray, R. W. *J. Am. Chem. Soc.* **1998**, *120*, 4845-4849.
- (9) Templeton, A. C.; Hostetler, M. J.; Kraft, C. T.; Murray, R. W. *J. Am. Chem. Soc.* **1998**, *120*, 1906-1911.
- (10) Ingram, R. S.; Hostetler, M. J.; Murray, R. W. *J. Am. Chem. Soc.* **1997**, *119*, 9175-9178.
- (11) Ingram, R. S.; Murray, R. W. *Langmuir* **1998**, *14*, 4115-4121.
- (12) Green, S. J.; Stokes, J. J.; Hostetler, M. J.; Pietron, J.; Murray, R. W. *J. Phys. Chem. B* **1997**, *101*, 2663-2668.
- (13) Green, S. J.; Pietron, J. J.; Stokes, J. J.; Hostetler, M. J.; Vu, H.; Wuelfing, W. P.; Murray, R. W. *Langmuir* **1998**, *14*, 5612-5619.
- (14) Hostetler, M. J.; Green, S. J.; Stokes, J. J.; Murray, R. W. *J. Am. Chem. Soc.* **1996**, *118*, 4212-4213.
- (15) Templeton, A. C.; Chen, S. W.; Gross, S. M.; Murray, R. W. *Langmuir* **1999**, *15*, 66-76.

- (16) Clifffel, D. E.; Zamborini, F. P.; Gross, S. M.; Murray, R. W. *Langmuir* **2000**, *16*, 9699-9702.
- (17) Choi, M. M. F.; Douglas, A. D.; Murray, R. W. *Anal. Chem.* **2006**, *78*, 2779-2785.
- (18) Negishi, Y.; Nobusada, K.; Tsukuda, T. *J. Am. Chem. Soc.* **2005**, *127*, 5261-5270.
- (19) Sakurai, H.; Tsunoyama, H.; Tsukuda, T. *J. Organomet. Chem.* **2007**, *692*, 368-374.
- (20) Tsunoyama, H.; Sakurai, H.; Tsukuda, T. *Chem. Phys. Lett.* **2006**, *429*, 528-532.
- (21) Yanagimoto, Y.; Negishi, Y.; Fujihara, H.; Tsukuda, T. *J. Phys. Chem. B* **2006**, *110*, 11611-11614.
- (22) Tsunoyama, H.; Sakurai, H.; Negishi, Y.; Tsukuda, T. *J. Am. Chem. Soc.* **2005**, *127*, 9374-9375.
- (23) Tsunoyama, H.; Sakurai, H.; Ichikuni, N.; Negishi, Y.; Tsukuda, T. *Langmuir* **2004**, *20*, 11293-11296.
- (24) Eklund, S. E.; Clifffel, D. E. *Langmuir* **2004**, *20*, 6012-6018.
- (25) Briggs, C.; Norsten, T. B.; Rotello, V. M. *Chem. Commun.* **2002**, 1890-1891.
- (26) Galow, T. H.; Drechsler, U.; Hanson, J. A.; Rotello, V. M. *Chem. Commun.* **2002**, 1076-1077.
- (27) Pietron, J. J.; Hicks, J. F.; Murray, R. W. *J. Am. Chem. Soc.* **1999**, *121*, 5565-5570.
- (28) Pietron, J. J.; Murray, R. W. *J. Phys. Chem. B* **1999**, *103*, 4440-4446.
- (29) Ponc, V.; Bond, G. C. *Catalysis by Metals and Alloys*; Elsevier: Amsterdam, 1996.
- (30) Haruta, M.; Yamada, N.; Kobayashi, T.; Iijima, S. *J. Catal.* **1989**, *115*, 301-309.
- (31) Davis, R. J. *Science* **2003**, *301*, 926-927.
- (32) Bond, G. C.; Thompson, D. T. *Catal. Rev.-Sci. Eng.* **1999**, *41*, 319-388.
- (33) Lopez, N.; Norskov, J. K. *J. Am. Chem. Soc.* **2002**, *124*, 11262-11263.
- (34) Meitzner, G.; Via, G. H.; Lytle, F. W.; Sinfelt, J. H. *J. Chem. Phys.* **1987**, *87*, 6354-6363.
- (35) Sinfelt, J. H. *Accounts Chem. Res.* **1987**, *20*, 134-139.

- (36) Meitzner, G.; Via, G. H.; Lytle, F. W.; Sinfelt, J. H. *J. Chem. Phys.* **1985**, 83, 4793-4799.
- (37) Wang, P. K.; Slichter, C. P.; Sinfelt, J. H. *J. Phys. Chem.* **1985**, 89, 3606-3609.
- (38) Meitzner, G.; Via, G. H.; Lytle, F. W.; Sinfelt, J. H. *J. Chem. Phys.* **1983**, 78, 2533-2541.
- (39) Meitzner, G.; Via, G. H.; Lytle, F. W.; Sinfelt, J. H. *J. Chem. Phys.* **1983**, 78, 882-889.
- (40) Hirai, H.; Nakao, Y.; Toshima, N. *Chem. Lett.* **1976**, 905-910.
- (41) Hirai, H.; Nakao, Y.; Toshima, N. *Chem. Lett.* **1978**, 545-548.
- (42) Hirai, H.; Nakao, Y.; Toshima, N. *Journal of Macromolecular Science-Chemistry* **1978**, A12, 1117-1141.
- (43) Hirai, H.; Nakao, Y.; Toshima, N. *Journal of Macromolecular Science-Chemistry* **1979**, A13, 727-750.
- (44) Toshima, N.; Yonezawa, T.; Kushihashi, K. *Journal of the Chemical Society-Faraday Transactions* **1993**, 89, 2537-2543.
- (45) Toshima, N.; Kushihashi, K.; Yonezawa, T.; Hirai, H. *Chem. Lett.* **1989**, 1769-1772.
- (46) Toshima, N.; Harada, M.; Yamazaki, Y.; Asakura, K. *J. Phys. Chem.* **1992**, 96, 9927-9933.
- (47) Zhao, B.; Toshima, N. *Chem. Express.* **1990**, 5, 721.
- (48) Toshima, N.; Wang, Y. *Adv. Mater.* **1994**, 6, 245-247.
- (49) Toshima, N.; Wang, Y. *Chem. Lett.* **1993**, 1611-1614.
- (50) Toshima, N.; Wang, Y. *Langmuir* **1994**, 10, 4574-4580.
- (51) Yonezawa, T.; Toshima, N. *Journal of Molecular Catalysis* **1993**, 83, 167-181.
- (52) Miner, R. S.; Namba, S.; Turkevich, J. *Proceedings of the 7th International Congress on Catalysis* Kodansha, Tokyo, 1981.
- (53) Brauer, G. *Handbook of Preparative Inorganic Chemistry*; Academic Press: New York, 1965.
- (54) Huang, T.; Murray, R. W. *J. Phys. Chem. B* **2003**, 107, 7434-7440.

- (55) Pradhan, N.; Pal, A.; Pal, T. *Langmuir* **2001**, *17*, 1800-1802.
- (56) Hayakawa, K.; Yoshimura, T.; Esumi, K. *Langmuir* **2003**, *19*, 5517-5521.